

DOCTORAL THESIS

DEVELOPMENT OF
LARGE-SCALE NANOPOWDER SYNTHESIS METHOD USING
MODULATED INDUCTIVELY COUPLED THERMAL PLASMA AND
VISUALIZATION OF REACTION FIELD IN THE TORCH



KANAZAWA UNIVERSITY
GRADUATE SCHOOL OF NATURAL SCIENCE AND TECHNOLOGY
ELECTRICAL ENGINEERING AND COMPUTER SCIENCE

STUDENT ID 1524042001

NAOTO KODAMA

SUPERVISERS

PROF. YASUNORI TANAKA

PROF. YOSHIHIKO UESUGI

PROF. TATSUO ISHIJIMA

MARCH, 2018

Contents

Acknowledgement	xv
Chapter1 Introduction	1
1.1 Plasma state	1
1.1.1 Overview of plasma	1
1.1.2 Concept of temperature	2
1.1.3 Classification of plasma by temperature	4
1.2 Inductively coupled thermal plasma system	7
1.3 Nanoparticles	8
1.3.1 Overview of nanoparticle	8
1.3.2 Nanoparticle synthesis method	9
1.3.3 Experimental measurement method of nanoparticle synthesis field	11
1.4 Objective of this thesis	16
1.5 Composition of the thesis	18
References in chapter 1	19
Chapter2 Large-scale synthesis of Al ³⁺ -doped TiO ₂ nanopowder using pulse-modulated induction thermal plasmas	23
2.1 Introduction	23
2.2 Methodology of a large-scale nanopowder synthesis system	25
2.3 Experimental setups	28
2.3.1 Experimental arrangements	28
2.3.2 Experimental condition	29
2.4 Results and discussions	32
2.4.1 SEM images and particle size distribution of synthesized powder	32

2.4.2	Element distribution analysis of synthesized nanoparticles using BF-TEM & TEM/EDX mapping	35
2.4.3	Crystal composition assessment of synthesized Al ³⁺ -doped TiO ₂ nanopowder using XRD spectra analysis	36
2.4.4	Chemical binding state in synthesized Al ³⁺ -doped TiO ₂ nanopowder by XPS spectra analysis	38
2.4.5	Optical property of synthesized Al ³⁺ -doped TiO ₂ nanopowder by spectrophotometric analysis	40
2.5	Summary of chapter 2	41
	References in chapter 2	43
Chapter3	Fundamental behavior of Ti and TiO vapor in the induction thermal plasma	47
3.1	Introduction	47
3.2	Principle of two-dimensional optical emission spectroscopy system	49
3.3	Experimentals	51
3.3.1	Spectroscopic observation conditions	53
3.4	Two-dimensional spectroscopic observation results	55
3.4.1	Test spectroscopic observation for simultaneous observation	55
3.5	Results and discussions	56
3.5.1	Spatial and temporal variation of Ti I radiation intensities	56
3.5.2	Spatial and temporal variation of TiO molecular spectra	59
3.6	Discussion	61
3.6.1	Equilibrium particle composition for Ar-O-Ti system	61
3.6.2	Effect on plasma properties by Ti vapour inclusion into Ar-O ₂ plasmas	63
3.6.3	Effect of carrier gas injection to the temperature field	66
3.6.4	Ti feedstock evaporation and precursor formation in the ICTP torch	67
3.7	Summary	71
	References in chapter 3	73
Chapter4	Influence of coil-current modulation on Ti feedstock evaporation and formation of TiO precursor molecule	79
4.1	Introduction	79

4.2	PMITP+TCFF approach for large-scale nanopowder synthesis	81
4.3	Experimentals	83
4.3.1	Experimental conditions	83
4.3.2	2D OES conditions	84
4.4	Results and discussions	86
4.4.1	Synthesized nanoparticles	86
4.4.2	Two-dimensional distribution of radiation intensities	87
4.4.3	Temporal variation in radiation intensities for different spectral lines	90
4.4.4	Discussion on Ti evaporation and TiO formation in PMITP+TCFF method	92
4.5	Summary	93
	References in chapter 4	95
Chapter5	Spatial estimation of Ti excitation temperature in the ICTP torch dur- ing TiO ₂ nanopowder synthesis	97
5.1	Introduction	97
5.2	Experimentals	99
5.2.1	Experimental setup	99
5.2.2	Experimental conditions	100
5.2.3	Optical emission spectroscopy conditions	103
5.3	Determination method of Ti excitation temperature	104
5.4	Two-dimensional spectroscopic observation results	106
5.4.1	Spatial distribution of Ti I radiation intensities	106
5.4.2	Spatiotemporal distribution of the Ti excitation temperature	108
5.5	Discussion	112
5.5.1	Equilibrium particle composition for the Ar-O-Ti system	112
5.5.2	Temperature difference between with and without Abel inversion .	115
5.5.3	Possibility in nucleation occurrence in the torch	116
5.6	Summary	118
	References in chapter 5	119

Chapter6	Determination of Ti vapor admixture ratio in the Ar ICTP torch during Ti feedstock injection	123
6.1	Introduction	123
6.2	Experimentals	125
6.2.1	Experimental configuration	125
6.2.2	Experimentals conditions	126
6.2.3	Optical emission spectroscopy setup	126
6.3	Determination procedure	129
6.3.1	Determination of Ti excitation temperature	129
6.3.2	Definition of the Ti vapor admixture ratio	130
6.3.3	Equilibrium particle compositions	131
6.3.4	Procedure for determination of the Ti vapor admixture ratio and particle number densities	132
6.4	Results and discussion	137
6.4.1	Spatial distribution of Ti I and Ar I radiation intensities	137
6.4.2	Spatial distribution of Ti excitation temperature	137
6.4.3	Estimation result of Ti vapor admixture ratio	138
6.4.4	Estimation result of particle number density	141
6.5	Summary	142
	References in chapter 6	143
Chapter7	Conclusions	147
7.1	Introduction	147
7.2	Summary of results	148
7.2.1	Large-scale synthesis of Al ³⁺ -doped TiO ₂ nanopowder	148
7.2.2	Fundamental investigation of Ti feedstock evaporation in the ICTP torch during TiO ₂ nanopowder synthesis	148
7.2.3	Effect of coil-current modulation on feedstock evaporation and precursor TiO formation during TiO ₂ nanopowder synthesis	149
7.2.4	Spatial estimation of Ti excitation temperature in the ICTP torch during TiO ₂ nanopowder synthesis	149

7.2.5	Determination of Ti vapor admixture ratio in the Ar ICTP torch during Ti feedstock injection	150
7.3	Scope of future researches	150

List of Figures

1.1	States of materials.	2
1.2	Maxwell-Boltzmann velocity distribution of Argon atom as function of velocity and temperature.	3
1.3	Classification of plasmas by electron temperature and electron density. . .	5
1.4	Inductively coupled thermal plasma system [4].	6
1.5	Schematic of ICTP torch.	6
1.6	Color and absorption spectra of gold solution. (a) Color of different-size gold nanoparticle solutions [6]. (b) Absorption of colloidal gold found experimentally [7]. Numbers on curves indicate particle diameters in $\text{\AA}(10^{-10})$ units. For small (~ 30 nm) mono-disperse gold nanoparticles, blue-green light (wavelength $\lambda \sim 450$ nm) is absorbed while red light ($\lambda \sim 700$ nm) is reflected. Thus, solution color is rich red color. As increasing particle sizes, absorbance of red light is increased while blue light is reflected. Consequently solution color becomes pale blue or purple color.	9
1.7	Overview of nanoparticle synthesis method.	10
1.8	Nanoparticle synthesis process using ICTP method.	12
1.9	Energy diagram of hydrogen atom and wavelength of emission spectra. . .	15
1.10	The OES result for Ar-O ₂ ICTP.	15
2.1	Modulated coil current and definition of modulation parameters.	26
2.2	Method for large-scale nanopowder synthesis using pulse-modulated induction thermal plasma with time-controlled feedstock feeding (PMITP+TCFF). 27	
2.3	Whole system of nanopowder synthesis using PMITP+TCFF.	28

2.4	FE-SEM images for (a) feedstock, and synthesized powder with conditions (b) 80%SCL, $g_{\text{pow}} = 12 \text{ g min}^{-1}$, (c) 70%SCL, $g_{\text{pow}} = 12 \text{ g min}^{-1}$, and (d) 60%SCL, $g_{\text{pow}} = 19 \text{ g min}^{-1}$	32
2.5	Particle size distributions for (a) 80%SCL, $g_{\text{pow}} = 12 \text{ g min}^{-1}$, (b) 70%SCL, $g_{\text{pow}} = 12 \text{ g min}^{-1}$, and (c) 60%SCL, $g_{\text{pow}} = 19 \text{ g min}^{-1}$	33
2.6	Dependence of particle mean diameter and standard deviation on the shimmer current level of the pulse modulation.	34
2.7	BF-TEM and TEM/EDX mapping for (a) 80%SCL, $g_{\text{pow}} = 12 \text{ g min}^{-1}$, (b) 70%SCL, $g_{\text{pow}} = 12 \text{ g min}^{-1}$, and (c) 60%SCL, $g_{\text{pow}} = 19 \text{ g min}^{-1}$	35
2.8	XRD spectra for (a) 80%SCL, $g_{\text{pow}} = 12 \text{ g min}^{-1}$, (b) 70%SCL, $g_{\text{pow}} = 12 \text{ g min}^{-1}$, (c) 60%SCL, $g_{\text{pow}} = 19 \text{ g min}^{-1}$, and (d) reference peaks.	37
2.9	XPS spectra for commercial pure-TiO ₂ (P-25; Degussa), pure-TiO ₂ nanopowder synthesized using PMITP+TCFF and Al ³⁺ -doped TiO ₂ nanopowder synthesized in this study. (a) Ti 2p region between 455 eV and 470 eV, (b) Al 2p region between 70 eV and 80 eV.	39
2.10	Diffuse reflection spectra for commercial pure-TiO ₂ (P-25; Degussa) and Al ³⁺ -doped TiO ₂ nanopowder synthesized in this study.	40
3.1	The principle of 2D OES system.	50
3.2	Experimental configuration using ICTP and solenoid valve installed to control feedstock injection.	52
3.3	Two-dimensional spectroscopic observation region and observation system using imaging spectrometer and high-speed video camera.	55
3.4	Test observation result. (a) Ti I radiation intensities observed simultaneously. (b) TiO radiation intensities observed simultaneously.	57
3.5	Two-dimensional spectroscopic observation result during TiO ₂ nanopowder synthesis using non-modulated ICTP torch with intermittent feedstock feeding. Two-dimensional distribution of Ti I radiation intensities for (a) 27%DF _{valve} (open/close=8/22 ms), (b) 40%DF _{valve} (open/close=12/18 ms), and (c) 53%DF _{valve} (open/close=16/14 ms)	58

3.6	Two-dimensional spectroscopic observation result during TiO ₂ nanopowder synthesis using non-modulated ICTP torch with intermittent feedstock feeding. Two-dimensional distribution of TiO radiation intensities for (a) 27%DF _{valve} (open/close=8/22 ms), (b) 40%DF _{valve} (open/close=12/18 ms), and (c) 53%DF _{valve} (open/close=16/14 ms)	60
3.7	Equilibrium particle composition for the Ar-O-Ti system.	62
3.8	Thermal conductivity of various gas composition conditions.	65
3.9	Electrical conductivity of various gas composition conditions.	66
3.10	Temperature distribution in the torch and reaction chamber. (a) No carrier gas injection, and (b) 4 L min ⁻¹ Ar carrier gas injection.	68
3.11	Understanding of Ti feedstock evaporation and precursor TiO molecules in the torch. (a) Observation result for Ti I in valve open condition of 8 ms, (b) Observation result for TiO in valve open condition of 8 ms, (c) Estimated timing of feedstock injection into the torch, (d) Estimated temporal variation of temperature, and (e) Estimated timing of formation of precursor TiO molecules,	69
3.12	Temporal and spatial variation of Ti atomic density and TiO molecular density in the ICTP torch estimated from two-dimensional spectroscopic observation result for 27%DF _{valve} . (a) Before feedstock injection into the ICTP torch(<i>t</i> =0 ms), (b) Ti feedstock feeding, Ti evaporation and TiO formation (<i>t</i> ~7 ms), (c) Formation of high-density Ti-O mixture and TiO molecules (<i>t</i> ~14 ms), (d) TiO transport and TiO dissociation attributable to the increased temperature by stopping of feedstock feeding (<i>t</i> ~18 ms), (e) Formation of high-density Ti atoms attributable to dissociation reaction of TiO→Ti+O (<i>t</i> ~20 ms), and (e) Convective transport of Ti atoms (<i>t</i> ~22 ms).	72
4.1	Method for large-scale nanopowder synthesis using induction thermal plasma. Left-hand side: conventional non-modulated ICTP with continuous feedstock feeding; Right-hand side: PMITP with intermittent feedstock feeding.	82
4.2	The 2D OES system and observation area for an induction thermal plasma torch.	85

4.3	FE-SEM images of nanoparticles synthesized (a) by non-modulated ICTP, and (b) by PMITP with intermittent feedstock feeding (80%SCL) [15].	86
4.4	Particle size distribution of nanoparticles synthesized (a) by non-modulated ICTP and (b) by PMITP with intermittent feedstock feeding (80%SCL) [15].	86
4.5	Two-dimensional distribution of radiation intensities for the non-modulated ICTP (100%SCL) with continuous feedstock feeding. (a) Ar I: 811.53 nm, (b) O I: 777.54 nm, (c) Ti I: 453.32 nm, and (d) TiO: 615.91 nm.	88
4.6	Two-dimensional distribution of radiation intensities from the PMITP for 80%SCL with continuous feedstock feeding. (a) Ar I: 811.53 nm, (b) O I: 777.54 nm, (c) Ti I: 453.32 nm, and (d) TiO: 615.91 nm.	89
4.7	Two-dimensional distribution of radiation intensities from the PMITP for 80%SCL with intermittent feedstock feeding. (a) Ar I: 811.53 nm, (b) O I: 777.54 nm, (c) Ti I: 453.32 nm, and (d) TiO: 615.91 nm.	90
4.8	Temporal variation of radiation intensities of different spectral lines observed below the coil end. (a) Non-modulated coil current with continuous feedstock feeding, (b) modulated coil current of 80%SCL with continuous feedstock feeding, (c) modulated coil current of 80%SCL with intermittent feedstock feeding.	91
4.9	An interpretation on the evaporation process of Ti feedstock and the formation of TiO for pulse-modulation with intermittent feedstock feeding. (a) Input powder increase and initiation of feedstock feeding in on-time; (b) The evaporation of Ti feedstock, and then diffusion of Ti atoms in on-time ($t= 0$ ms); (c) Mixing of Ti and O atoms, and initiation of TiO formation around the axis ($t= 3$ ms); (d) Increasing of TiO density ($t= 6$ ms); (e) Formation of high TiO density region ($t= 9$ ms); (f) Transportation of TiO to the downstream of the PMITP torch ($t= 12$ ms).	94
5.1	Experimental apparatus using an ICTP torch and solenoid valve.	101
5.2	Overall view of the experimental apparatus used for nanopowder fabrication.	101
5.3	Two-dimensional spectroscopic observation region and observation system using an imaging spectrometer and high-speed video camera.	104
5.4	Relation between I_{453}/I_{521} and the Ti excitation temperature.	106

5.5	2D OES results for two Ti atomic lines. (a) High-speed solenoid valve open–close signal. (b) Estimated actual feedstock injection timing into the ICTP torch. (c) Ti I radiation intensity at 453.32 nm wavelength. (d) Ti I radiation intensity at 521.04 nm wavelength.	108
5.6	Comparison between Ti I radiation intensities and estimated Ti excitation temperature distribution at $t=16$ ms. (a) Ti I radiation intensity at 453.32 nm wavelength. (b) Ti I radiation intensity at 521.04 nm wavelength. (c) 2D distribution of Ti excitation temperature.	109
5.7	Comparison between Ti I and TiO radiation intensities and estimated Ti excitation temperature distribution at $t=16$ ms. (a) Ti I radiation intensity at 453.32 nm wavelength. (b) 2D distribution of Ti excitation temperature. (c) TiO radiation intensity obtained from our earlier work [31].	110
5.8	Comparison between 2D OES results and estimated Ti excitation temperature distribution. (a) Ti I radiation intensity at 453.32 nm wavelength. (b) 2D distribution of Ti excitation temperature. (c) TiO radiation intensity obtained from our earlier work [31].	111
5.9	Equilibrium particle compositions for the Ar-O ₂ -Ti system: (a) 89%Ar-10%O ₂ -1%Ti, and (b) 50%Ar-25%O ₂ -25%Ti.	113
5.10	Estimation result of Ti excitation temperature with Abel inversion at $z=20$ mm. 114	
5.11	Estimation result of TiO ₂ (g) saturation vapour pressure in the ICTP torch.	117
6.1	Experimental apparatus using an ICTP torch.	125
6.2	OES spectra for the region below the coil-end (a) $\lambda=430$ nm to 830 nm, and (b) Ti I spectra ($\lambda=430$ nm to 530 nm).	127
6.3	2D OES region in this work.	127
6.4	Flowchart to determine Ti excitation temperature and Ti vapor admixture ratio.	131
6.5	Equilibrium particle compositions for Ar-Ti system at pressure of 300 Torr: (a) 1 mol%Ti and (b) 10^{-5} mol%Ti.	133
6.6	Emission coefficient ratio between Ti I@521.04 nm and Ar I@811.53 nm as a function of temperature and Ti vapor admixture ratio.	134

6.7	Particle number densities as a function of the temperature and Ti vapor admixture ratio: (a) number density of Ar atom, (b) number density of Ti atom, and (c) electron density.	135
6.8	2D OES results for Ti I and Ar I atomic spectra: (a) Ti I ($\lambda=453.32$ nm), (b) Ti I ($\lambda=521.04$ nm), and (c) Ar I ($\lambda=811.53$ nm).	136
6.9	Determination result for spatial distribution of Ti excitation temperature: (a) Ti I ($\lambda=453.32$ nm) and (b) Ti excitation temperature $T_{\text{ex}}^{\text{Ti}}$	138
6.10	Estimation result for spatial distribution of Ti vapor admixture ratio: (a) Ti I ($\lambda=453.32$ nm) and (b) Ti vapor admixture ratio X_{Ti}	139
6.11	Spatial distribution of particle number densities: (a) Ar atomic number density n_{Ar} , (b) Ti atomic number density n_{Ti} , and (c) electron density n_e	140

List of Tables

2.1	Experimental conditions.	30
3.1	Experimental conditions.	54
3.2	Two-dimensional spectroscopic observation conditions.	56
4.1	Experimental conditions.	84
4.2	The 2D OES measurement conditions.	85
5.1	Experimental conditions.	102
5.2	Two-dimensional spectroscopic observation conditions.	103
5.3	Physical quantities for respective Ti I spectra.	106
6.1	Experimental conditions.	128
6.2	Two-dimensional spectroscopic observation conditions.	129

Acknowledgement

First of all, I would like to express my gratitude to Prof. Yasunori Tanaka, Prof. Yoshihiko Uesugi, and Prof. Tatsuo Ishijima for devoted supervision. Without their help and devoted supervision, it was hard for me to achieve my research described in this thesis. I also express my deep gratitude to Prof. Takafumi Seto and Associate Prof. Norio Tokuda for their many advices. I would like to thank Ms. W. Guo, Mr. K. Kita, Mr. Y. Ishisaka, Mr. K. Shimizu and Mr. K. Onda for many useful discussion, working together, and many helps. Thanks to them, I really enjoyed my researching life at the Kanazawa university. Finally, I would like to thank my parents and my brothers, for all their care, help and understanding for my working in the Kanazawa university.

Abstract

The method for large-scale synthesis of Al^{3+} -doped TiO_2 nanopowder was developed using pulse-modulated induction thermal plasma with time-controlled feedstock feeding method (PMITP+TCFF method). In this method, the feedstock was synchronously and intermittently injected into the PMITP torch with coil-current modulation. As a result, Al^{3+} -doped TiO_2 nanopowder was successfully synthesized with a production rate of about 400 g/h at an input power of 20 kW. In addition, the mean particle diameter was also successfully controlled by coil-current modulation.

Furthermore, two-dimensional optical emission spectroscopy (2D OES) was carried out to investigate spatiotemporal distribution of Ti and TiO vapor during TiO_2 nanopowder synthesis using the conventional ICTP or PMITP+TCFF method. In addition, the spatiotemporal distribution of Ti excitation temperature ($T_{\text{ex}}^{\text{Ti}}$) was also estimated from the 2D OES results. Investigation results suggest that injected Ti feedstock was evaporated to form high concentration of Ti vapor at on- and off-axis region, while TiO vapor was almost simultaneously generated in low-temperature on-axis region. In addition, it was also confirmed that the PMITP+TCFF method is effective for efficient feedstock evaporation and precursor TiO formation.

Furthermore, Ti vapor admixture ratio (X_{Ti}) was also estimated with $T_{\text{ex}}^{\text{Ti}}$ during Ti nanopowder synthesis to investigate Ti vapor admixing effect on plasma temperature. The X_{Ti} was estimated from the 2D OES results and the calculated emission coefficients. These estimation results revealed much higher X_{Ti} and higher temperature at off-axis region compared with those at on-axis region.

Chapter 1

Introduction

1.1 Plasma state

1.1.1 Overview of plasma

The different states of matter existing on the earth are solid, liquid, and gas. As shown in Fig. 1.1, these matter changes in phase depend on its temperature or internal energy. In solid state, atoms and molecules in the material hardly move because of very low kinetic energy. In liquid and gas states, neutral particles move freely in the space because the kinetic energy is higher than that of solid state. If the energy applied to matter is increased more from gas state, neutral particles can be splitted into electrons and ions, that is, ionization. This fourth state of matter is called ionized gas or “Plasma”.

Any ionized gas cannot be called a plasma. Plasma always containing electrons, ions (positive and negative ions of atoms and molecules) and neutral atoms and/or molecules. Thus, plasma is microscopically charged negatively or positively because it contain both negative and positive species. In plasma state, however, negative and positive charged particle move collectivity. In addition, plasma containing the same number of negative and positive species. Consequently, plasma is electrically neutral in macroscopic view if characteristic length is much longer than the Debye length. In summary, *A plasma is a quasi-neutral gas of charged and neutral particles which exhibits collective behavior.* This is a fundamental and useful definition of plasma [1].

As already described above, plasma contains electrons and other neutral and charged particles. The mass of electron is much lighter than other particles. Thus ions and neutral particles are often classified “heavy particle”. Due to differences of particle mass, electron

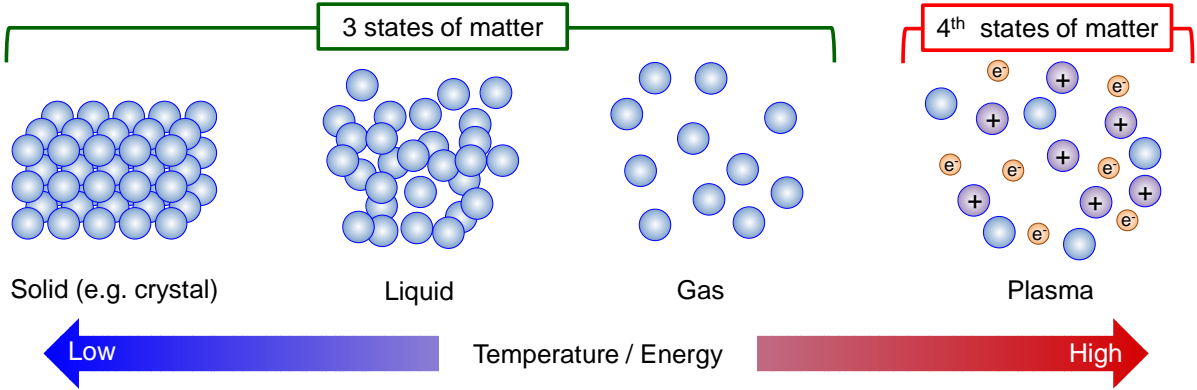


Fig. 1.1: States of materials.

and other heavy particle often have different kinetic energy in the plasma. Thus, electron and other heavy particle often have different kinetic temperature as discussed in the following paragraph.

1.1.2 Concept of temperature

Plasma is composed by electrons, ions and neutral particles. Because of large mass difference between electron and other heavy particle, the electron and other heavy particle can obtain different kinetic energy (i.e. kinetic temperature). The kinetic temperature of the electron and other heavy particles are expressed as “electron temperature” and “heavy particle temperature”, respectively. These temperatures in plasma are defined by average kinetic energy of that particle. If the particles follow a Maxwell-Boltzmann distribution, average kinetic energy can be expressed as follows [2, 3]:

$$\frac{1}{2}m\overline{v^2} = \frac{3}{2}kT \quad (1.1)$$

where m is the mass of particle, $(\overline{v^2})^{1/2}$ is its root mean square velocity, k is the Boltzmann constant, and T is the kinetic temperature. Thus, to describe kinetic energy or other parameters in the plasma on a macroscopic scale, microscopic properties have to be averaged. For this purpose, the velocity distribution function of the particle should be introduced.

The velocity distribution function $f(\vec{v}, \vec{r}, t)$ depends on the space coordinate \vec{r} , and velocity \vec{v} at that coordinate and time t . The number of particle dwelling in the volume

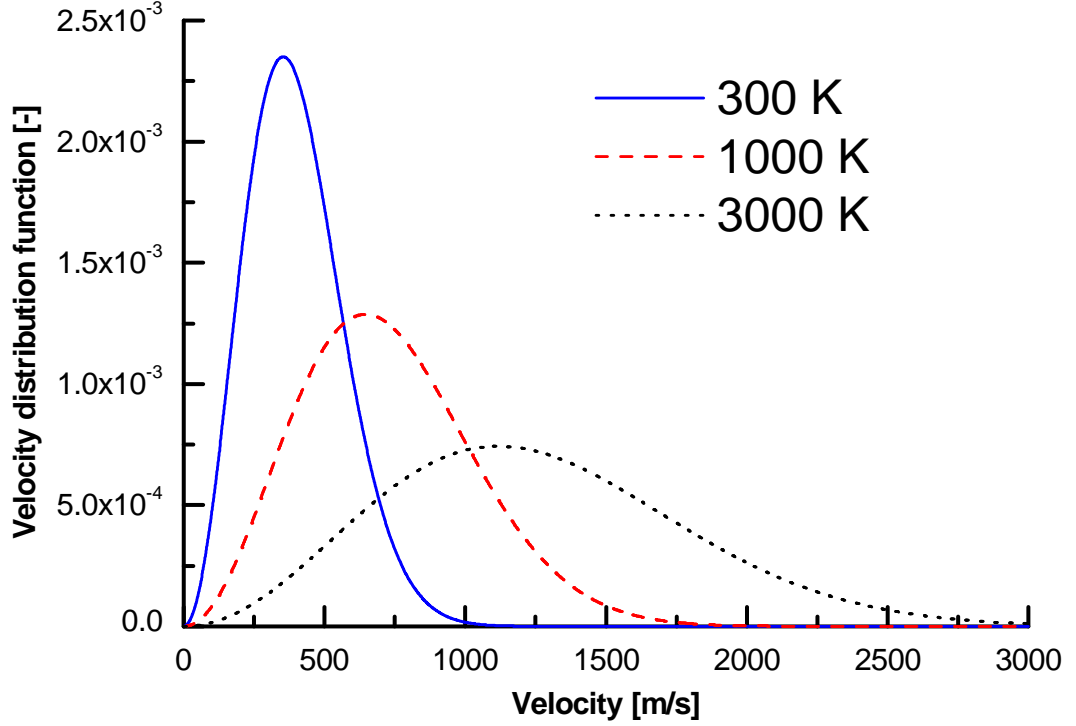


Fig. 1.2: Maxwell-Boltzmann velocity distribution of Argon atom as function of velocity and temperature.

element $dx dy dz (=d\vec{r})$ and having velocities in the velocity element $\vec{v} \rightarrow \vec{v} + d\vec{v}$ is given by following equation:

$$\Delta N = f(\vec{v}, \vec{r}, t) \cdot d\vec{v} \cdot d\vec{r} \quad (1.2)$$

where N is the total number of particle. Thus, the integration of Eq. (1.2) over the total velocity space gives the total particle number density $n(\vec{r}, t)$

$$n(\vec{r}, t) = \int f(\vec{v}, \vec{r}, t) d\vec{v} \quad (1.3)$$

The velocity distribution function $f(\vec{v}, \vec{r}, t)$ gives existence probability of particle at that velocity.

Some distribution functions are studies and found. One of the famous distribution function is the Maxwell-Boltzmann distribution function. If the collision frequency between each particles are very high, energy of each particles are fully exchanged. Thus, this high collision frequency leads a plasma to complete-equilibrium state. Under the complete-equilibrium state, the distribution function is steady, uniform, and isotropic. The number

of particles having velocities between $v \rightarrow v + dv$, in random directions at an absolute temperature T is expressed by

$$\frac{dN(v)}{N_{\text{tot}}} = f(v)dv = \frac{4\pi v^2 dv}{(2\pi kT/m)^{3/2}} \exp\left(-\frac{mv^2}{2kT}\right) \quad (1.4)$$

Fig. 1.2 shows the velocity distribution function of Argon (Ar) atom as functions of temperature and velocity. When the plasma has high temperature, particles in the plasma can obtain high energy, thus the proportion of higher speed particles is increased.

These distribution function is very important property to determine the temperature in the plasma. There are some kinds of “temperature” in the plasma; electron temperature, heavy particle temperature, rotational and vibrational temperature of diatomic molecule, and excitation temperature. Former two temperatures, electron temperature and heavy particle temperature, are based on the kinetic energy of the translational motion of these particles. In the following section, the temperature based on the energy of the translational motion of particle is described as temperature for simplicity.

1.1.3 Classification of plasma by temperature

Various kinds of plasma sources have been found and developed up to now. Each type of plasma has typical temperature and electron density as shown in Fig. 1.3. Thus, “temperature” is one of the important parameter to classify plasmas.

As already described above section, plasma has various kinds of temperature, and electron and heavy particle temperatures are most fundamental temperature in plasmas. Thus in this section, plasmas are classified by temperature differences between electron and heavy particle.

If heavy particle temperature is equal to electron temperature, that plasma is called “thermal equilibrium plasma (thermal plasma)”. Thermal plasma has very high gas temperature up to few thousands kelvin or few tens thousands kelvin. Because of its high temperature, thermal plasma also has high chemical activity field. These high temperature and high chemical activity field enable us to use thermal plasma for various kinds of material processing such as nanopowder synthesis, surface modification, deposition, arc cutting and welding, and combustion processes.

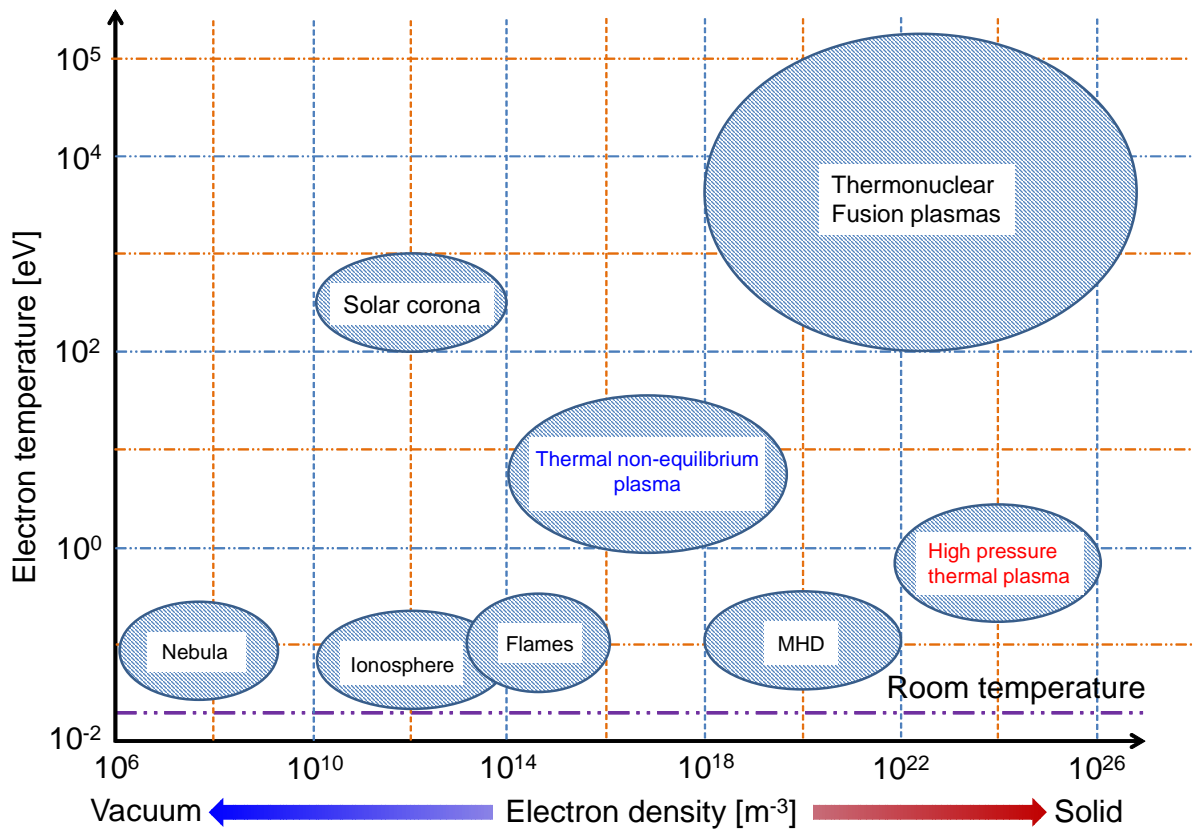


Fig. 1.3: Classification of plasmas by electron temperature and electron density.

In contrast, if heavy particle temperature is not equal to electron temperature, that plasma is classified “thermal non-equilibrium plasma”. Non-thermal plasma has lower gas temperature compared with electron temperature. Gas temperature in non-thermal plasma is close to room temperature. However, the electron temperature often have few eV for thermal non-equilibrium plasma. If gas temperature is lower than room temperature, that plasma is categorized into cryo-plasma. Non-thermal plasma is generally used for low temperature process such as medicine, sterilization, semiconductor manufacturing, and so on.

The thermal plasma and its application are mainly discussed in this thesis.

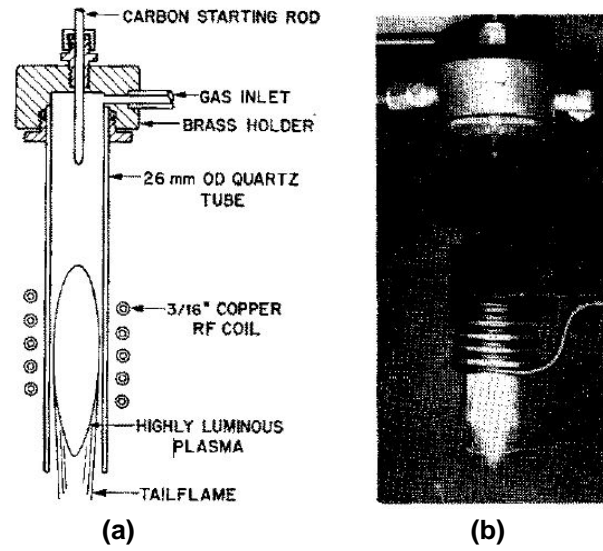


Fig. 1.4: Inductively coupled thermal plasma system [4].

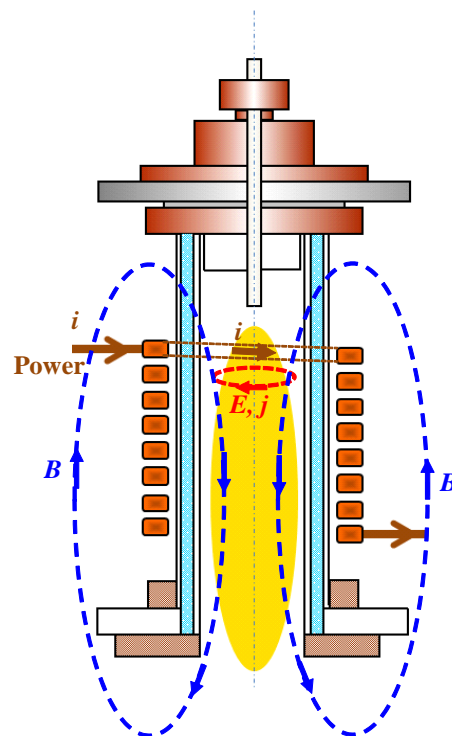


Fig. 1.5: Schematic of ICTP torch.

1.2 Inductively coupled thermal plasma system

An RF discharge can be maintained either by capacitive coupling or inductive coupling with the power source. An inductive coupling discharge is often called “inductively coupled (thermal) plasma”, and maintained by the time-varying magnetic field generated by high frequency (e.g. few hundreds kHz to few MHz) coil-current [2]. The inductively coupled thermal plasma (ICTP) is firstly established by T. B. Reed as shown in Fig. 1.4 [4]. Fig. 1.4(a) shows diagram of apparatus and drawing of torch and (b) illustrates photograph of 1.5 kW plasma torch firstly established by T. B. Reed. In the ICTP torch, an induction coil is installed around quartz tube and it is connected to the RF power supply. An induction thermal plasma is established inside of the quartz tube. In this type of plasma source, the electrode and a plasma are spatially separated as shown in Fig. 1.4. Thus, in principle, a high purity plasma is easily formed inside the quartz tube because there is no contamination originated from suppering of electrode material. Fig. 1.5 shows a principle of an ICTP [2]. In a RF-ICTP system, RF current is supplied into the induction coil to generate alternating magnetic field inside and outside of quartz tube. Due to alternating magnetic field, rotational electric filed is also induced inside the quartz tube as shown in Fig. 1.5. Charged particles are accelerated by electric field, and then particles collides with each other to ionize itself. Finally, an initial plasma is established inside quartz tube. After starting of a plasma, the plasma is maintained by induction heating. As already described, alternating magnetic field induces an electric ring field as shown in Fig. 1.5, which also drives a current of density j . The plasma can be heated by joule-heating of induced eddy current, and then the plasma temperature reaches extremely high temperature.

In the ICTP torch, the temperature distribution shows characteristic peak at off-axis region. This characteristics temperature peak is primarily due to the skin effect. Since the plasma has a relatively high electrical conductivity, the alternating magnetic field cannot penetrate the plasma. The penetration length of the electromagnetic field is quantified as skin depth δ . The skin depth is expressed by

$$\delta = \left(\frac{1}{\pi f \sigma \mu} \right)^{\frac{1}{2}} \quad (1.5)$$

where σ is the electrical conductivity of the plasma, f is the frequency of the current, and μ is the permeability of the plasma. According to Eq. (1.5), alternating electromagnetic

field cannot penetrate into the plasma especially in case of high coil current frequency.

1.3 Nanoparticles

1.3.1 Overview of nanoparticle

Nanopowders and nanoparticles are defined as particles with diameters less than a hundred nanometer. One of the important parameter of nanoparticles is its specific surface area. The specific surface area is defined by surface area per unit volume. The specific surface area of nanoparticle is much larger than that of bulk material. Thus, efficiencies of reaction occurring on the particle surface (e.g. chemical reaction, photocatalysis) are remarkably higher compared with that of bulk material. In addition, when particle size becomes less than the wavelength of light and magnetic domain of material, then new chemical, optical, physical, electrical and quantitative characteristics can appear. One of the famous effect for nanoparticle is that for gold nanoparticles. Fig. 1.6 shows color of gold nanoparticle solutions for different particle size [6,7]. As shown in this figure, the color of solutions changed depends on size of gold nanoparticle. This effect is known as surface plasmon resonance on gold particle surface. These nanoparticles are anticipated as next generation material because of the above unique characteristics.

Nanoparticle consists of countable atoms or molecules. Therefore, even slight impurities of countable atoms or molecules can change the nanoparticle properties. In addition, a large scale production method is also important on the practical situation. Thus, both high quality and mass production are important subject to use nanoparticle in industrial applications. Here “quality” means purity, dispersiveness, uniform structure, and stability of characteristics.

To achieve both subject, many kinds of nanoparticle synthesis process have been investigated and developed up to now. In the next section, nanoparticle synthesis methods are briefly introduced.

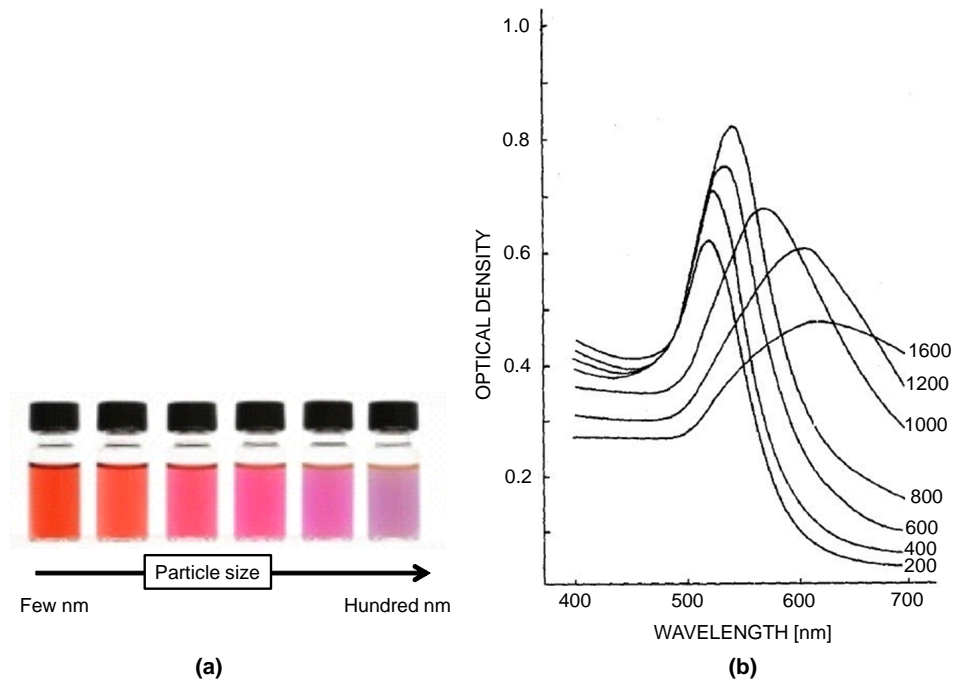


Fig. 1.6: Color and absorption spectra of gold solution. (a) Color of different-size gold nanoparticle solutions [6]. (b) Absorption of colloidal gold found experimentally [7]. Numbers on curves indicate particle diameters in $\text{Å}(10^{-10})$ units. For small (~ 30 nm) monodisperse gold nanoparticles, blue-green light (wavelength $\lambda \sim 450$ nm) is absorbed while red light ($\lambda \sim 700$ nm) is reflected. Thus, solution color is rich red color. As increasing particle sizes, absorbance of red light is increased while blue light is reflected. Consequently solution color becomes pale blue or purple color.

1.3.2 Nanoparticle synthesis method

1.3.2.1 Overview of nanoparticle synthesis method

Various kinds of nanoparticle synthesis methods have been developed so far. Nanoparticle synthesis processes are classified into two types processes, break down process and build up process. Break down process including method using solid precursor (solid phase method) and build up process including method using liquid and gas precursor (liquid phase method and gas phase method). The overview of breakdown process and build up process are illustrated in Fig. 1.7 [8].

In the break down process in solid phase method, precursor of particle is bulk material.

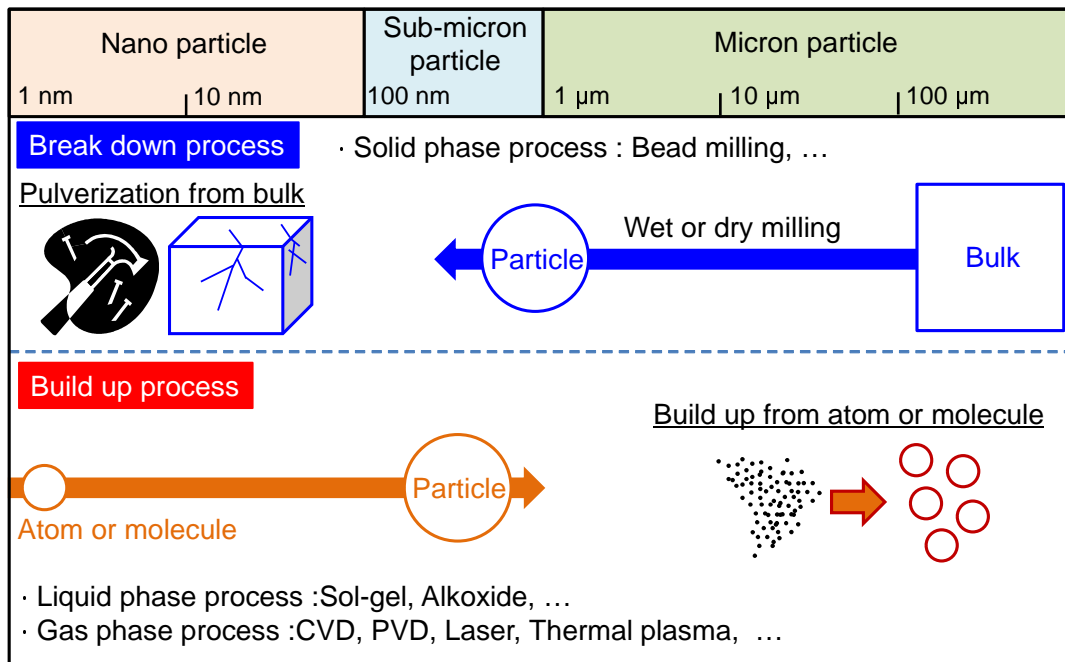


Fig. 1.7: Overview of nanoparticle synthesis method.

Bulk material is pulverized by the applying of mechanical energy by milling with small beads in the wet (in liquid) or dry environment. Solid phase method is very simple method. However, it is hard to synthesize nano-size particle because of mitigation of mechanical energy by the interaction between small particle-particle or bead.

In case of liquid or gas phase processes, nanoparticle is synthesized by chemical reaction in liquid or gas phase. In liquid phase process, it is relatively easy to synthesize homogeneous particles. However, synthesized particle fundamentally contains contamination because the feedstock include particles other than the precursor in the liquid phase process.

Nanopowder synthesis method using laser and thermal plasma are categorized as gas phase method. In gas phase method, feedstock is evaporated or vaporized to form precursor particles, then nanoparticles are synthesized from precursor vapor by condensation and agglomeration processes. Various kinds of thermal plasma are used as heat source, e.g. transfer and non-transfer arc plasma, inductively coupled thermal plasma, hybrid plasma and so on. The common benefit of gas phase method is that it can easily produce nanoparticle in vary short time.

1.3.2.2 Nanopowder synthesis using inductively coupled thermal plasmas

Nanoparticle synthesis method using inductively coupled thermal plasma (ICTP) , i.e. ICTP method, is one of the gas phase method using a thermal plasma. Fig. 1.8 shows nanoparticle synthesis procedure of ICTP method. For description, titanium dioxide (TiO_2) nanoparticle synthesis process is illustrated in Fig. 1.8 [9, 10]. TiO_2 material is frequently used as photocatalyst and other usefull application [11]– [15]. In the ICTP method, TiO_2 nanopowder can be synthesized through following processes: (a) Evaporation of feedstock material in the thermal plasma to generate mixture of reactive O atom and Ti atom. (b) Chemical reaction between O atom and Ti atom to form monomer species such as TiO or TiO_2 molecules. (c) Monomer species are condensed with/without seed particle to generate clusters (forward reaction). Generated clusters can be evaporated at the same time (backward reaction). Nanoparticle nuclei are synthesized when the cluster size exceeds critical size. (d) Nanoparticle grows by heterogeneous condensation to form primary particle. (e) Synthesized nanoparticles are agglomerated each other to form secondary particles (aggregates). The series of processes take place within a several or several tens milli second in the single device. Main advantages of ICTP method are (a) high temperature and high chemical activity field, (b) no-contamination process due to electrodeless discharge, (c) short processing cycle time. The high temperature field enables in the ICTP method to use not only gas phase and liquid phase feedstock but also solid phase feedstock. The ICTP method with such convenient characteristics has been applied to vairous nanoparticle synthesis [16]– [19]. However, when mass feedstock is injected into the ICTP torch, the plasma temperature is easily decreased. Consequently, complete evaporation of large amount of feedstock is not easy in the ICTP method. This issue makes it not easy to improve the production rate (kg/h). In addition, control of particle size is also not easy in the ICTP method. These two disadvantages are the barrier to use the ICTP method in actual industrial application.

1.3.3 Experimental measurement method of nanoparticle synthesis field

Here, nanopowder synthesis processes are tabulated again as follows:

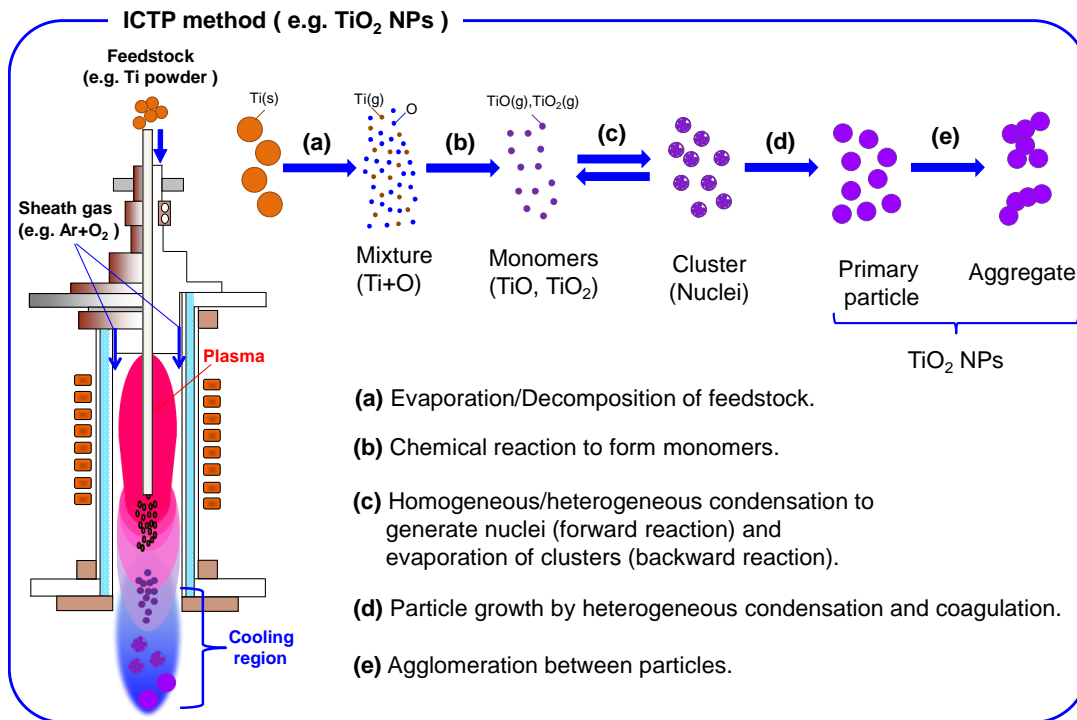


Fig. 1.8: Nanoparticle synthesis process using ICTP method.

1. Feedstock evaporation.
2. Mixing of feedstock vapor with reactive plasma gases.
3. Formation of monomer (precursor) species.
4. Cluster formation and stabilization as nuclei.
5. Nanoparticle growth.
6. Agglomeration of nanoparticles.

These first to third processes are taken place mainly inside the thermal plasma by chemical and physical reactions in it. Especially as a matter related to the first process, feedstock evaporation efficiency directly affects nanoparticle synthesis efficiency. Thus, efficient evaporation is necessary for efficient nanopowder synthesis. The controlling of nanopowder size is an important issue to be improved as already described in previous section. Agglomeration of nanoparticles increases size and decreases specific surface area of particle.

These agglomeration of particle may degrade nanoparticle quality. Therefore, agglomeration should be prevented to the keep nanoparticle quality. From the above reasons, a nanopowder synthesis processes should be understood and clarified in more detail to control these processes in the ICTP method. These processes have been investigated through following experimental measurement.

1.3.3.1 Analysis of chemical composition of synthesis field

The feedstock evaporation, mixing of feedstock vapor and monomer formation processes involve changes in the chemical composition of the thermal plasma. Thus, changing of chemical composition is often investigated for the reaction field inside or outside of the plasma. Optical emission spectroscopy (OES) method or mass spectroscopy (MS) method are often used to investigate chemical composition [23]. The OES method measures elemental composition from the light emitted from particle of interest. Figure 1.9 shows the energy diagram of hydrogen atom. When the excited electrons are de-excited from higher energy level to lower energy level, the energy difference is emitted as light with energy of $h\nu$, where h is the Planck constant and ν is the frequency of light. The energy level and combination of transitions depend on each atoms and molecules. Therefore, the wavelength of emitted light depends on types of atoms and molecules as shown in Fig. 1.10. The radiation intensity of emission spectrum from atomic species is expressed as Eq. (1.6)

$$I = \frac{hc}{\lambda} \frac{N A_{ul} g_u}{Z(T)} \exp\left(-\frac{E_u}{kT}\right) \quad (1.6)$$

where $Z(T)$ is the partition function, N is the number density of particle of interest, A_{ul} is the spontaneous transition probability (Einstein's A coefficient), g_u is the degeneracy at upper state, λ is the wavelength of light, E_u is the energy level at upper state, k is the Boltzmann constant, T is the temperature. As shown in Eq. (1.6), the radiation intensity of emitted light depends on the number density of particles of interest. Thus, we can measure and estimate the elemental composition and number density of particles from the OES measurement result. In case of OES measurement, measurable particles are basically limited to single-atom and diatomic molecules because it is hard to detect optical emission from polyatomic molecules.

The MS method also measure chemical composition of gases. The MS method determine chemical species from difference of particle mass and charge ratio (m/z). Thus, polyatomic molecule can be detected in case of the MS method. However in principle, the MS method can not identify particles with the same m/z value.

1.3.3.2 Particle size measurement

Nanopowder processes after formation of cluster are often investigated from measurement result of cluster/particle size and their distribution. However, the particle size range of interest is so wide from a few nanometers to tens of micrometers. Thus many types of measurement method have been developed based on different physical principles, such as laser-light-scattering (LLS) of particles [21, 22], small angle x-ray scattering (SAXS) of clusters [24, 25], differential mobility analyzer (DMA) for particle [26, 27], and inertia filter using cascade impactor [28, 29]. These methods are used to measure appropriate particle size range.

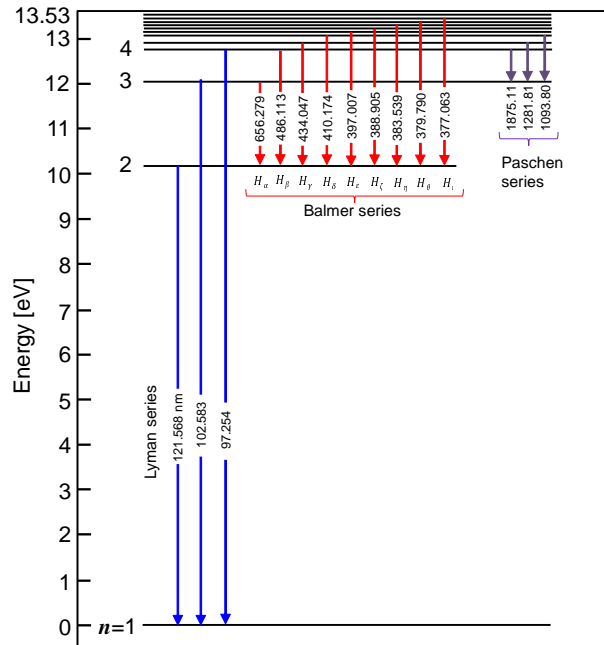


Fig. 1.9: Energy diagram of hydrogen atom and wavelength of emission spectra.

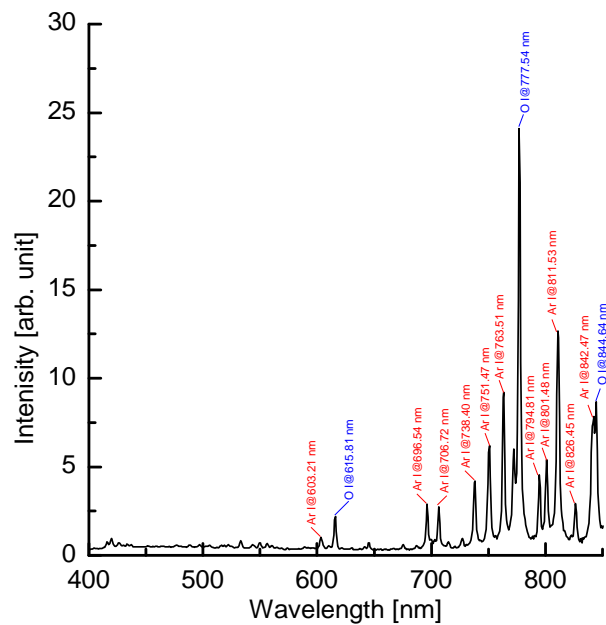


Fig. 1.10: The OES result for Ar-O₂ ICTP.

1.4 Objective of this thesis

“Nano material” is a keyword to progress recent technical society in this world because nano material has unique characteristics different from bulk material. Social demand of nano material keeps increasing day by day in various kind of fields such as electronics, biomedical, energy and so on. To use nano material, high purity process is necessary because nano material is composed by countable number of atoms or molecules. Admixing of few amount of contamination can markedly changes characteristics of nano material. From the above reasons, a large-scale synthesis method is greatly desired for high-purity nanomaterials.

Liquid phase method is recently used to produce nanoparticle in industrial scale. Liquid phase method can synthesize homogeneous nanoparticle with a high energy efficiency because this method use chemical reaction in the liquid solutions. In principal, nanoparticle synthesized by liquid phase method contains some contaminations. This is the serious disadvantage to use synthesized nanoparticle in various kinds of fields.

In contrast to liquid phase method, gas phase method using inductively coupled thermal plasma (ICTP method) can synthesize a high purity nanoparticle with high time efficiency because this method use electrodeless discharge and high temperature and high chemical activity field. However, the ICTP method has some disadvantages as follows: (1) energy efficiency of nanoparticle synthesis is not so high (e.g. few g/hour at the input power of 20 kW). (2) synthesis of homogeneous particles, that is size controlled nanoparticle, is not easy. Therefore, these disadvantages of ICTP method should be improved to use this method as industrial application.

The main objective of this thesis is development of a large-scale nanopowder synthesis method using inductively coupled thermal plasma. To achieve this objective, firstly we developed an unique nanoparticle synthesis method using pulse-modulated induction thermal plasmas. Pulse-modulated induction thermal plasma (PMITP) is a new thermal plasma source developed in our laboratory and PMITP can temporarily control the temperature and chemical activity fields in the torch. In this work, the following aspects will be discussed.

1. Development of a large-scale synthesis method of Al³⁺-doped TiO₂ nanopowder using pulse-modulated induction thermal plasma system.

-
2. Spatiotemporal distribution of feedstock Ti vapor and precursor TiO vapor in ICTP torch during TiO₂ nanopowder synthesis.
 3. Effect of admixing of feedstock vapor in the ICTP.
 4. Spatiotemporal distribution of temperature in the ICTP torch.
 5. Possibility in nanoparticle nucleation in the ICTP torch during TiO₂ nanopowder synthesis.
 6. Spatial measurement of feedstock vapor admixture ratio in the Ar ICTP during Ti nanopowder synthesis.
 7. Spatial estimation of particle number densities for various kind of particles in the Ar ICTP during Ti nanopowder synthesis.

The first aspect was done to investigate a possibility in large-scale nanopowder synthesis using the pulse-modulated induction thermal plasma system. The second to the 7th aspects are essential to understand feedstock evaporation mechanism. Especially for the ICTP method, “spatial measurement” is crucial to understand feedstock evaporation and nucleation possibility because ICTP has large volume processing field. Thus, we newly applied two-dimensional optical emission spectroscopic measurement system to obtain spatiotemporal distribution atomic and molecular spectral radiation intensities. From optical emission measurement results, we fundamentally discussed feedstock evaporation and nucleation processes.

1.5 Composition of the thesis

This thesis is composed from following chapters. In first chapter, which is already described, fundamental informations of plasma and nanopowder were introduced. In second chapter, a large-scale synthesis method using the pulse-modulated induction thermal plasma (PMITP) was investigated for Al^{3+} -doped titanium dioxide (Al^{3+} -doped TiO_2) nanopowder. In third chapter, feedstock evaporation and precursor molecule formation processes were fundamentally investigated from two-dimensional optical emission spectroscopic measurement (2D OES) for an ICTP torch during TiO_2 nanopowder synthesis. In fourth chapter, effect of coil-current modulation and intermittent feedstock feeding on feedstock evaporation and precursor formation were discussed from 2D OES results for PMITP/ICTP torch during TiO_2 nanopowder synthesis. In fifth chapter, spatial distribution of temperature was determined for ICTP torch during TiO_2 nanopowder synthesis and nucleation possibility was simply discussed in the torch. In sixth chapter, Ti vapor admixture ratio, particle number densities were spatially estimated from 2D OES results for Ar ICTP torch during Ti feedstock injection. In final chapter, eighth chapter, is summary of this thesis.

References

- [1] Chen F C 1974 *Introduction to plasma physics vol.1* (New York: Plenum press)
- [2] Boulos M I, Fauchais P and Pfender E 1994 *Thermal plasmas fundamentals and applications vol.1* (New York: Plenum Press)
- [3] Lieberman M A, and Lichtenberg A J 2005 *Principles of plasma discharges and materials processing 2nd ed.* (Wiley Interscience)
- [4] Reed T B 1961 Induction-coupled plasma torch, *J. Appl. Phys*, **32**, pp. 821–4
- [5] Boulos M I 1992 RF induction plasma spraying: state-of-the-art review *J. Thermal Spray Technol*, **1**, pp. 33-40
- [6] SIGMA-ALDRICH web site, “Gold nanoparticle: properties and applications” <https://www.sigmaaldrich.com/technical-documents/articles/materials-science/nanomaterials/gold-nanoparticles.html> , (accessed Nov. 28, 20017)
- [7] Turkevich J, Garton G, Stevenson P C 1954 The color of colloidal gold, *J. Colloid Sci.*, **9**, pp. 26-35 (1954)
- [8] National center for industrial property information and training 2006 *Nanoparticle manufacturing technology* (in Japanese)
- [9] Nakaso K, Fujimoto T, Seto T, Shimada M, Okuyama K, and Lunden M M 2001 Size distribution change of titania nano-particle agglomerates generated by gas phase reaction, agglomeration, and sintering, *Aerosol Sci, Technol.*, **35**, pp. 929-47 (2001)
- [10] Friedlander S K 2000 *Smoke, dust and haze, fundamentals of aerosol dynamics 2nd ed.* (New York: Oxford university press)

-
- [11] Hashimoto K, Hiroshi I, and Akira F 2005, TiO₂ photocatalysis: a historical overview and future prospects, *Jpn. J. Appl. Phys.*, **44**, pp. 8269-85
- [12] Linsebigler A L, Lu G, and Yates J T 1995, Photocatalysis on TiO₂ surfaces: principles, mechanisms, and selected results, *Chem. Rev.*, **95**, pp. 735-58
- [13] Giacomo Barolo, Stefano Livraghi, Mario Chiesa, Maria Cristina Paganini, and Elio Giamello 2012, Mechanism of the photoactivity under visible light of N-doped titanium dioxide. Charge carriers migration in irradiated N-TiO₂ investigated by electron paramagnetic resonance, *J. Phys. Chem. C*, **116**, pp. 20887-94
- [14] Huang C M, Chen L C, Cheng K W, and Pan G T 2007 Effect of nitrogen-plasma surface treatment to the enhancement of TiO₂ photocatalytic activity under visible light irradiation, *J. Mol. Catal. A: Chem.*, **261**, pp. 218-24
- [15] Mio M, Kogoma M, Fukui H and Takeda A 2010 Control of inflammation using adsorption of inflammatory by nano-particles *Chem. Eng.*, **55**, pp. 603-8 (In Japanese)
- [16] Hollabaugh C M, Hull D E, Newkirk L R and Petrovic J J 1983, R.F.-plasma system for the production of ultrafine, ultrapure silicon carbide powder, *J. Mater. Sci.*, **18**, pp. 3190-4
- [17] Zhang H, Bai L, Hu P, Yuan F and Li J 2012 Single-step pathway for the synthesis of tungsten nanosized powders by RF induction thermal plasma, *Int. J. Refract. Met. Hard Mat.*, **31**, pp. 33-8
- [18] Karoly Z, Mohai I, Klebert S, Keszler A, Sajó I E and Szepvolgyi J 2011, Synthesis of SiC powder by RF plasma technique, *Powder Technology*, **214**, pp. 300-5
- [19] Samal S, Kim D W, Kim K W and Park D W 2012 Direct synthesis of TiO₂ nanoparticles by using the solid-state precursor TiH₂ powder in a thermal plasma reactor, *Chem. Eng. Res. Des.*, **90**, pp. 1074-81
- [20] Tanaka Y, Takeuchi Y, Sakuyama T, Uesugi Y, Kaneko S and Okabe S 2008 Numerical and experimental investigations on thermal interaction between thermal plasma and solid polymer powders using induction thermal plasma technique, *J. Phys. D: Appl. Phys.*, **41**, 025203

-
- [21] H C van den Hulst 1981 *Light scattering by small particles* (New York: Dover Publications)
- [22] Nunomura S, Kita M, Koga K, Shiratani M, and Watanabe Y 2006 In situ simple method for measuring size and density of nanoparticles in reactive plasmas, *J. Appl. Phys.*, **99**, 083302
- [23] Montaser A and Golightly D W 1992 *Inductively coupled plasmas in analytical atomic spectrometry 2nd ed.* (New York: VCH Publishers)
- [24] Stasio S D, Mitchell J B A, LeGareec J L, Biennier L, and Wulff M 2006 Synchrotron SAXS; in situ identification of three different size modes for soot nanoparticles in a diffusion flame, *Carbon*, **44**, pp. 1267-79
- [25] Diaz J M A, Kambara M, and Yoshida T 2006 Detection of Si nanoclusters by x-ray scattering during silicon film deposition by mesoplasma chemical vapor deposition, *J. Appl. Phys.*, **104**, 013536
- [26] Knutson E O and Whitby K T 1975 Aerosol classification by electric mobility: apparatus, theory, and applications, *J. Aerosol Sci.*, **6**, pp.443-51
- [27] Seto T, Nakamoto T, Okuyama K, Adachi M, Kuga Y and Takeuchi K 1997 Size distribution measurement of nanometer-sized aerosol particles using DMA under low-pressure conditions, *J. Aerosol Sci.*, **28**, pp.193-206
- [28] May K R 1945 The cascade impactor: An instrument for sampling coarse aerosols, *J. Sci. Instrum.*, **22**, pp.187-95
- [29] Mitchell R I and Pilcher J M 1959 Improved cascade impactor for: measuring aerosol particle size, *Ind. Eng. Chem.*, **51**, pp.1039-42
-

Chapter 2

Large-scale synthesis of Al^{3+} -doped TiO_2 nanopowder using pulse-modulated induction thermal plasmas

2.1 Introduction

Nanopowder or nanoparticles are anticipated as promising next-generation elements for use in various applications such as in electronics, energy, and environmental fields. Titanium dioxide (TiO_2) nanopowder is continually receiving attention for use as photocatalysts [1], photonic crystals [2], photovoltaic cells [3], and gas sensors [4]. It is also anticipated for use as a strong deoxidation material used for producing hydrogen gas from water for fuel cells [5]. In fact, TiO_2 is well known to work as a photocatalyst under ultraviolet light because of its wide energy band gap. This problem can be improved by metallic-ion doping of TiO_2 materials because the energy levels of the doped material in the energy band gap of TiO_2 improve their visible light absorption efficiency [5]– [7]. Another application of such metallic-ion doped TiO_2 nanoparticles is in the biomedical field [7, 8]. Reportedly, Al^{3+} -doped TiO_2 nanoparticles have inflammatory protein adsorption ability [7]. This adsorption effect might be attributed to the fact that Al^{3+} -doped TiO_2 nanoparticles are positively charged in water dispersion, which can attract inflammatory proteins with a negatively charged functional group. For such biomedical applications, an effective method for mass production of Al^{3+} -doped TiO_2 nanopowder without impurity is strongly desired from an

industrial view point. Nevertheless, it has not yet been developed for such metallic-ion doped TiO₂ nanopowder without impurity contamination.

Various types of nanopowder synthesis methods have been developed. Among them, the inductively coupled thermal plasma (ICTP) method is a useful technique to synthesize nanoparticles of various kinds [2]– [18]. It provides one-step direct processing including rapid evaporation of injected raw materials, and enables rapid cooling of evaporated materials. It can offer nanoparticles in non-equilibrium or metastable phase. The most important benefit of this method is that it can fundamentally provide nanoparticles without any impurity. Several studies have examined the synthesis of TiO₂ nanoparticles using a steady-state type of inductively coupled thermal plasma (ICTP). They have mainly investigated control of its particle size and phase constituent [3, 14, 18]. However, some issues persist: the difficulty in controlling the synthesized particle size, and also the lower production rate from the instability of ICTP sustainability during heavy-load feeding of feedstock.

The authors recently developed a new synthesis method of large amounts of pure oxide nanopowder without contamination using pulse-modulated induction thermal plasma (PMITP) with time-controlled feeding of feedstock (TCFF) [19]– [21]. The PMITP was developed by our group to control the temperature and chemical activity fields in thermal plasmas using coil-current modulation [23, 24]. In addition to this, our group recently developed a method for feedstock powder injection, in which the feedstock powder is supplied intermittently to the thermal plasma periodically, in synchronization with the coil-current modulation of the PMITP. This intermittent and synchronized feeding of feedstock is a time-controlled feedstock feeding (TCFF) method [21, 22]. The TCFF was combined with the PMITP for nanopowder synthesis. This PMITP–TCFF method accommodates heavy-load feeding of feedstock powder, thereby providing complete evaporation. In our previous work, the PMITP+TCFF method developed as explained above was adopted to synthesize pure TiO₂ nanopowder for mass production. Results show that this method using a 20-kW PMITP supported a production rate of about 500 g h⁻¹ of pure TiO₂ nanopowder with mean particle diameter of about 43 nm [21].

This chapter describes the experimental results of trial adoption of our uniquely-developed PMITP+TCFF method to synthesize large amounts of Al³⁺-doped TiO₂ nanopowder, as well as TiO₂ nanopowder. Mass production of metallic-ion doped nanopowder is a key issue

in nanotechnology fields for various applications including skincare creams for anti-atopic dermatitis. The synthesized nanopowder was analyzed using different methods, including FE-SEM, to assess the morphology of nanoparticles and their size distribution, XRD and TEM/EDX mapping for the crystal phase composition of the particle and the estimation of Al doping, XPS for estimation of the chemical-bonding state in the particles, and spectrophotometry for optical property evaluation. In addition, the effects of the degree of coil-current modulation were particularly investigated in the synthesized nanopowder. The Al³⁺-doped TiO₂ nanopowder was synthesized using our originally developed PMITP+TCFF method. The Al³⁺-doped TiO₂ nanopowder production rate was finally estimated as about 400 g h⁻¹ using a 20-kW PMITP, which is about 10 times higher than that attained using the conventional method with steady-state induction thermal plasmas.

2.2 Methodology of a large-scale nanopowder synthesis system

Here, our developed method is described briefly for synthesis of large amounts of nanopowders using a PMITP+TCFF, although it has been described in our previous paper [21].

We have developed a pulse-modulated induction thermal plasma (PMITP) system. The PMITP is sustained by the coil current on the order of several hundreds of amperes, the amplitude of which is modulated into a rectangular waveform. Such modulation of the coil current can repetitively produce a high-temperature field during the ‘on-time’ and a low-temperature field during ‘off-time’ in thermal plasmas. Figure 2.1 portrays the coil current modulated into a rectangular waveform and the definition of modulation parameters. As presented in figure 2.1, the on-time is the time period with the higher current level (HCL), although the off-time means the time period with the lower current level (LCL). We have also defined a shimmer current level (SCL) as a ratio of LCL to HCL. In addition, the duty factor (DF) has been defined as the ratio of on-time in one modulation period. A condition of 100%SCL or 100%DF corresponds to the non-modulation condition. A lower SCL condition is equivalent to a condition with a larger modulation degree.

Figure 2.2 presents our developed methodology for the synthesis of large amounts of nanopowder using a pulse-modulated induction thermal plasma (PMITP) with time-controlled

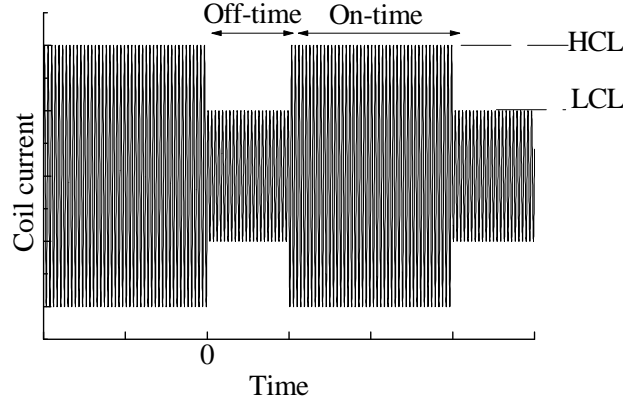


Fig. 2.1: Modulated coil current and definition of modulation parameters.

feeding of the feedstock (TCFF). As explained earlier, the PMITP can produce a higher temperature field and a lower temperature field repetitively according to the coil current modulation. To this PMITP, the feedstock solid powder is supplied from a powder feeder through a powder feeding tube with Ar carrier gas from the top of the plasma torch head to the PMITP. Furthermore, a high speed valve is installed on the tube between the powder feeder and the plasma torch. This high-speed solenoid valve has a response time of 2 ms to open and close. Setting the open and close timing of the valve can control the actual timing and the time length of the powder feeding. The right hand side of figure 2.2 shows the timing chart of the coil current modulation, switching signal of the solenoid valve, and the actual powder feeding. For synthesis of large amounts of nanopowder, heavy-load feeding of feedstock is necessary without extinction of the plasma or incomplete evaporation of the feedstock. In our method, the feedstock powder is controlled to be fed intermittently and synchronously only during the high-temperature period in the on-time of the PMITP. This synchronized powder feeding can be executed easily by controlling the delay time t_d for the opening timing of the valve in reference to the pulse modulation signal of the PMITP. In the actual experiment, the powder reaches to the PMITP in a finite time after inputting the opening signal to the solenoid valve. This finite time was measured in our previous work as another delay time t_{adt} of 6–8 ms [21]. Therefore, the actual total delay time is $(t_d + t_{adt}) \simeq (t_d + 7)$ ms before the powder is actually injected to the PMITP. The intermittent and synchronized feedstock feeding can be performed while taking account of this total delay time $(t_d + 7)$ ms.

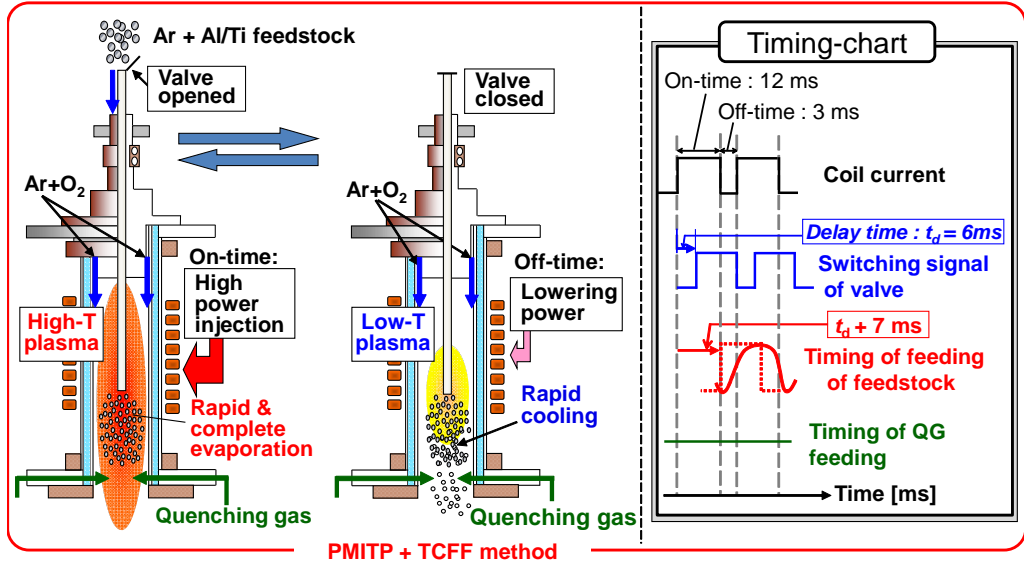


Fig. 2.2: Method for large-scale nanopowder synthesis using pulse-modulated induction thermal plasma with time-controlled feedstock feeding (PMITP+TCFF).

The injected feedstock powder with heavy-load is evaporated rapidly, completely, and efficiently in a high temperature plasma during the on-time of the PMITP because of higher power injection to the PMITP. The feedstock injection is stopped by closing the solenoid valve during the successive off-time. In the off-time, the evaporated feedstock material is cooled down rapidly because the thermal plasma temperature decreases as a result of the decreased input power to the PMITP. This rapid cooling might promote particle nucleation from evaporated Ti and O atom in vapour in the PMITP. Nucleated particles are transported downstream of the PMITP torch with particle growth. Downstream of the PMITP torch, the quenching gas is injected in the radial direction. Such a quenching gas injection cools the evaporated material further to restrain the synthesized particle growth. Then, in the successive on-time, the input power increases to rebuild high-temperature thermal plasma for the subsequent powder injection. In this way, the PMITP+TCFF method described above can create effective vaporization of the feedstock and support the effective cooling of the evaporated material. It enables synthesis of large amounts of nanopowder with a high production rate.

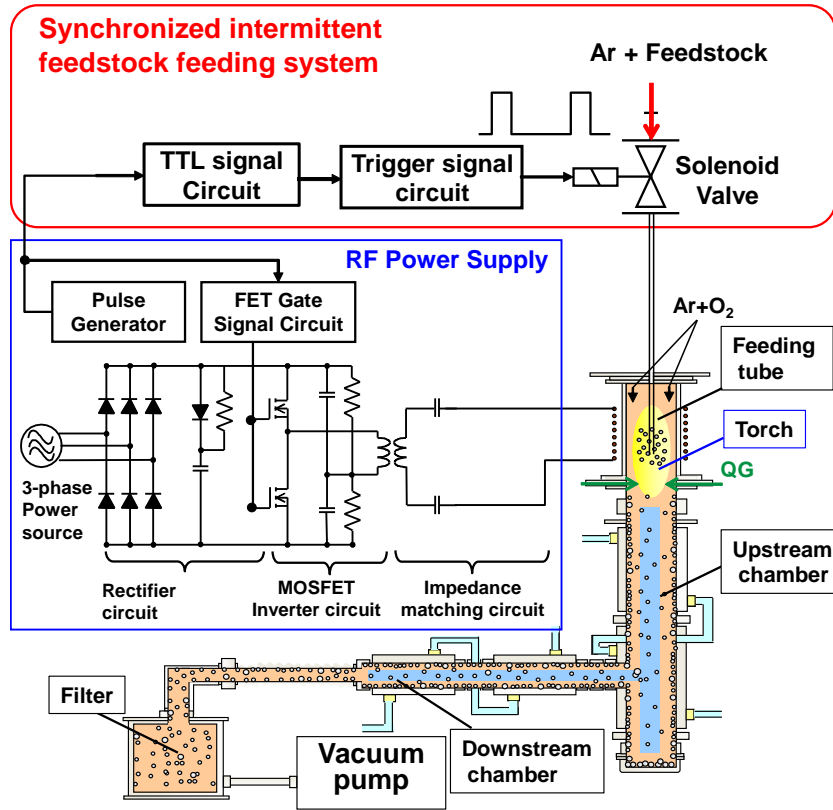


Fig. 2.3: Whole system of nanopowder synthesis using PMITP+TCFF.

2.3 Experimental setups

2.3.1 Experimental arrangements

Figure 2.3 shows the whole nanopowder synthesis system used in the present experiments. This nanopowder synthesis system has three main parts: an rf power source, a synchronized intermittent feedstock feeding system, and the plasma torch and the chamber. The rf power source is operated as a half-bridge inverter power supply with a metal-oxide semiconductor field emission transistor (MOSFET) at rated power of 30 kW. Its driving fundamental frequency was 450 kHz. This power supply can modulate the output electric current amplitude of several hundreds of amperes into a rectangular waveform according to the modulation signal from the pulse generator.

The synchronized intermittent feedstock feeding system has the transistor-transistor logic (TTL) signal circuit, a delayed trigger signal circuit, the high-speed solenoid valve on

the powder feeding tube, and the powder feeder. The TTL signal circuit translates a modulation signal of 0–10 V from the pulse generator for the MOSFET gate signal circuit to a TTL signal of 0–5 V. This TTL signal is inputted to the delayed trigger circuit, which outputs a TTL signal with a given delay time of t_d against the modulation signal. This delayed signal is used to open and close the high speed solenoid valve for powder feeding.

The plasma torch is configured identically to that used in our previous work. Its details were described in elsewhere [23, 24]. The plasma torch has two coaxial quartz tubes. The interior quartz tube has 70 mm inner diameter; its length is 370 mm. An argon–oxygen gas mixture was supplied as a sheath gas along the inside wall of the interior quartz tube from the top of the plasma torch. A powder mixture of titanium (Ti) and aluminium (Al) raw materials was fed using a powder feeder with Ar carrier gas through a water-cooled tube probe. The water-cooled tube probe was inserted from the top of the plasma torch head, as depicted in figure 2.3. Downstream of the plasma torch, quenching gas was supplied to cool down the evaporated material to promote nucleation. Further downstream, the water-cooled chambers were installed vertically and then horizontally, as depicted in figure 2.3. The total length of the vertical chamber is 600 mm; its inner diameter is 130 mm. Similarly, the total length of the horizontal chamber is 600 mm; its inner diameter is 130 mm. Further downstream of the horizontal chamber, a powder-collecting filter and the collecting chamber are set up. A vacuum pump is set up further downstream.

2.3.2 Experimental condition

Table 2.1 summarizes the experimental conditions in the present work. The time-averaged input power was fixed at 20 kW to the inverter power supply. This inverter power supply in the experiment was a semiconductor power supply with fundamental frequency of 450 kHz. This power supply was measured to have high power conversion efficiency of more than 95%. Therefore, the greater than 19 kW was outputted from the power supply. The instantaneous input power $P_{in}(t)$ was also changed periodically with time according to the coil current modulation. For 80%SCL-80%DF condition for example, the quantity $P_{in}(t)$ increased gradually with a time constant of about 1.6 ms during the on-time and reached 28 kW, although it decreased with a time constant of 2.0 ms during the off-time, reaching 10 kW. The modulation cycle was fixed at 15 ms. The reason to select the modulation

Table 2.1: Experimental conditions.

Time-averaged input power	20 kW
Fundamental frequency of the coil current	450 kHz
Modulation cycle	15 ms
Shimmer current level, SCL	60%, 70%, 80%
Modulation time	15 ms
Duty factor, DF	80% (On-time / Off-time = 12 ms / 3 ms)
Pressure	300 torr (= 40 kPa)
Gas composition	Ar: 90 L min ⁻¹ , O ₂ : 10 L min ⁻¹
Carrier gas flow rate	Ar: 4 L min ⁻¹
Quenching gas flow rate	Ar: 50 L min ⁻¹
Open and close time of solenoid valve	12 ms for open and 3 ms for close
Delay time of solenoid valve open t_d	6 ms
Powder feed rate g_{pow}	19 g min ⁻¹ for 60%SCL, 12 g min ⁻¹ for 70%SCL and 80%SCL
Raw powder and its maximum size	95wt%Ti + 5wt%Al, $\bar{d}_{\text{Ti}} = 27 \mu\text{m}$, $d_{\text{Ti}} < 45 \mu\text{m}$ $\bar{d}_{\text{Al}} = 3 \mu\text{m}$

cycle of 15 ms is attributed to the fact that the residence time of the reactant vapour was estimated as 10–20 ms according to the gas flow velocity calculation by numerical thermo-fluid simulation [19]. It is expected for this time period to provide sufficient evaporation of the injected powders in the high-temperature region in the plasma during the on-time, and successive rapid cooling of the plasma tail during the off-time. The DF of the modulated coil current was fixed at 80%. Only the modulation degree, i.e. the shimmer current level (SCL), was changed to 60%, 70% and 80%.

The total sheath gas flow rate was fixed at 100 L min⁻¹ (litres per minute). The O₂ gas admixture ratio to Ar was set at 10 mol% in the sheath gas in gas flow rate. The Ar quenching gas flow rate was fixed at 50 L min⁻¹. The chamber pressure was fixed at 300 Torr

(=40 kPa). The feedstock was a mixture of 5 wt%Al (ALE11PB; Kojundo Chemical Lab. Co. Ltd.) and 95wt%Ti (TILOP-45; Osaka Titanium Technologies Co., Ltd.) powder. The mean diameter of Al raw powder is about 3 μm , whereas that of Ti raw powder was 27 μm . The feedstock was fed into the plasma torch using a rotary powder feeder with Ar carrier gas. The Ar carrier gas flow rate was fixed at 4 L min^{-1} . The feeding rate of the feedstock g_{pow} was found to be 19 g min^{-1} at 60%SCL, 12 g min^{-1} at 70%SCL and 12 g min^{-1} at 80%SCL, respectively, by weight measurements after each of the experiments. These powder feeding rates are much higher than those in other conventional nanoparticle synthesis methods described in the literature. They used induction thermal plasmas of several tens of kilowatts [5, 14]. The feedstock was fed intermittently with a high-speed solenoid valve that was synchronized with the coil current modulation with delay time t_d of 6 ms. The open time and close time of the high-speed solenoid valve were, respectively, 12 ms and 3 ms.

Nanopowder synthesis experiments were conducted for 5 min for each of the experiments under three SCL conditions. After each experiment, synthesized powder was collected at the filter. Morphology and size distribution of synthesized powder were analyzed using a field emission scanning electron microscope (FE-SEM) and a bright-field transmission electron microscope (BF-TEM). The FE-SEM analyses were carried out on a JEOL JSM-6700F operated at 5 kV. The crystal phase composition was identified using X-ray diffraction (XRD) spectroscopy. The XRD measurements were carried out on a Rigaku RINT-Ultima III operated at 40 kV and 40 mA. The element distribution of Ti, O and doped Al atom was mapped using TEM / energy dispersive X-ray (EDX) spectrometry. The chemical-bonding state of in the synthesized powder was estimated using X-ray photo-electron spectroscopy (XPS) on a carbon-tape. The XPS measurements were carried out on a Thermo VG Scientific Sigma Probe using monochromatic AlK_α radiation. The calibration of peak positions was made using the C 1s line at 285 eV after experimental acquisitions, because the carbon originated from carbon-tape was well detected. The spot-size of XPS measurements were 400 μm with pass energy of 600 eV. The optical property of the synthesized powders were evaluated by using a Hitachi U-4100 spectrophotometer. The final nanopowder production rate was estimated from the weight of the synthesized powder, together with the fraction of nanopowder from the analysis described above.

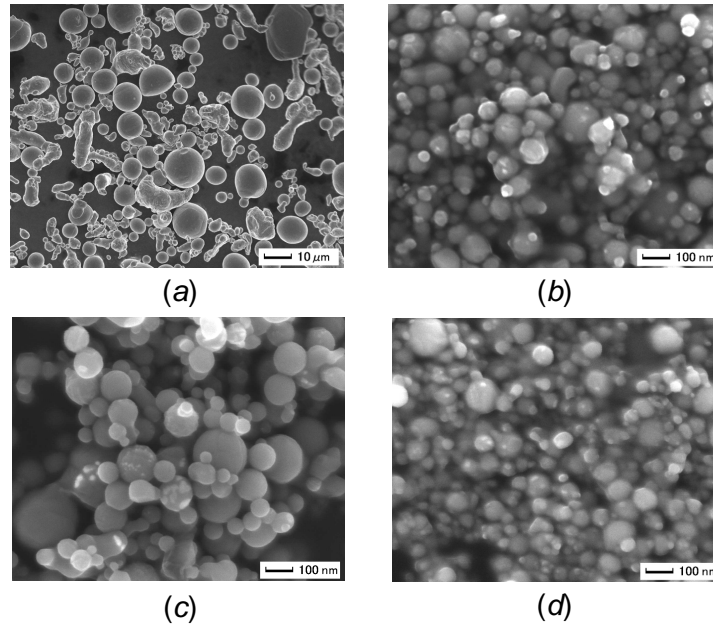


Fig. 2.4: FE-SEM images for (a) feedstock, and synthesized powder with conditions (b) 80%SCL, $g_{\text{pow}} = 12 \text{ g min}^{-1}$, (c) 70%SCL, $g_{\text{pow}} = 12 \text{ g min}^{-1}$, and (d) 60%SCL, $g_{\text{pow}} = 19 \text{ g min}^{-1}$.

2.4 Results and discussions

2.4.1 SEM images and particle size distribution of synthesized powder

Figure 2.4 presents FE-SEM images of feedstock and the synthesized nanopowder collected at the filter in different SCL conditions. The feedstock Ti powder has mean diameter around $27 \mu\text{m}$ with various shapes. However, most of synthesized particles were found to have a size of 100 nm or less in any of the three SCL conditions in the present experiments. Therefore, nanosized particles were produced despite heavy-load feeding of the feedstock using our developed method. The shapes of the synthesized particles were also observed to be almost spherical for these three conditions, which implies that nanoparticles were synthesized and grown in gas phase rather than on the surface of the filter or the wall.

From these FE-SEM images, the particle size distributions were evaluated by measuring diameters of 200 randomly selected particles. Figure 2.5 depicts the size distribution of

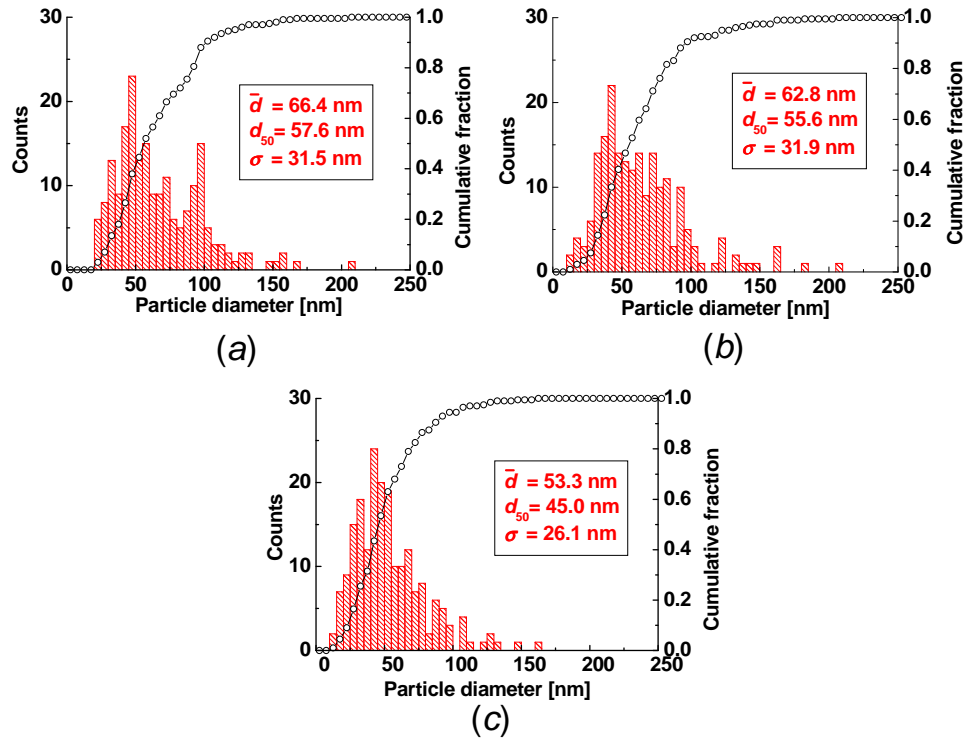


Fig. 2.5: Particle size distributions for (a) 80%SCL, $g_{\text{pow}} = 12 \text{ g min}^{-1}$, (b) 70%SCL, $g_{\text{pow}} = 12 \text{ g min}^{-1}$, and (c) 60%SCL, $g_{\text{pow}} = 19 \text{ g min}^{-1}$.

particles synthesized using the PMITP+TCFF method with three SCL conditions. More than 90% of the synthesized particles are nanoparticles of less than 100 nm diameter for three SCL conditions. The particle mean diameter \bar{d} , median d_{50} , and standard deviation σ for the synthesized nanopowder were calculated from the particle size distribution. The quantities \bar{d} , d_{50} and σ are also presented in figure 2.5. These magnitudes \bar{d} and σ are shown as a function of the SCL in figure 2.6. The \bar{d} refers to the left vertical axis, whereas σ to the right vertical axis in this figure. This figure suggests that lower SCL, which leads a larger modulation degree, provides nanoparticles with smaller \bar{d} . The quantity \bar{d} decreases from 68 nm to 53 nm with reduction of SCL from 80% to 60%. An interesting point is that the \bar{d} for 60%SCL is smaller than those for 70%SCL and 80%SCL, although the condition 60%SCL has a higher feeding rate g_{pow} of 19 g min^{-1} , whereas $g_{\text{pow}} = 12 \text{ g min}^{-1}$ for 80%SCL and 70%SCL. Generally, a higher g_{pow} often leads to a larger \bar{d} of synthesized particles because a higher g_{pow} forms a higher density vapour cloud in the thermal plasma

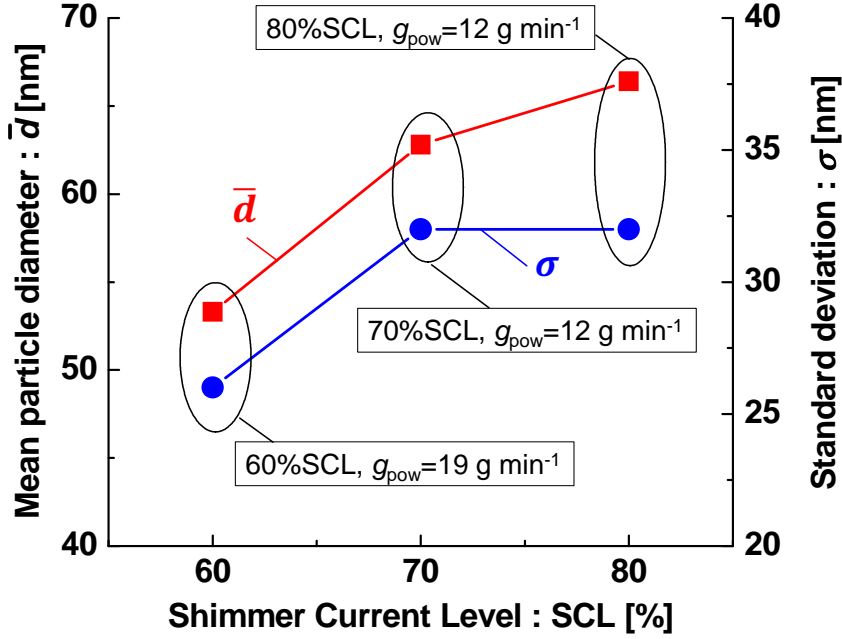


Fig. 2.6: Dependence of particle mean diameter and standard deviation on the shimmer current level of the pulse modulation.

to promote particle growth.

Synthesized particles were also collected in the upstream chamber and the downstream chamber. More than 90% of the synthesized particles collected in the upstream and downstream chamber have diameters less than 100 nm. No unmelted and non-vaporized feedstocks were found for 80% and 70% SCL with $g_{\text{pow}} = 12 \text{ g min}^{-1}$ conditions. This fact demonstrates no micro-sized powder such as unmelted and non-vaporized powder was synthesized for 80% and 70% SCL with $g_{\text{pow}} = 12 \text{ g min}^{-1}$ conditions.

Based on these results and weight measurements of the synthesized powder, the production rates of nanopowder were estimated as more than 400 g h^{-1} under $g_{\text{pow}} = 12 \text{ g min}^{-1}$ condition (80% SCL and 70% SCL), for example, using the 20-kW PMITP. This production rate value is 10–20 times higher than those obtained using the conventional thermal plasma method reported in the literature [5, 14]. This important benefit of our developed method, large-scale synthesis of nanopowder, must be emphasized.

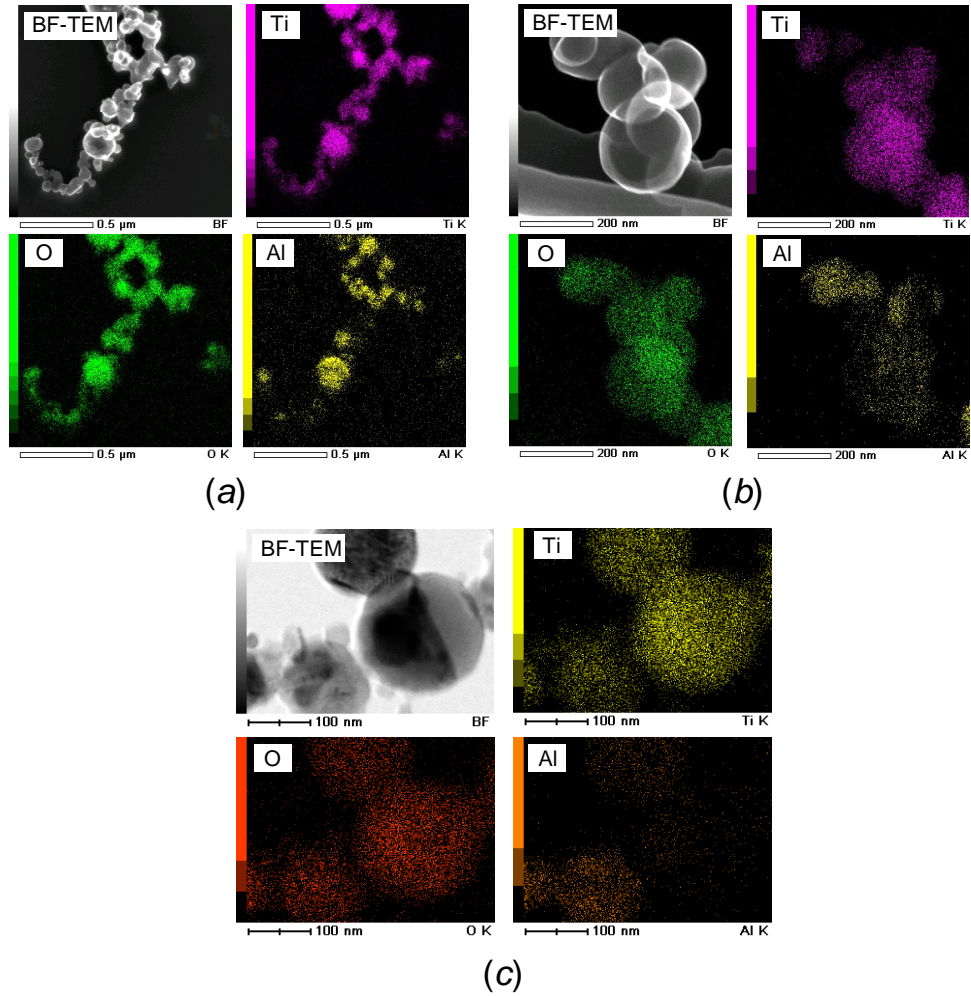


Fig. 2.7: BF-TEM and TEM/EDX mapping for (a) 80%SCL, $g_{\text{pow}} = 12 \text{ g min}^{-1}$, (b) 70%SCL, $g_{\text{pow}} = 12 \text{ g min}^{-1}$, and (c) 60%SCL, $g_{\text{pow}} = 19 \text{ g min}^{-1}$.

2.4.2 Element distribution analysis of synthesized nanoparticles using BF-TEM & TEM/EDX mapping

This study specifically examines the large-scale synthesis of Al^{3+} -doped TiO_2 nanopowder. In this case, Al doping is one vital factor to characterize synthesized nanopowder. Figure 2.7 presents BF-TEM images and TEM/EDX mapping results of synthesized nanopowder collected at the filter. Panel (a) shows the result for condition of 80%SCL with a powder feed range g_{pow} of 12 g min^{-1} , whereas panel (b) shows the result of the condition 70%SCL and $g_{\text{pow}}=12 \text{ g min}^{-1}$. Finally, panel (c) shows the results for the condition 60%SCL and

$g_{\text{pow}}=19 \text{ g min}^{-1}$. Each panel has a BF-TEM image and Ti, O, Al element distributions. Magnifications of TEM images and TEM/EDX mapping are different in each panel. From the BF-TEM images, results show that spherical nanoparticles without mesopores were synthesized for these three SCL conditions. The TEM/EDX mapping shows that an Al element was detectable, and that it was distributed almost uniformly in the synthesized particles in the same manner as Ti and O for 80%SCL and 70%SCL, which means that elemental Al might be distributed almost uniformly on the synthesized TiO₂ nanoparticles even by our developed PMITP+TCFF method with heavy-load feeding of feedstock, together with consideration from the XRD and XPS analysis results as described later.

2.4.3 Crystal composition assessment of synthesized Al³⁺-doped TiO₂ nanopowder using XRD spectra analysis

An X-ray diffraction (XRD) analysis was made to study the crystallographic structure and chemical composition of the synthesized nanoparticles. Figure 2.8 portrays XRD spectra for the synthesized nanopowder collected at the filter. Panel (a) shows the result for the condition of 80%SCL, whereas panel (b) corresponds to the result for 70%SCL, and panel (c) is that for 60%SCL. The designation ‘A’ in these figures indicates that the specified XRD spectral line arises from TiO₂ in anatase form; the designation ‘R’ denotes the lines originating from the TiO₂ in rutile form. Panel (d) shows reference XRD peaks for feedstock and synthesized crystal materials: Ti, Al, Al₂O₃ and TiO₂ in rutile and anatase phases.

From these figures, the synthesized nanopowder was confirmed clearly as containing mainly rutile and anatase-TiO₂ crystal for three SCL conditions. The weight fraction f_A of anatase-TiO₂ in the synthesized nanopowder can be estimated from

$$f_A = \frac{1}{1 + 1.26 \frac{I_{R(110)}}{I_{A(101)}}}, \quad (2.1)$$

where $I_{R(110)}$ represents the intensity of the (110) reflection of rutile at $2\theta=27.4^\circ$, and $I_{A(101)}$ stands for the intensity of the (101) reflection of anatase at $2\theta=25.3^\circ$. Here, f_A were estimated as about 40 wt% for the 80%SCL condition, 35 wt% for the 70%SCL condition and 40 wt% for the 60%SCL condition. These values of f_A are lower for the

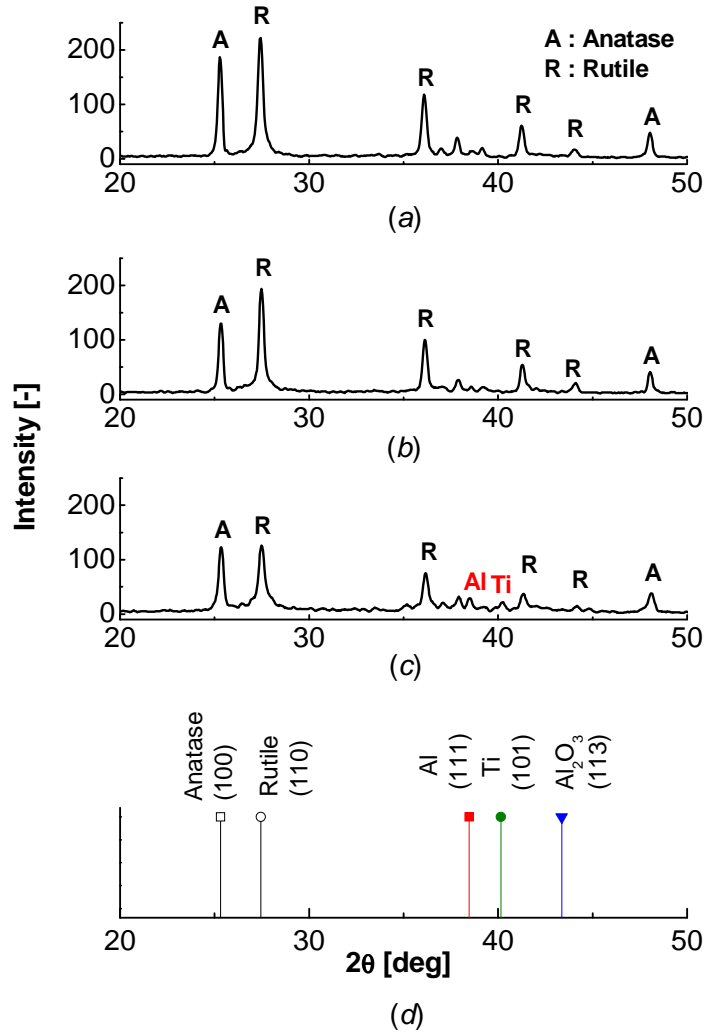


Fig. 2.8: XRD spectra for (a) 80%SCL, $g_{pow} = 12 \text{ g min}^{-1}$, (b) 70%SCL, $g_{pow} = 12 \text{ g min}^{-1}$, (c) 60%SCL, $g_{pow} = 19 \text{ g min}^{-1}$, and (d) reference peaks.

photocatalyst [25]. The lower f_A and lower photocatalysis characteristics are useful for application to skin care cream [7]. The f_A in the synthesized nanopowder can be controlled by changing the O_2 concentration in nanopowder processing [3, 26]. The most important feature to be emphasized in the obtained XRD spectra is that no Ti, Al or Al_2O_3 peaks were detected in nanopowder for 80%SCL and 70%SCL. This result shows that Ti, Al and Al_2O_3 bulk particles in feedstock were evaporated completely in the high-temperature region of the PMITP, and that Ti was oxidized completely in a highly reactive field to generate TiO_2 crystal. In addition to these XRD spectra, Al or Al_2O_3 crystal rarely exists in the synthesized particles according to EDX mapping results described in the previous section. This result suggests that Al elements might be doped in TiO_2 nanopowder synthesized

using our developed PMITP+TCFF method. However, Al and Ti peaks were detected in the case of 60%SCL and $g_{\text{pow}} = 19 \text{ g min}^{-1}$. This might be the result of heavy-load feeding. Therefore, the remaining Al and Ti are present in the synthesized nanopowder.

2.4.4 Chemical binding state in synthesized Al³⁺-doped TiO₂ nanopowder by XPS spectra analysis

The X-ray photo-electron spectroscopy (XPS) was used to measure the elemental composition, chemical state and electronic state of the elements on the surface of the synthesized nanoparticles. Figure 2.9 (a) portrays the XPS analysis result for Ti 2p region between 455 eV and 470 eV for the synthesized Al³⁺-doped TiO₂ nanopowder. For comparison, the result for commercial pure-TiO₂ nanopowder (P-25; Degussa) and the result for non-doped pure TiO₂ nanopowder synthesized using our PMITP+TCFF method are presented in figure 2.9. The non-doped pure TiO₂ nanopowder was synthesized in almost identical conditions with 80%SCL-80%DF and $g_{\text{pow}}=12 \text{ g min}^{-1}$, except for raw material without Al powder. The neutralizer was also used to prevent nanoparticles from charging up during the XPS measurement.

This figure shows Ti 2p_{3/2} and Ti 2p_{1/2} peaks for analysis. The commercial pure TiO₂ and pure TiO₂ nanopowder synthesized using the PMITP+TCFF method has almost the same binding energy of 459.30–459.60 eV for Ti 2p_{3/2}, and 465.00 eV for Ti 2p_{1/2}. These correspond to the binding energy for electrons from the 2p orbit in Ti (IV) in TiO₂. However, the chemical shifts clearly occurred for Ti 2p_{1/2} and Ti 2p_{3/2} peaks by the intended addition of Al elements. For example, this chemical shift is clearly visible from 459.30 eV to 459.60 eV for Ti 2p_{3/2} peak in case of Al addition under the condition of 80%SCL and $g_{\text{pow}}=12 \text{ g min}^{-1}$. This chemical shift is increased further from 459.60 eV to 460.20 eV with reduction of SCL from 80% to 70%, i.e. a larger modulation in the PMITP. These results imply that the Al element was possibly doped in TiO₂. A higher amount of Al doping might be obtained for reduced SCL. However, the chemical shift to lower binding energy occurred for Ti 2p_{3/2} to 457.80 eV in the condition of 60%SCL and $g_{\text{pow}}=19 \text{ g min}^{-1}$, which might be true because of oxygen deficiency attributable to rich Ti vapour arising from a higher g_{pow} . That oxygen deficiency produces Ti₂O₃ crystals in 60%SCL and $g_{\text{pow}}=19 \text{ g min}^{-1}$

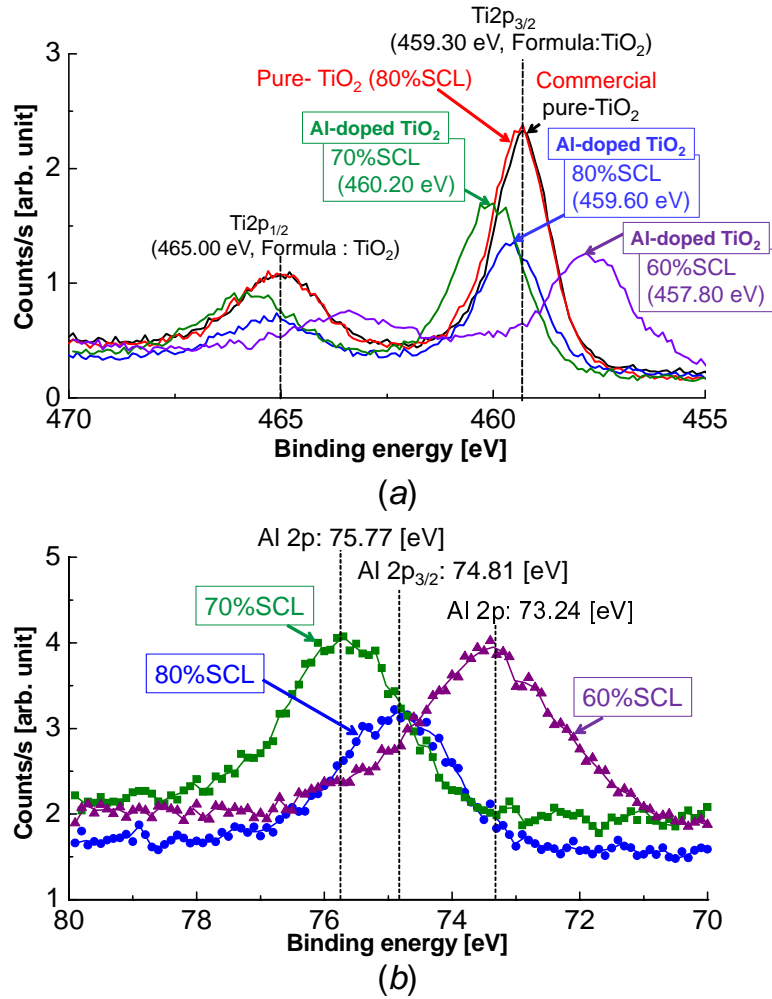


Fig. 2.9: XPS spectra for commercial pure-TiO₂ (P-25; Degussa), pure-TiO₂ nanopowder synthesized using PMITP+TCFF and Al³⁺-doped TiO₂ nanopowder synthesized in this study. (a) Ti 2p region between 455 eV and 470 eV, (b) Al 2p region between 70 eV and 80 eV.

condition. Figure 2.9 (b) portrays the XPS analysis result for Al 2p region between 70 eV and 80 eV for the synthesized Al-doped TiO₂ nanopowder. The binding energies around 74.81 eV (condition of 80%SCL), 75.77 eV (condition of 70%SCL) and 73.24 eV (condition of 60%SCL) correspond to Al 2p of Al³⁺, Al 2p_{2/3} of Al³⁺ and Al 2p of Al³⁺, respectively. They probably indicate that Al³⁺ ion exist in TiO₂ crystal and possible formation of the Al-O-Ti chemical bond in the TiO₂ lattice. In addition, they may indicate that Al³⁺-doped TiO₂ nanopowder was positively charged due to Al³⁺ ion doping [27]. Actually, the Al³⁺-doped TiO₂ nanoparticles could be dispersed in the purified water, while TiO₂ nanoparticles were settled down.

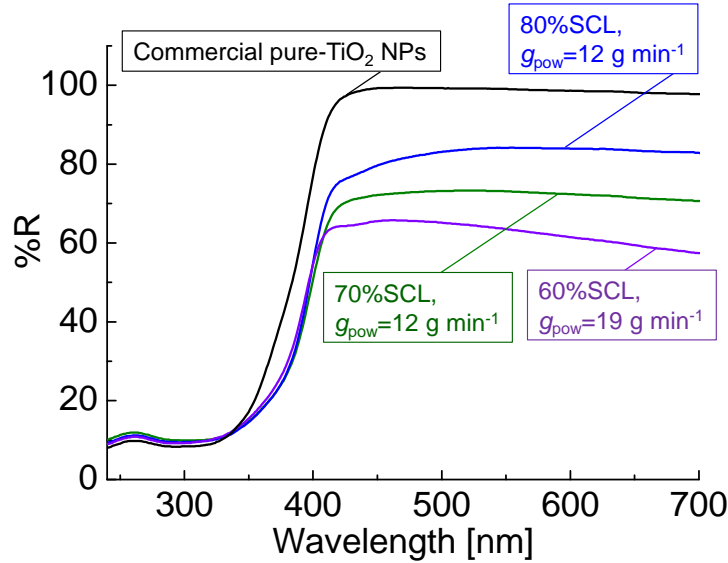


Fig. 2.10: Diffuse reflection spectra for commercial pure-TiO₂ (P-25; Degussa) and Al³⁺-doped TiO₂ nanopowder synthesized in this study.

2.4.5 Optical property of synthesized Al³⁺-doped TiO₂ nanopowder by spectrophotometric analysis

The metal-ion doping generally changes the optical property of nanopowders. Influence of Al³⁺ doping to TiO₂ nanopowder was evaluated for the optical property of the synthesized nanopowder by a spectrophotometer for solid powder. Figure 2.10 shows the integrated total diffuse reflectivity %R for Al³⁺-doped TiO₂ synthesized using the PMITP+TCFF method, and then also that for commercial pure-TiO₂ nanopowder for comparison. The %R was obtained using an integrated sphere in the spectrophotometer. As shown in this figure, the commercial pure TiO₂ nanopowder has high reflectivity in the visible-light region because of the wide energy band gap of pure-TiO₂ with 80% anatase-TiO₂ and 20% rutile-TiO₂. It has an absorption edge at a wavelength around 390 nm that corresponds to energy band gap of around 3.18 eV. The synthesized Al³⁺-doped TiO₂ nanopowder also has extremely low diffuse reflectivity %R as much as commercial pure-TiO₂ nanopowder in ultraviolet region, and has lower reflectivity than commercial pure-TiO₂ nanopowder in the visible-light region. For the synthesized Al³⁺-doped TiO₂ nanopowder, the diffuse reflectivity %R in the visible-light region decreases with reduced SCL from 80% to 60%. The important point in the diffuse reflectivity is that synthesized nanopowder has an absorption

edge at a wavelength around 400 nm. This wavelength of the absorption edge corresponds to an energy gap of 3.10 eV. On the other hand, %R for Al³⁺-doped TiO₂ nanopowder in the visible-light region decreases with reduced SCL from 80% to 60%. This reason was considered that Al concentration in the vicinity of TiO₂ nanoparticle surface was probably changed depending on the SCL value [28]. This result suggests that Al doping to TiO₂ crystal can be done in the synthesized nanopowder using our PMITP+TCFF method. It is noteworthy that the production rate of Al³⁺-doped TiO₂ nanopowder was estimated as 400 g h⁻¹.

2.5 Summary of chapter 2

Large amounts of Al³⁺-doped TiO₂ nanopowder were synthesized using pulse-modulated induction thermal plasmas (PMITP) with time-controlled feeding of feedstock (TCFF). The PMITP+TCFF method originally developed in our group, is characterized by the intermittent powder feeding synchronized with the modulated power of the PMITP. Effects of the coil current modulation degree were also studied for the synthesized Al³⁺-doped TiO₂ nanopowder. Results show that most of the synthesized powder had diameter of less than 100 nm. The diameter can be decreased by setting a reduced shimmer current level of the PMITP. The synthesized nanopowder was analyzed using several different methods including EDX, XRD, XPS, and spectrophotometry. Results showed that Al elements can be doped on TiO₂ nanopowder synthesized using the PMITP+TCFF method. The final production rate was estimated as higher than 400 g h⁻¹.

References

- [1] Malato S, Blanco J, Alarcon D C, Maldonado M I, Fernandez-Ibanez P and Gernjak W 2007 Photocatalytic decontamination and disinfection of water with solar collectors. *Catalysis Today* **122** pp.137–49
- [2] Li J, Zhao X, Wei H, Gu Z Z, and Lu Z 2008 Macroporous ordered titanium dioxide (TiO₂) inverse opal as a new label-free immunosensor. *Analytica Chimica Acta* **625** pp.63–9
- [3] Gratzel M 2001 Photoelectrochemical cells. *Nature* **414** pp.338–44
- [4] Biju K P and Jain M K 2008 Effect of crystallization on humidity sensing properties of sol-gel derived nanocrystalline TiO₂ thin films. *Thin Solid Films* **516** pp.2175–80
- [5] Park J H, Park O O, and Kim S 2006 Photoelectrochemical water splitting at titanium dioxide nanotubes coated with tungsten trioxide. *Appl. Phys. Lett.* **89** 163106
- [6] Tsai Y C, Hsi C H, Bai H, Fan S K and Sun D H 2012 Single-step synthesis of Al-doped TiO₂ nanoparticles using non-transferred thermal plasma torch. *Jpn. J. Appl. Phys.* **51** 01AL01
- [7] Shon K H, Cho L D, Na H S, Kim B J, Park J H and Kim H J 2009 Development of a novel method to prepared Fe- and Al-doped TiO₂ from wastewater. *J. Ind. Eng. Chem.* **15** pp.476–82
- [8] Barolo G, Livraghi S, Chiesa M, Cristina M, Paganini C and Giamello E 2012 Mechanism of the photoactivity under visible light of N-doped titanium dioxide. charge carriers migration in irradiated N-TiO₂ investigated by electron paramagnetic resonance. *J. Phys. Chem. C* **116** pp.20887–94

-
- [9] Lee K N, Kim Y, Lee C W and Jai-Sung Lee J S 2011 Simultaneous amination of TiO₂ nanoparticles in the gas phase synthesis for bio-medical applications *Mater. Sci. Eng.* **18** 082021
- [10] Mio M, Kogoma M, Fukui H, and Takeda A 2010 Control of inflammation using adsorption of inflammatory by nano-particles *Chem. Eng.* **55** pp.603-8 (in Japanese)
- [11] Girshick S L, Chiu C P, Muno R, Wu C Y, Yang L, Singh S K, and McMurry P H 1993 Thermal plasma synthesis of ultrafine iron particles. *J. Aerosol Sci.* **24** pp.367–82
- [12] Shigeta M, Watanabe T, and Nishiyama H 2004 Numerical investigation for nano-particle synthesis in an RF inductively coupled plasma. *Thin Solid Films* **457** pp.192–200
- [13] Oh S M and Ishigaki T 2004 Preparation of pure rutile and anatase TiO₂ nanopowders using RF thermal plasma. *Thin Solid Films* **457** pp.186–91
- [14] Lee J E, Oh S M, and Park D W 2004 Synthesis of nano-sized Al doped TiO₂ powders using thermal plasma. *Thin Solid Films* **457** pp.230–4
- [15] Ishigaki T, Oh S M, Li J G, and Park D W 2005 Controlling the synthesis of TaC nanopowders by injecting liquid precursor into RF induction plasma. *Sci. & Technol. Advanced Mater.* **6** pp.111–8
- [16] Tong L and Reddy R G 2006 Thermal plasma synthesis of SiC nano-powders/nano-fibers. *Materials Research Bulletin* **41** pp.2303–10
- [17] Ishigaki T and Li J G 2007 Synthesis of functional nanocrystallites through reactive thermal plasma processing. *Sci. & Technol. Advanced Mater.* **8** pp.617–23
- [18] Li J G, Ikeda M, Ye R, Moriyoshi Y, and Ishigaki T 2007 Control of particle size and phase formation of TiO₂ nanoparticles synthesized in RF induction plasma. *J. Phys. D: Appl. Phys.* **40** pp.2348–53
- [19] Tanaka Y, Nagumo T, Sakai H, Uesugi Y, and Nakamura K 2010 Nanoparticle synthesis using high-powered pulse-modulated induction thermal plasma. *J. Phys. D: Appl. Phys.* **43** 265201

-
- [20] Tanaka Y, Sakai H, Tsuke T, Uesugi Y, Sakai Y, and Nakamura K 2011 Influence of coil current modulation on TiO₂ nanoparticle synthesis using pulse-modulated induction thermal plasmas. *Thin Solid Films* **519** pp.7100–05
- [21] Tanaka Y, Tsuke T, Guo W, Uesugi Y, Ishijima T, Watanabe S, and Nakamura K 2012 A large amount synthesis of nanopowder using modulated induction thermal plasmas synchronized with intermittent feeding of raw materials. *J. Phys. D: Conf. Ser.* **406** 012001
- [22] Tanaka Y, Sakai H, Tsuke T, Guo W, Uesugi Y, Sakai Y and Nakamura K 2011 Nanoparticle synthesis using high-power modulated induction thermal plasmas with intermittent synchronized feeding of raw materials. *Proc. 20th Int. Symp. Plasma Chem. ISPC-20*, 346, Philadelphia, USA
- [23] Tanaka Y and Sakuta T 2003 Temperature control of Ar induction thermal plasma with diatomic molecular gases by pulse-amplitude modulation of coil current. *Plasma Sources Sci. & Technol.* **12** pp.69–77
- [24] Tanaka Y, Uesugi Y, and Sakuta T 2007 Controlling the number of excited atoms flowing into the reaction chamber using pulse-modulated induction thermal plasmas at atmospheric pressure. *Plasma Sources Sci. & Technol.* **16** pp.281–9
- [25] Ohno T, Sarukawa K, Tokieda K, and Matsumura M 2001 Morphology of a TiO₂ photocatalyst (degssa, P-25) consisting of anatase and rutile crystalline phases. *J. of Catal.* **203** pp.82–6
- [26] Tanaka Y, Guo W, Kodama N, Uesugi Y, Sakai Y and Nakamura K 2013 A novel approach for large amount synthesis of TiO₂ nanopowder using modulated induction thermal plasmas with time-controlled feeding of feedstock. *Proc. 21th Int. Symp. Plasma Chem. ISPC-21*, OR **52**, Cairns, Australia
- [27] Abazović N D, Mirengi L, Janković I A, Bibić N, Šojić D V, Abramović B F and Čomor M I 2009 Synthesis and characterization of rutile TiO₂ nanopowders doped with iron ions. *Nanoscale Res. Lett.* **4** pp.518–25

- [28] Trejo-Tzab R, Alvarado-Gil J J, Quintana P, Bartolo-Pérez P 2012 N-doped TiO₂ P25/Cu powder obtained using nitrogen(N₂) gas plasma. *Catal. Today* **193** pp.179–85

Chapter 3

Fundamental behavior of Ti and TiO vapor in the induction thermal plasma

3.1 Introduction

Nanoparticles or nanopowder (NPs) are anticipated as promising next-generation materials because of their unique physical, chemical, and optical characteristics. It is therefore used in various fields of environmental, energy, electronics and so on. For example, titanium dioxide nanopowder (TiO₂ NPs) is used widely in many applications such as photocatalysts [1], photonic crystals [2], photovoltaic cells [3], and gas sensors [4]. Metallic-ion doped TiO₂ NPs are anticipated for use as visible light-active photocatalysts [5]– [7], and as biomedical materials for adsorption of inflammatory protein [8, 9]. For these biomedical nanomaterials, almost a complete lack of contamination is required because even slight impurities of countable atoms or molecules can change the NP properties. Therefore, non-contamination processes (high-purity process) of nanomaterials with high production efficiency are desired for development for nano-technological progress.

Various nanopowder synthesis methods have been invented to date [11]. In these methods, different types of thermal plasmas have been adopted to fabricate nano-materials including NPs [1]. Among the various methods, the thermal plasma method, especially the inductively coupled thermal plasma (ICTP) method presents some beneficial features for NP production [2]– [18]. The most important point of this method is that the ICTP fundamentally provides no contamination processes. Another advantageous point of this

ICTP method is that it can offer one-step and direct process with much shorter processing time. In addition, this ICTP method can readily produce not only pure-metal NPs but also oxide NPs and nitride NPs by adopting specified reactive gas in the processing. However, this method also entails some shortcomings. Control of synthesized NP size and enhanced production efficiency are challenging issues for the ICTP method.

In the chapter 2, a unique and original method of large-scale NPs synthesis method was discussed. For large-scale NPs synthesis, the pulse-modulated induction thermal plasma (PMITP) was applied with the time-controlled feedstock feeding (TCFF) method, i. e., PMITP+TCFF method [19]– [22]. The PMITP was developed in our laboratory to control the temperature and the reactive species in thermal plasmas using amplitude modulation of the coil-current [23,24]. The PMITP can uniquely produce a periodically changed temperature field: a higher temperature field during higher coil-current phase and a lower temperature field during lower coil-current phase. In addition to this, we further developed the TCFF method for more effective nanopowder synthesis. The TCFF method makes the feedstock inject intermittently and synchronously into the PMITP using coil-current modulation [21,22]. In this method, large amounts of feedstock are injected into the higher temperature plasma in the torch only during higher coil-current phase, and injection of feedstock was stopped during lower coil-current phase. This PMITP+TCFF method can provide efficient evaporation of the feedstock and efficient nucleation of nanoparticles. The PMITP+TCFF method can also produce size-controlled nanopowder with a high production rate. In the chapter 2, PMITP+TCFF method was adopted for large-scale synthesis of Al^{3+} -doped TiO_2 nanopowder [26]. In this work, we successfully obtained Al^{3+} -doped TiO_2 nanopowder with a high production rate of $\sim 400 \text{ g h}^{-1}$ with mean diameter of $\sim 67 \text{ nm}$ at the input power of 20 kW. Besides Al^{3+} -doped TiO_2 nanopowder, we found that pure- TiO_2 nanopowder can be synthesized with a high production rate of $\sim 500 \text{ g h}^{-1}$ with a mean diameter of $\sim 43 \text{ nm}$ by using PMITP+TCFF method [7, 21]. These production rates were several tens of times higher than those of conventional thermal plasma methods. The conversion rate from injected feedstock to collected nanopowder was estimated as about 34-42% in case of TiO_2 nanopowder production [7, 21].

A key point to enhancing the production efficiency is to understand NP formation mechanisms in the PMITP or ICTP torch. We have been investigating that mechanism mainly

using a two-dimensional optical emission spectroscopy (2D OES) system during TiO₂ NP synthesis.

This chapter describes fundamental investigation results of Ti feedstock evaporation and precursor formation processes in the non-modulated ICTP torch with an almost single-shot injection of feedstock. This almost single-shot injection of feedstock to the ICTP was selected to elucidate the evaporation process of Ti feedstock and the fundamental formation of TiO molecules. For this purpose, 2D OES measurements were conducted during TiO₂ nanopowder synthesis. In addition, changes in transport properties and the temperature distribution in the torch were calculated numerically to support observation results presented in the discussion section. Finally, the Ti feedstock evaporation, transport, and diffusion of Ti atoms and formation and conveyance of precursor TiO species in the plasma torch were discussed based on the observation and numerical calculation results. Through these results, this paper contributes to the elucidation of fundamental behaviour of feedstock evaporation and formation of precursor molecules during TiO₂ NPs synthesis.

3.2 Principle of two-dimensional optical emission spectroscopy system

This section describes the principle of 2D OES system used in our experiments. Figure 3.1 shows schematic diagram of the 2D OES system. This OES system consists of an imaging spectrometer, an objective lens and a collimator lens in front of the spectrometer, and a high speed video camera behind the spectrometer. This type of the imaging spectroscopic system is often called “Monochromatic imaging spectrometer (MIS)” [25, 26]. The MIS is based on the idea using a Czerny-Turner spectrometer. The Czerny-Turner spectrometer has an entrance slit, a spherical mirror (a), a diffraction grating, a spherical mirror (b), and an exit slit. Using this spectrometer, a 2D monochromatic image can be obtained as follows:

1. A image from a light source is captured by an objective lens.
2. This image through the objective lens is collimated by a collimator lens (a) located in front of the entrance slit of the spectrometer. Then, a part of the collimated light

t

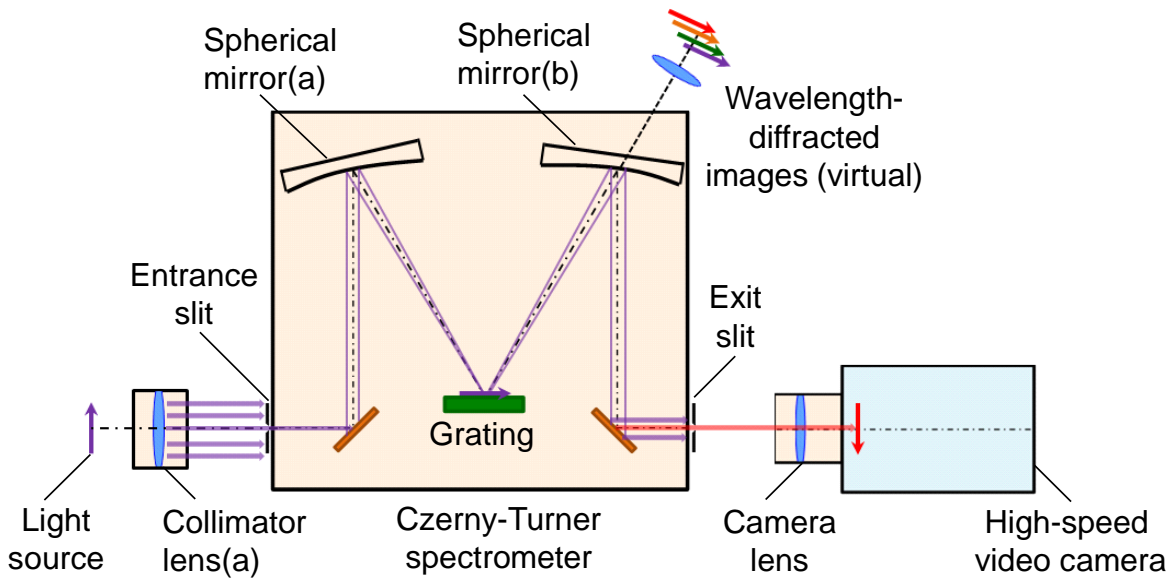


Fig. 3.1: The principle of 2D OES system.

is fed into the spectrometer through the slit.

3. From the light fed from the entrance slit, the image is reformed on the focal plane in vicinity of the diffraction grating by the spherical mirror (a), because the distance between the entrance slit and the grating is equal to the focal distance of the spherical mirror (a). Then, this focal image is dispersed in different wavelengths by the diffraction grating.
4. The dispersed image is re-collimated by the spherical mirror (b).
5. The re-collimated light at a specified wavelength can pass through the exit slit. This re-collimated monochromatic light contains information on the 2D image.
6. If a camera lens is located outside of the exit slit, a monochromatic 2D image at the specified wavelength can be obtained on the focal plane of the camera lens. Thus, a 2D monochromatic image can be captured by an 2D imaging sensor placed on the focal plane.

In this system, the entrance slit works only as an aperture of the spectrometer. The wavelength resolution is determined by width of the exit slit and the type of the diffraction

grating adopted. Main advantages of this 2D OES system are a high wavelength resolution ($\sim 0.2\text{--}0.8$ nm), and setting observation wavelength variable, rather than the conventional band-pass interference filters. In general, band-pass interference filters have been often used for 2D OES with a high-speed video camera or an ICCD. However, the wavelength resolution of the filter is low like as few nm to few tens nm, and we cannot change the observation wavelength of the filter; another filter for another wavelength should be prepared. In contrast, the 2D OES system based on MIS has a high wavelength resolution, and freedom degree for observation wavelength. Meanwhile, this system loses much of light from the light source at the entrance slit of the spectrometer. Nevertheless, this light loss is not a serious problem in the present observation because a thermal plasma of interest has an extremely high radiation intensity. Thus, the 2D OES system based on MIS is greatly useful for investigation of thermal plasma processing.

3.3 Experimentals

The experimental setup is the same as that reported from our previous work [26]. Details can be found in an earlier report [26]. Figure 3.2 presents the plasma torch for TiO_2 nanopowder synthesis. The plasma torch has two coaxial quartz tubes. The interior quartz tube has 70 mm inner diameter and 370 mm length. Around the quartz tube is an eight-turn induction coil connected to the matching circuit and an inverter power supply to generate an electromagnetic field and then an rf thermal plasma inside the plasma torch. Into this plasma torch, a water-cooled stainless steel tube is inserted from the top of the torch head. Through this tube, feedstock powder can be supplied to the thermal plasma inside the plasma torch from the powder feeder. Between this tube and the powder feeder, a high-speed solenoid valve is connected to start and stop the feedstock feeding. This valve can be controlled using a transistor–transistor logic (TTL) signal to open and close. Downstream of this plasma torch, reaction chambers and a collection filter are installed to collect the synthesized nanopowder as described in an report [26].

Table 4.1 summarizes the experimental conditions of TiO_2 nanopowder synthesis in the present work. The time-averaged input power from the inverter power supply was fixed at 20 kW. The fundamental frequency of the coil-current was 450 kHz. For this experiment,

t

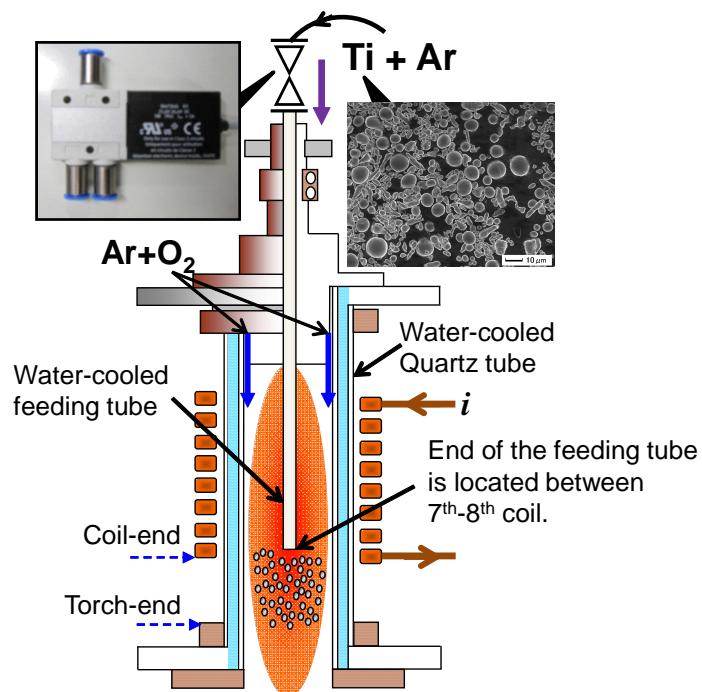


Fig. 3.2: Experimental configuration using ICTP and solenoid valve installed to control feedstock injection.

non-modulated ICTP was adopted to investigate the fundamental processes of Ti feedstock evaporation and formation of precursor species. The Ar-O₂ mixture gas was used as the sheath gas. Its total flow rate was fixed at 100 L min⁻¹. The O₂ gas admixture ratio was set to 10 mol%. The quenching gas was not injected in this study because the evaporation process of almost single-shot feedstock is studied fundamentally in this study. The pressure in the reaction chamber was fixed at 300 Torr (~40 kPa). Pure-Ti powder (TILOP-45; Osaka Titanium Technologies Co., Ltd.) was used as feedstock. The mean diameter and the maximum diameter of this powder are, respectively, about 27 μm and 45 μm. The feedstock was injected intermittently into the ICTP torch with Ar carrier gas. The Ar carrier gas flow rate was fixed at 4 L min⁻¹. The intermittent injection of the feedstock was conducted using the high-speed solenoid valve shown in figure 3.2. The response time of this valve (t_{res}) was about 2 ms. The feedstock feed rate was adjusted to about 4–7 g min⁻¹. This feeding rate is much lower than that used for the large-scale nanopowder synthesis condition [26]. This low feed rate was selected because of fundamental investigation of feedstock evaporation and precursor formation processes. The cycle time including open/close of the high-speed solenoid valve was fixed at 30 ms, which is much longer than that used in our previous work [26] to realize an almost single-shot of the feedstock. The open (t_{open})/close time (t_{close}) of the solenoid valve was regulated, respectively, at 8/22 ms (27%DF_{valve}), 12/18 ms (40%DF_{valve}), and 16/14 ms (53%DF_{valve}). In a condition of 27%DF_{valve}, the open time was less than that in other conditions. This condition corresponds to an almost single-shot feeding of feedstock, which can avoid interaction between each single powder feeding during intermittent feeding. We set different valve opening times to confirm the valve performance and response, and to study Ti atom transport in the ICTP.

3.3.1 Spectroscopic observation conditions

Two-dimensional optical emission spectroscopic measurements were conducted using a 2D OES system (AN-IMC-DD; Anfi Inc.) presented in figure 3.3. This observation system contains an objective lens (AF Zoom-Nikkor 80-200 mm f/2.8D ED; Nikon Corp.), a beam splitter, two imaging spectrometers (Acton Spectra Pro 2300i; Princeton Instruments, Inc.), and two high-speed video cameras (GX-8; nac Imaging Technology Inc.). The observation conditions are presented in table 3.2. The two-dimensional observation region was set to

Table 3.1: Experimental conditions.

Time-averaged input power	20 kW
Fundamental frequency of the coil current	450 kHz
Modulation	Non-modulation
Pressure	300 Torr (~ 40 kPa)
Gas composition	Ar: 90 L min ⁻¹ , O ₂ : 10 L min ⁻¹
Carrier gas flow rate	Ar: 4 L min ⁻¹
Quenching gas	Non-injection
Valve-open/close cycle	30 ms
Valve-open/close time	8/22 ms(27%DF _{valve}), 12/18 ms(40%DF _{valve}) 16/14 ms(53%DF _{valve})
Powder feed rate g_{pow}	4-7 g min ⁻¹
Feedstock	100wt%Ti powder $\bar{d} = 27 \mu\text{m}$, $d < 45 \mu\text{m}$

about $57 \times 47 \text{ mm}^2$ region below the coil-end. The emission light from the observation region was transmitted through an objective lens. Then it was separated into two optical paths using the beam splitter. The two splitter lights were inputted simultaneously to the two imaging spectrometers. Each monochromated image at a specified wavelength from each spectrometer was observed using a high-speed video camera. The upper observation system was defined as System A (Sys.A). The lower one was defined as System B (Sys.B) as presented in figure 3.3. These imaging spectrometers contain diffraction grating of 1200 grooves/mm. The wavelength resolutions of each two observation system were, respectively, 0.8 nm for Sys.A and 0.4 nm for Sys.B. A salient feature of this observation system is that it can measure two-dimensional radiation intensities for two wavelengths simultaneously. In this work, the atomic spectral line of Ti I at a wavelength of 453.32 nm was observed using Sys.B, whereas the band head of TiO molecular spectra at a wavelength of 621 nm was detected using Sys.A. These two spectral intensities were measured simultaneously in two dimensions.

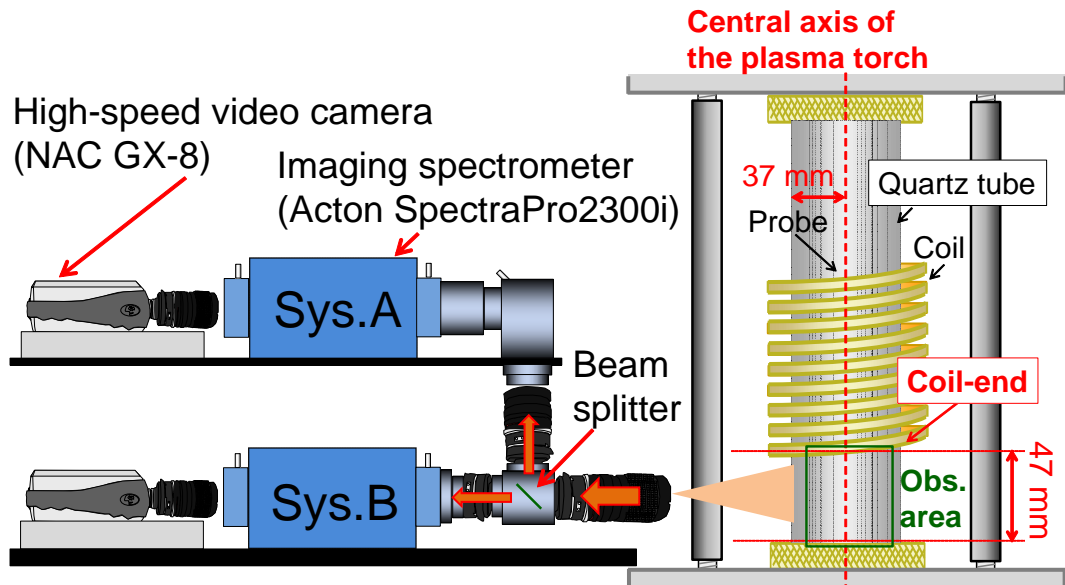


Fig. 3.3: Two-dimensional spectroscopic observation region and observation system using imaging spectrometer and high-speed video camera.

3.4 Two-dimensional spectroscopic observation results

3.4.1 Test spectroscopic observation for simultaneous observation

First, the radiation intensity distribution from the same spectral lines were observed simultaneously both by Sys.A and Sys.B observation systems to confirm and compare the operation and sensitivity of both Sys.A and Sys.B.

Figure 3.4(a) presents test results of Ti I spectral intensity distribution at a wavelength of 453.32 nm. The coil-end and the torch-end positions are shown as white solid curves. These time evolutions in the radiation intensity distribution were detected simultaneously by Sys.A and Sys.B. The Ti feedstock powder was fed continuously to the thermal plasma at an input power of 20 kW without coil current modulation. These observation results suggest clearly that both Sys.A and Sys.B showed almost identical images, which means that Sys.A and Sys.B can detect the same region at the same wavelength specified. It is also noteworthy that the strength of the radiation intensities detected by Sys.A were lower than that by Sys.B. This is true because differences in optical path length and sensitivity of imaging

Table 3.2: Two-dimensional spectroscopic observation conditions.

Observation area	57×47 mm ² region below the coil end
Diffraction grating	1200 grooves/mm
Wavelength resolution	0.8 nm (Sys.A), 0.4 nm (Sys.B)
Spectral lines observed	Ti I (453.32 nm) and TiO (621 nm)
Frame rate for high speed video camera	3000 fps

sensors between these two observation systems of Sys.A and Sys.B. These differences in sensitivity can be calibrated using these images at the same wavelength. Figure 3.4(b) presents TiO spectral intensity distribution at 621.0 nm wavelength, as measured by Sys.A and Sys.B. The results showed that Sys.A and Sys.B can yield almost identical images at the specified wavelength of 621.0 nm, and the image at 621.0 nm differs greatly from Ti I at 453.32 nm. The results above imply that Sys.A and Sys.B is useful to measure two-dimensional radiation intensity and its time variation at two wavelengths simultaneously.

3.5 Results and discussions

3.5.1 Spatial and temporal variation of Ti I radiation intensities

Figure 3.5 shows observation results for Ti I atomic lines at 453.32 nm by Sys.B. Panel (a) shows 27%DF_{valve}($t_{\text{open}}=8$ ms), panel (b) shows 40%DF_{valve}($t_{\text{open}}=12$ ms), and panel (c) shows 53%DF_{valve}($t_{\text{open}}=16$ ms). The coil-end and the torch-end positions are presented as white solid curves. The Ti I radiation intensity depends on the excited Ti atomic density and the Ti excitation temperature $T_{\text{ex}}^{\text{Ti}}$. The solenoid valve received the open-signal (high level) at $t=0$ ms for all conditions, and received the close-signal (low level) at $t=8$ ms for panel (a) 27%DF_{valve}, $t=12$ ms for panel (b) 40%DF_{valve} and $t=16$ ms for panel (c) 53%DF_{valve}, where t is the time. In each panel, the open/close signal for the valve is shown schematically versus time t . The condition for panel (a) corresponds to the almost single-shot condition for feedstock feeding.

In case of the 27%DF_{valve} in panel (a), the Ti I radiation intensity was extremely low

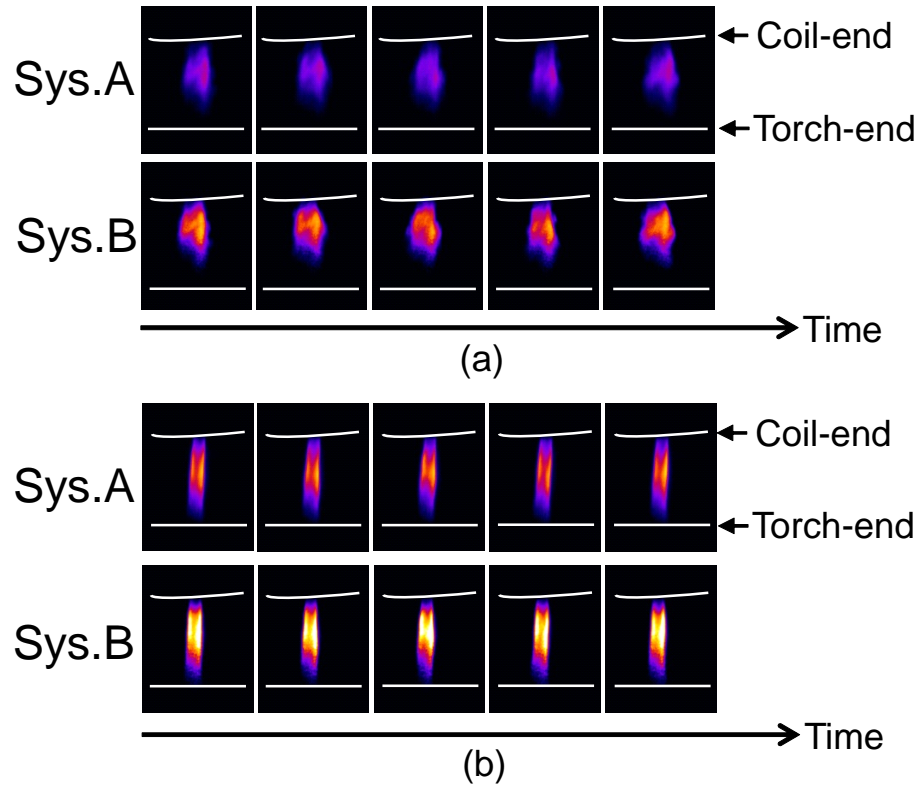


Fig. 3.4: Test observation result. (a) Ti I radiation intensities observed simultaneously. (b) TiO radiation intensities observed simultaneously.

between $t=0$ ms to 6 ms. This is true because Ti feed stock powder was not yet supplied. However, the Ti I radiation intensity was markedly increased from $t=8$ ms. Therefore, it takes about 8 ms to transport feedstock powder from the valve to the thermal plasma. The feedstock powder is evaporated by the thermal plasma to produce detectable excited Ti atoms. Furthermore, this Ti I radiation intensity was detected as high even just below the coil-end region in the plasma torch. This fact signifies that the feedstock is evaporated rapidly just into the thermal plasma from the tip of the water-cooled tube. In addition, this high radiation intensity was observed not only in the on-axis region but also in the off-axis region, although the Ti feedstock was supplied along the axis from the water-cooled tube located on the axis of the plasma torch. This fact indicates that some Ti feedstock is supplied not only in the on-axis region but also in the off-axis region, and that the excited Ti atom emitting radiation might be transported in a radial direction. Furthermore, in the on-axis region, the strength of radiation intensity was found to be weaker than that of the

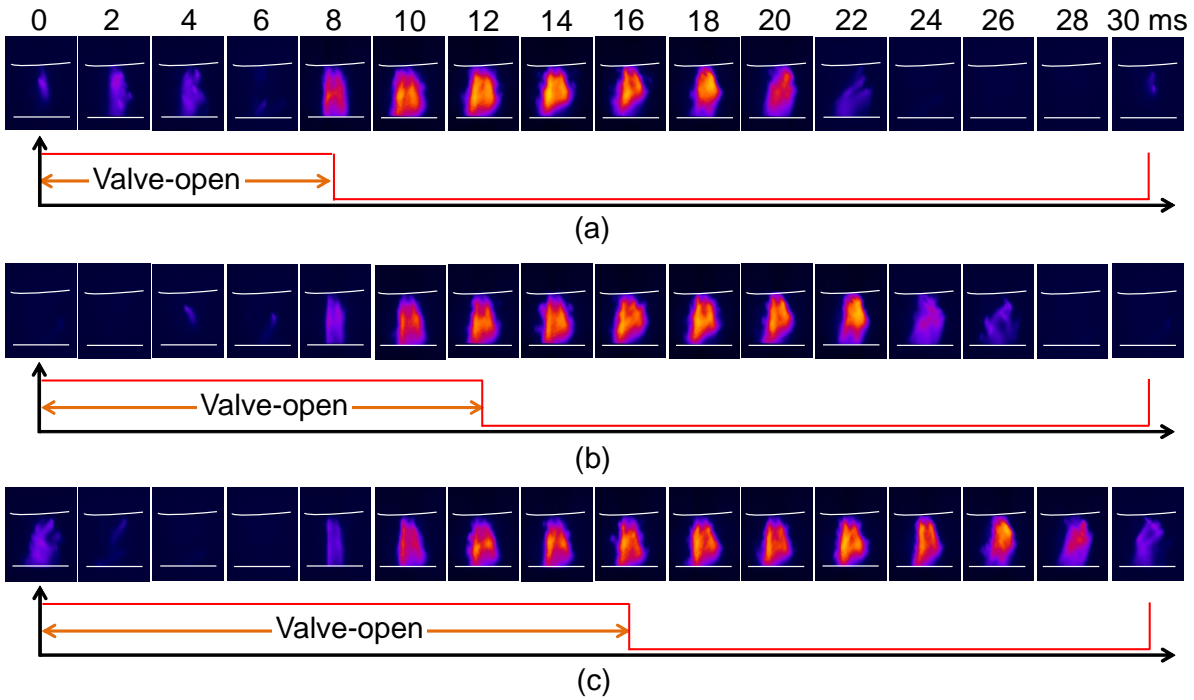


Fig. 3.5: Two-dimensional spectroscopic observation result during TiO_2 nanopowder synthesis using non-modulated ICTP torch with intermittent feedstock feeding. Two-dimensional distribution of Ti I radiation intensities for (a) $27\%DF_{\text{valve}}$ (open/close=8/22 ms), (b) $40\%DF_{\text{valve}}$ (open/close=12/18 ms), and (c) $53\%DF_{\text{valve}}$ (open/close=16/14 ms)

off-axis region. Then, the Ti I spectral line maintained high radiation intensity between $t=8$ ms to 20 ms. This time duration corresponds to the total time for actual powder feeding by the opening valve. It also corresponds to evaporation of the feedstock and decay in the evaporated Ti atoms. After $t=22$ ms, the Ti I radiation intensity decreased with time, eventually reaching a low value. Details of the Ti atom behaviour above will be discussed in section 3.6.4.

For other longer opening time conditions $40\%DF_{\text{valve}}$ and $53\%DF_{\text{valve}}$, the Ti I radiation intensity increases at almost identical timing $t=8$ ms to that in the $27\%DF_{\text{valve}}$ condition, which suggests that almost identical starting timing of feedstock feeding were obtainable using valve opening in our system. When the opening time duration increases, the high Ti I radiation intensity phases were measured between $t=8$ ms to 26 ms for $40\%DF_{\text{valve}}$, and

$t=8$ ms to 30 ms for $54\%DF_{\text{valve}}$. This time duration increase corresponds to the increase in the length of the valve open time. This result implies that detected Ti I radiation intensity reflects the behaviour of the evaporated and excited Ti atoms, and that Ti I detectable time-lengths, which are the actual feeding time duration, are controllable in detail by the valve opening time length. This ability to control feedstock feeding is extremely important for our developed PMITP+TCFF method.

3.5.2 Spatial and temporal variation of TiO molecular spectra

The TiO molecules are regarded as one precursor to TiO_2 NPs. It is therefore important to study at which timing and where TiO molecules form, and how TiO molecules transport is in the ICTP. Figure 3.6 depicts the temporal variation in the radiation intensity of the band head of TiO molecular spectra at 621 nm. Panel (a) shows the result for $27\%DF_{\text{valve}}$ (valve-open:8 ms). Panels (b) and (c) respectively present $40\%DF_{\text{valve}}$ (valve-open:12 ms), and $53\%DF_{\text{valve}}$ (valve-open:16 ms).

For $27\%DF_{\text{valve}}$, TiO radiation intensity was too low to be detected at $t=0$ ms to $t=6$ ms. However, the TiO radiation intensity was increased remarkably from $t=8$ ms even still inside the plasma torch which is located downstream of the reaction chamber. This timing of $t=8$ ms is almost identical to the timing of an increase in Ti I radiation intensity indicated in figure 3.5(a). This fact signifies that TiO is generated at similar timing immediately after Ti evaporation in 1 ms time resolution. At this timing $t=8$ ms, the TiO radiation intensity became high at 30 mm distance from the coil end on the axis. This high TiO radiation intensity region was stretched axially from that position to upper position around 10 mm below the coil end between $t=8$ ms and $t=16$ ms, which suggests that TiO is formed first downstream from the coil end, and that the TiO formation region is then expanded upstream. In addition, TiO molecules are more formed around the on-axis region, which differs greatly from the behaviour of excited Ti atoms. The TiO radiation intensity decreased from $t=18$ ms from upstream. After $t=20$ ms, the TiO radiation intensity became sufficiently low to be undetectable.

A similar tendency can also be found in cases of $40\%DF_{\text{valve}}$ and $54\%DF_{\text{valve}}$. Only the differences are time duration with high TiO intensity, depending on the open time of the valve. Strong TiO radiation intensity was found to continue between $t=8$ ms and 22 ms for

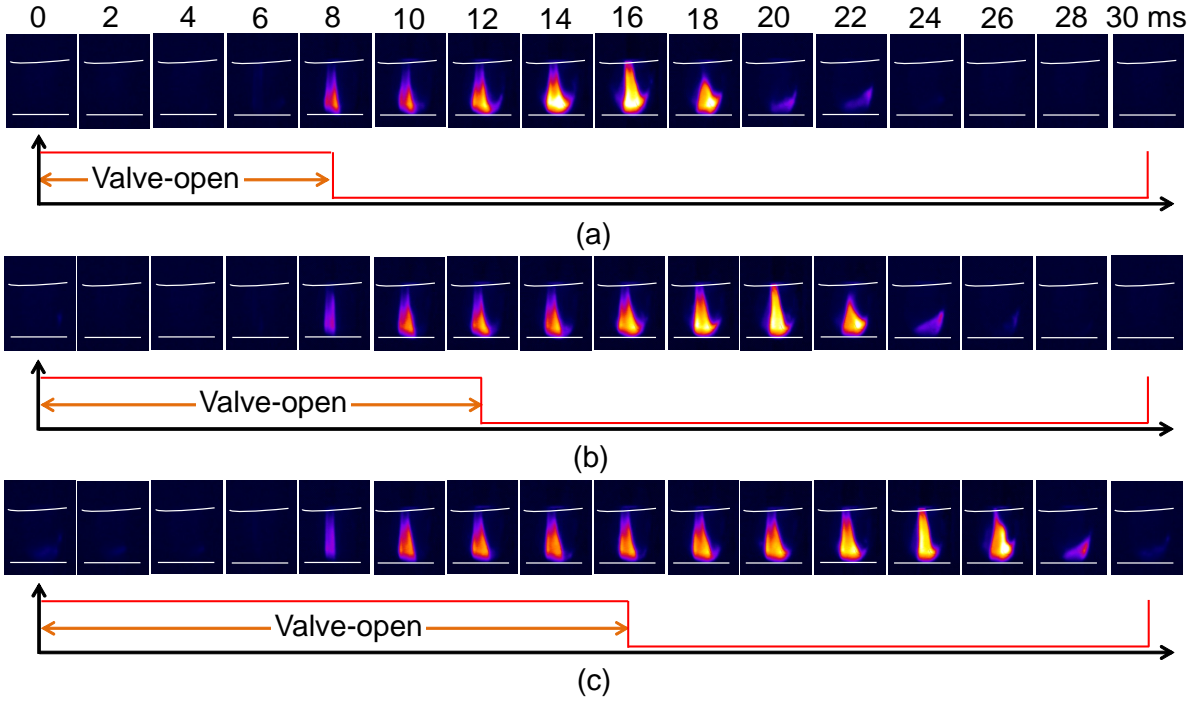


Fig. 3.6: Two-dimensional spectroscopic observation result during TiO_2 nanopowder synthesis using non-modulated ICTP torch with intermittent feedstock feeding. Two-dimensional distribution of TiO radiation intensities for (a) $27\%DF_{\text{valve}}$ (open/close=8/22 ms), (b) $40\%DF_{\text{valve}}$ (open/close=12/18 ms), and (c) $53\%DF_{\text{valve}}$ (open/close=16/14 ms)

$40\%DF_{\text{valve}}$, and between $t=8$ ms and 26 ms for $54\%DF_{\text{valve}}$. These TiO detectable time-lengths were ~ 10 ms for $27\%DF_{\text{valve}}$, ~ 14 ms for $40\%DF_{\text{valve}}$, and ~ 18 ms for $54\%DF_{\text{valve}}$. These detectable time lengths correspond to the total time of the valve open time and the response time of the valve ($t_{\text{open}} + t_{\text{res}}$).

The results above all suggest that gas phase TiO was formed in the limited area around on-axis region in the torch. Then TiO gas was transported to the axial direction by gas flow. Further details of TiO behaviour will be discussed in section 3.6.4.

3.6 Discussion

3.6.1 Equilibrium particle composition for Ar-O-Ti system

To consider Ti and TiO behaviours, it is important to understand dominant species fundamentally at a given temperature and pressure. The equilibrium compositions of Ar-O-Ti system in the gas phase were therefore calculated using minimization of Gibb's free energy. Considering the isothermal and isobaric process, Gibb's free energy is shown as follows:

$$G = \sum_{i=1}^N x_i \left\{ \mu_i^0 + RT \ln \left(\frac{x_i}{\sum_{j=1}^N x_j} \right) + RT \ln \left(\frac{P}{P_0} \right) \right\} \quad (3.1)$$

$$\mu_i^0 = -RT \ln (Z_i^{\text{tr}}) - RT \ln (Z_i^{\text{int}}) + U_i^0 \quad (3.2)$$

$$Z_i^{\text{tr}} = \frac{RT}{P_0} \left(\frac{2\pi m_i kT}{h^2} \right)^{\frac{3}{2}} \quad (3.3)$$

where G stands for the Gibb's free energy, x_i is the mole number of i -species, N signifies the total number in the mixture gas, T denotes the temperature, P represents the pressure, R is the gas constant, μ_i^0 is the chemical potential, Z_i^{tr} signifies the translational partition function, Z_i^{int} denotes the internal partition function, P_0 is the atmospheric pressure, U_i^0 stands for the standard enthalpy of formation, m_i represents the mass of i -species, k is Boltzmann's constant, and h is Planck's constant. Each physical constant was referred to reference data [30].

The calculated equilibrium composition of 89%Ar-10%O₂-1%Ti system in gas phase at 300 Torr (~ 40 kPa) is presented for temperatures of 3000–15 000 K in figure 3.7. In this calculation, we only show mole fraction of each of species in gas phase, not in liquid and solid phases. This is because low Ti vapor contamination of 1 mol% involves low partial pressures of Ti, TiO, and TiO₂ in gas phase, which hardly results in these species in liquid and solid phases. Almost all particles are ionized in the temperatures of more than 15 000 K region. From 15 000 to 10 000 K, atomic species of Ar and O are formed from their ions. At temperatures of 10 000 to 4000 K, neutral atoms of Ar, O and Ti are dominant. The neutral Ti atoms are formed by recombination of Ti⁺ and electron from 8000 to 4000 K. Between the temperature of 6000 to 3000 K, TiO(g) in gas phase is formed

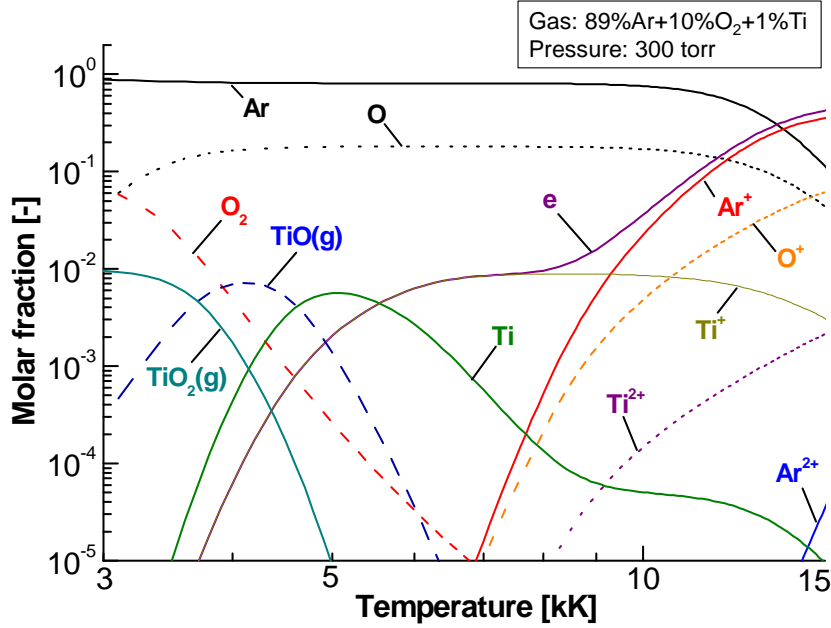


Fig. 3.7: Equilibrium particle composition for the Ar-O-Ti system.

attributable to association reaction of $\text{Ti}(\text{g}) + \text{O}$ atom with an exothermic reaction energy of $663.2 \pm 8.4 \text{ kJ mol}^{-1}$ [30]. At temperatures of 5000–4000 K, $\text{TiO}(\text{g})$ becomes dominant for Ti included species. The interesting point in this composition is that both particles of $\text{Ti}(\text{g})$ and $\text{TiO}(\text{g})$ can exist with high molar fraction between temperatures about 5000 to 4000 K. Therefore, association reaction of $\text{Ti}(\text{g}) + \text{O} \rightarrow \text{TiO}(\text{g})$ and dissociation reaction of $\text{TiO}(\text{g}) \rightarrow \text{Ti}(\text{g}) + \text{O}$ are popular in this temperature region. A further decrease in temperature produce $\text{TiO}_2(\text{g})$ from association reaction of $\text{TiO}(\text{g}) + \text{O} \rightarrow \text{TiO}_2(\text{g})$ with an exothermic reaction energy of $1266.9 \pm 12.6 \text{ kJ mol}^{-1}$ [30].

As already shown in figure 3.5 and figure 3.6, both Ti I and TiO radiation were observed with high intensities around the on-axis region. In contrast, only Ti I radiation intensity was detected in the off-axis region. These characteristic distributions of Ti I and TiO suggest that TiO molecules were dissociated in the off-axis region with high temperatures of more than 6000 K. The ICTP has higher temperature in the off-axis region because of zero input power on the axis. However, TiO molecular gas was formed only in the on-axis region, which implies that the on-axis region has a mild temperature of 4000–5000 K, which is lower than that in off-axis region. The reason will be again discussed in section 3.6.2 and section 3.6.3.

3.6.2 Effect on plasma properties by Ti vapour inclusion into Ar-O₂ plasmas

This section presents a description of the effect of Ti vapour inclusion into Ar-O₂ thermal plasmas on the transport properties. This effect is treated here because Ti feedstock injection supplies high concentrated Ti vapour to the thermal plasma, which might affect the input power density distribution and then the temperature distribution. We calculated the transport properties for 100%Ar, 90%Ar+10%O₂, 89%Ar+10%O₂+1%Ti and 100%Ti at a pressure of 300 Torr. The thermal conductivity κ and the electrical conductivity σ were calculated using the first-order approximation of the Chapman–Enskog method [28, 31] as follows:

Electrical conductivity:

$$\sigma = \frac{e^2}{kT} \cdot \frac{x_e}{\sum_{\substack{i=1 \\ i \neq e}}^N x_i \Delta_{ei}^{(1)}} \quad (3.4)$$

$$\Delta_{ij}^{(1)} = \frac{8}{3} \left(\frac{2m_i m_j}{\pi k T (m_i + m_j)} \right)^{\frac{1}{2}} \pi \bar{\Omega}_{ij}^{(1,1)} \quad (3.5)$$

where e stands for the elementary charge of electron, x_i signifies molar fraction of species i , and $\pi \bar{\Omega}_{ij}^{(1,1)}$ denotes the momentum transfer collision integral between species i and j .

Thermal conductivity κ :

$$\kappa = \kappa_{\text{tr}} + \kappa_{\text{int}} + \kappa_{\text{re}} \quad (3.6)$$

$$\kappa_{\text{tr}} = \frac{15}{4} k \sum_{i=1}^N \frac{x_i}{\sum_{j=1}^N \alpha_{ij} x_j \Delta_{ij}^{(2)}} \quad (3.7)$$

$$\kappa_{\text{int}} = k \sum_{i=1}^N \frac{\left(\frac{C_{P_i} m_i}{R} - \frac{5}{2} \right) x_i}{\sum_{j=1}^N x_j \Delta_{ij}^{(1)}} \quad (3.8)$$

$$\kappa_{re} = k \sum_{l=1}^{N_{re}} \frac{\left(\frac{\Delta H_l}{RT}\right)^2}{\sum_{i=1}^N \frac{\beta_{li}}{x_i} \left(\sum_{j=1}^N (\beta_{li}x_j - \beta_{lj}x_i)\Delta_{ij}^{(1)}\right)} \quad (3.9)$$

$$\alpha_{ij} = 1 + \frac{\left(1 - \frac{m_i}{m_j}\right) \left(0.45 - 2.54 \frac{m_i}{m_j}\right)}{\left(1 + \frac{m_i}{m_j}\right)^2} \quad (3.10)$$

$$\Delta H_l = \sum_{i=1}^N \beta_{li} h_i m_i \quad (3.11)$$

$$\Delta_{ij}^{(2)} = \frac{16}{5} \left(\frac{2m_i m_j}{\pi k T (m_i + m_j)}\right)^{\frac{1}{2}} \pi \overline{\Omega}_{ij}^{(2,2)} \quad (3.12)$$

where κ_{tr} signifies the translational thermal conductivity, κ_{int} denotes the internal thermal conductivity, κ_{re} represents the reactional thermal conductivity, C_{P_i} represents the specific heat of species i , β_i is the stoichiometric coefficient, h_i is the enthalpy of species i , and $\pi \overline{\Omega}_{ij}^{(2,2)}$ is the viscosity collision integral between species i and j .

These collision integrals were calculated as below. Collision integrals between neutral-neutral atoms were calculated using the interparticle potentials [33,34]. Collision integrals between the same molecules were estimated using the hard-sphere model. Atomic radii used on calculation of the hard-sphere model were referred from literatures [35,36]. Collision integrals between different kinds of neutral species were found by the empirical combining law [37]. In case of collision between heterogeneous ion-neutral particles, momentum transfer collision integrals were calculated using resonant charge exchange cross section [38]. On the other hands, viscosity collision integrals were assumed to be equal to those of the neutral species. For electron-neutral particle, only e-O and e-Ar collision integrals were calculated from the collision cross section and other combinations were estimated using the hard-sphere model. Collision integrals for coulomb collisions were calculated by Gvosdover cross section for coulomb collisions [39].

Figure 3.8 presents the calculated thermal conductivity for 100%Ar, 90%Ar+10%O₂, 89%Ar+10%O₂+1%Ti and 100%Ti at a pressure of 40 kPa as a function of temperature. This figure shows that the thermal conductivity was increased slightly in case of

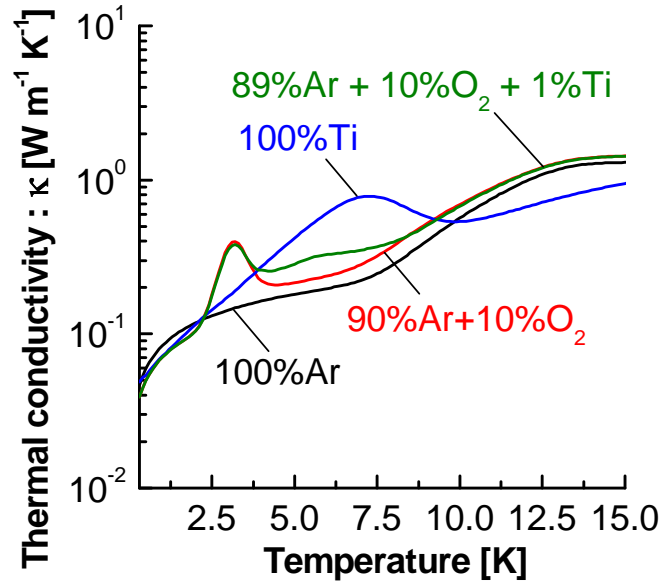


Fig. 3.8: Thermal conductivity of various gas composition conditions.

1%Ti vapour inclusion to the Ar-O₂ gas in temperature range from 3000 to 7500 K. This phenomenon results from reactional thermal conductivity of Ti ionization. Nevertheless, inclusion of 1%Ti vapor to the Ar-O₂ does not influence greatly the total thermal conductivity. Thus, influence of Ti inclusion to the Ar-O₂ mixture from thermal conductivity needs not discussed in later section 3.6.4.

Figure 3.9 shows the calculated electrical conductivity for 100%Ar, 90%Ar+10%O₂, 89%Ar+10%O₂+1%Ti and 100%Ti. As shown in figure 3.9, the electrical conductivity for 100%Ar and 90%Ar-10%O₂ gas is very low at temperatures below 5000 K. In contrast, only 1%Ti inclusion to Ar-O₂ gas markedly elevates the electrical conductivity at temperatures below 7500 K. This calculation result suggests that the electric current can flow in high electrical conductivity region. Then Joule heating can be enhanced in the region including Ti vapour. This fact shows that inclusion of Ti vapour elevates joule heating, affecting the evaporation of Ti feedstock. It is, however, noted that Ti vapour inclusion elevates the radiation loss at the same time. This effect thus limits the excessive temperature increase.

Actually, as shown in figure 3.5, the Ti I radiation intensity was observed more strongly at the off-axis region than in the on-axis region. This high Ti I intensity at off-axis region might be attributable to the Joule heating enhancement above.

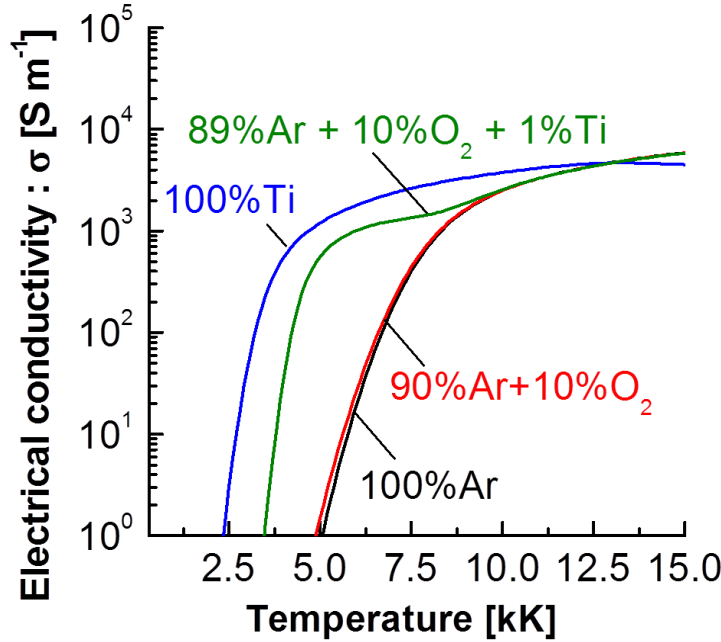


Fig. 3.9: Electrical conductivity of various gas composition conditions.

3.6.3 Effect of carrier gas injection to the temperature field

In this section, the influence of Ar carrier gas injection to the temperature field was investigated from the numerical calculation of the temperature field in the plasma torch. In this calculation, the following are assumed in the Ar-O₂ ICTP: (a) Plasma is in a steady state. (b) Local thermodynamic equilibrium (LTE) condition was assumed. (c) Consequently, the electron temperature, the gas temperature and the excitation temperatures are all equal. All chemical reactions reach their equilibrium states. (d) Plasma is optically thin. Consequently, the light absorption effect is negligible. (e) The gas flow is laminar. Therefore, turbulence is not considered. (f) Plasma has an axisymmetric structure. Following the assumption described above, we solved the governing equations including the mass conservation, the momentum conservation, the energy conservation, the mass conservation for O₂, and the Maxwell equations. The calculation conditions were similar with those of the experiment. In this calculation, for simplicity, the Ti feedstock injection was not considered. The carrier gas flow rate was set at 0 and 4 L min⁻¹. The temperature of feeding tube wall was fixed at 300 K. The heat transfer between feeding tube wall and the plasma was taken into account. The SIMPLE method was adopted to solve the governing equations [40].

Figure 3.10 shows the numerical calculation results on the temperature distribution. Panel (a) shows the result without carrier gas, whereas panel (b) gives the result with Ar carrier gas injection of 4 L min^{-1} . The tip of the water-cooled feeding tube is located between 7th–8th turn of the coil. From panel (a), the temperature below the tip of feeding tube region ($z=200\text{--}250 \text{ mm}$) changes between about 2000 to 9000 K in case of no carrier gas injection. However, the temperature in this region ($z=200\text{--}250 \text{ mm}$) varies from 2000 K to 5000 K when Ar carrier gas is injected as shown in panel (b).

The axial velocity in the feeding tube was calculated as about 11 m s^{-1} . It is considered from this gas velocity and the response time of the high speed valve that the Ar carrier gas starts being injected into the ICTP torch at $t \sim 6 \text{ ms}$ in figures 3.5 and 3.6. This timing is earlier than the timing of Ti I intensity observed in figure 3.5. Therefore, Ar carrier gas is injected firstly into the ICTP torch before Ti feedstock injection into the torch and then the temperature below the tip of feeding tube is decreased and changed between about 2000 K–5000 K.

The melting point and evaporation temperature of solid Ti are, respectively, 1953 K and 3535 K [37]. According to these data, the temperature of 2000–5000 K below the feeding tube with Ar carrier gas is sufficiently high for melting and evaporation of Ti feedstock. In addition, these temperatures of 2000–5000 K can promote to form precursor TiO molecules according to the calculated particle composition shown in figure 3.7. This fact involves that Ar carrier gas injection of 4 L min^{-1} gives rather good influence on the formation of precursor TiO molecules in the plasma torch.

3.6.4 Ti feedstock evaporation and precursor formation in the ICTP torch

This section presents a discussion of Ti feedstock evaporation and formation of precursor TiO molecule process. The two-dimensional spectroscopic observation results and the numerical calculation results presented in the preceding sections engender the following physical picture including generation of Ti atoms, transport of Ti atoms, formation of TiO, and transport of TiO.

Figure 3.11(a) again shows the observation result of Ti I intensity variation for a valve

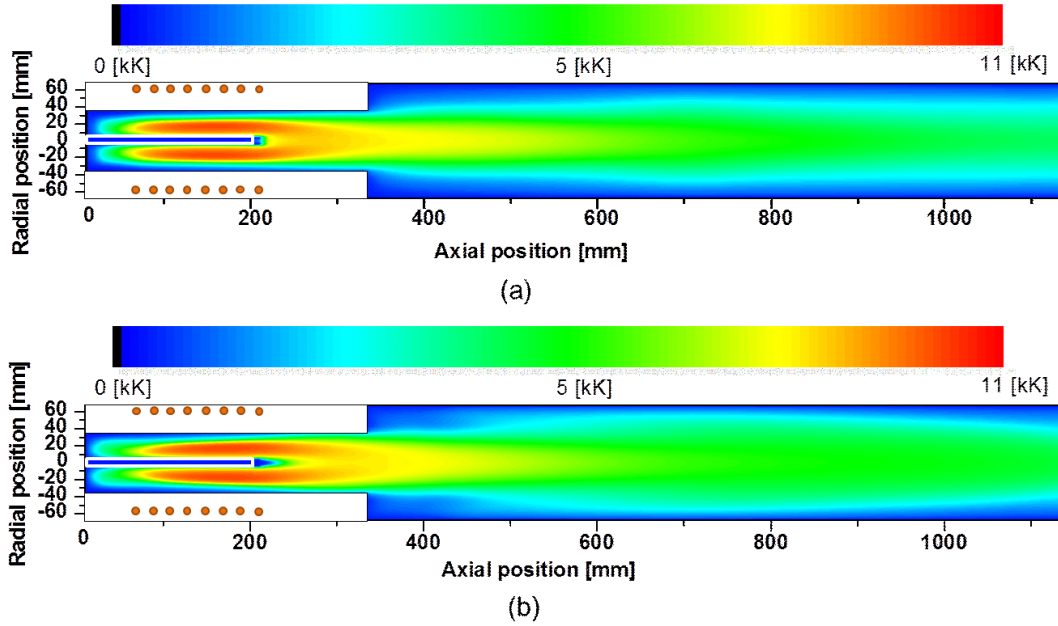


Fig. 3.10: Temperature distribution in the torch and reaction chamber. (a) No carrier gas injection, and (b) 4 L min^{-1} Ar carrier gas injection.

opening time t_{open} of 8 ms, figure 3.11(b) is the observation result of TiO intensity variation for t_{open} of 8 ms. These were observed simultaneously using the two-dimensional spectroscopic imaging system. On the other hand, figures 3.11(c)– 3.11 (e) respectively show our estimated time chart showing Ti feedstock injection into the torch, the temperature variation in the torch, and the temporal variation in formation of precursor TiO molecules. In addition, figure 3.12 shows the physical picture with comments we inferred for the temporal and spatial distribution of Ti atomic density and TiO molecular density in the case of $20\%DF_{\text{valve}}$. This figure was created by superimposing the measured radiation intensity distributions of Ti and TiO shown in figure 3.5 and figure 3.6. In this figure, the green region suggests the distribution of dense Ti atom; the red region shows the distribution of dense TiO molecule. Figure 3.12(a) is the inferred temperature distribution before injection of Ti feedstock into the torch. Figure 3.12(b) shows the introduction of Ti feedstock to the torch, Ti evaporation and initiation of TiO formation at $t \sim 7$ ms. Figure 3.12(c) depicts the mixing of Ti and O atoms and formation of TiO at $t \sim 14$ ms. Figure 3.12(d) shows the transport of TiO to the downstream of the torch at $t \sim 18$ ms. Figure 3.12(e) is a decrease in TiO density and an increase in Ti atomic density attributable to dissociation

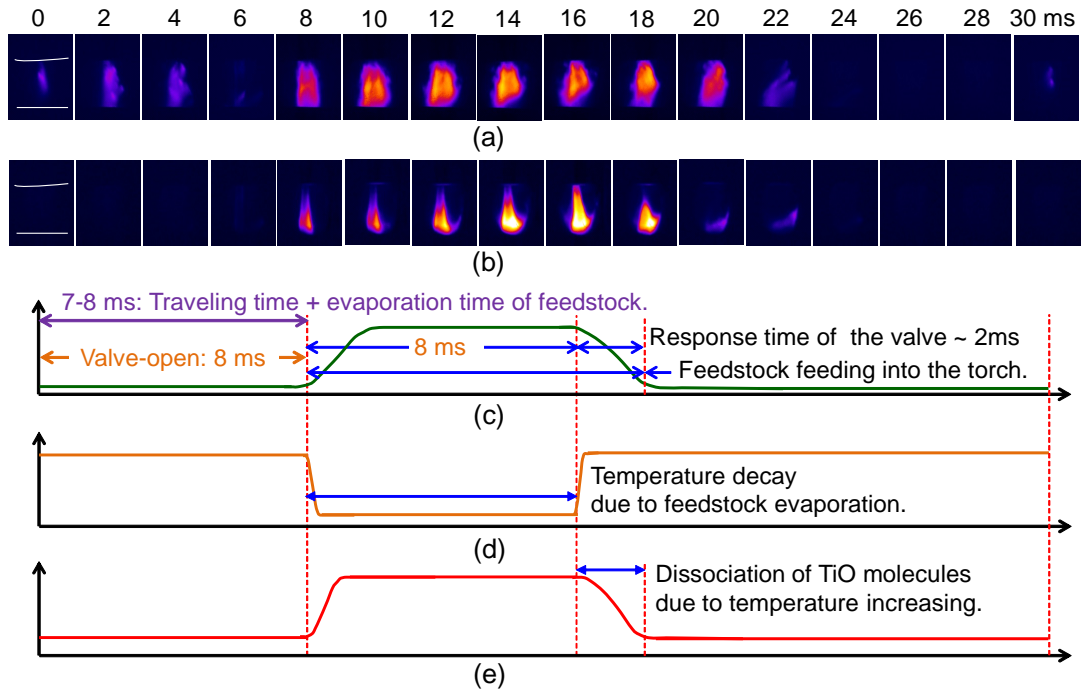


Fig. 3.11: Understanding of Ti feedstock evaporation and precursor TiO molecules in the torch. (a) Observation result for Ti I in valve open condition of 8 ms, (b) Observation result for TiO in valve open condition of 8 ms, (c) Estimated timing of feedstock injection into the torch, (d) Estimated temporal variation of temperature, and (e) Estimated timing of formation of precursor TiO molecules,

reaction of $\text{TiO} \rightarrow \text{Ti} + \text{O}$ by temperature recovery at $t \sim 20$ ms. Figure 3.12(f) is a decrease in Ti density attributable to convective transport to the downstream of the torch at $t \sim 22$ ms.

First, we specifically examine the Ti evaporation phase. The feedstock feeding starts by opening the valve. The feedstock powder from the valve arrives at the tip of the water-cooled tube into the thermal plasma within 7–8 ms, as indicated in figure 3.11(c) and figure 3.12(b). Injected feedstock powder begins to evaporate very quickly in 0.5 ms to generate Ti atoms just under the outlet of the feeding tube because of high temperature of the ICTP around 5000 K. The feedstock evaporation offers dense Ti atoms. The generated Ti atoms are transported to the axial direction downstream by flow of the carrier gas. The Ti atoms are also diffused in the radial direction because of high gradient in Ti

atomic density formed by feedstock evaporation. At the same time, the on-axis temperature could be decreased rapidly to 2000–5000 K by cool carrier gas flow according to the calculated temperature field in figure 3.10, and also by the feedstock evaporation shown in figure 3.12(b). Therefore, we estimated the time variation in the temperature just under the tube as indicated in figure 3.11(d). Because of this temperature decrease to 2000–5000 K, Ti and O are associated to produce precursor TiO molecules around the on-axis region according to the calculated equilibrium composition shown in figure 3.7. This formation reaction occurs almost as soon as Ti feedstock evaporation within 0.5 ms. Therefore, high-density Ti atomic gas is present rather in the off-axis region, although high-density TiO molecular gas is present around on-axis region.

Next, the steady state during Ti feedstock feeding is addressed. Actually, Ti feedstock feeding produces high-density Ti atoms. Increasing Ti atomic density between $t=8$ – 10 ms promotes TiO molecules formation reaction, resulting in the high-density TiO molecules at $t=8$ – 10 ms, as represented in figure 3.11(e). In $t=10$ – 16 ms, the time-variation of Ti atomic and TiO molecular densities become almost steady because of the balance between feedstock evaporation and diffusive transportation of Ti atoms and TiO molecules. Therefore, spatial distribution of Ti atom and TiO molecule shown in figure 3.12(c) are obtainable.

Finally, we mention the stopping period of Ti feedstock feeding. When the feedstock feeding and evaporation are finished, the temperature just under the outlet of the feeding tube recovers to higher values of 9000 K in the torch, as indicated in figure 3.11(d). In this case, TiO molecules are dissociated, leading to decreasing TiO molecular density, as shown in figure 3.12(d). At the same time, Ti atomic density is maintained, whereas TiO molecular density was decreased. This is true because Ti atoms are regenerated by a dissociation reaction of TiO molecules, as presented in figure 3.12(e). These TiO and Ti are transported downstream of the plasma torch and then the reaction chamber. Transported TiO and Ti are cooled down by temperature gradient in the plasma tail and by temperature decay due to Ar carrier gas injection and feedstock evaporation. If quenching gas is injected from the downstream of plasma torch, these gases could be more rapidly quenched. The high cooling rate allows the high efficiency nanoparticle nucleation. Moreover, it also prevents nanoparticle growth.

As described above, high-density Ti atoms are created in the off-axis region. High-

density TiO are produced in the on-axis region inside the plasma torch. They are then transported to the reaction chamber by gas flow. Such high-density Ti atoms can produce Ti clusters by homogeneous nucleation. Then they can be oxidized to create TiO_x clusters, i.e. the nuclei of TiO_2 NPs. However, the high-density TiO can also become TiO_x clusters by homogeneous nucleation with association. These clusters can grow by inhomogeneous processes including chemical vapour deposition from Ti, O, and TiO in gas phase. Then, coagulation and agglomeration occur to form NPs in the reaction chamber.

3.7 Summary

Two-dimensional optical emission spectroscopic measurement was conducted during TiO_2 nanopowder synthesis using an ICTP torch. This observation adopted an imaging spectroscopic system combined with two imaging spectrometers and two high-speed video cameras. Pure-Ti feedstock powder was injected intermittently into the ICTP torch in an interval to elucidate the Ti evaporation process of injected powder and formation of precursor TiO in the plasma torch. The spatiotemporal distribution of Ti I and TiO radiation intensities was observed simultaneously with the developed system. The observation results provided fundamental information on evaporation of Ti feedstock and transport of Ti atoms and then formation and transport process of TiO. These data will be useful to assess high efficient nanoparticle synthesis using the inductively coupled thermal plasmas.

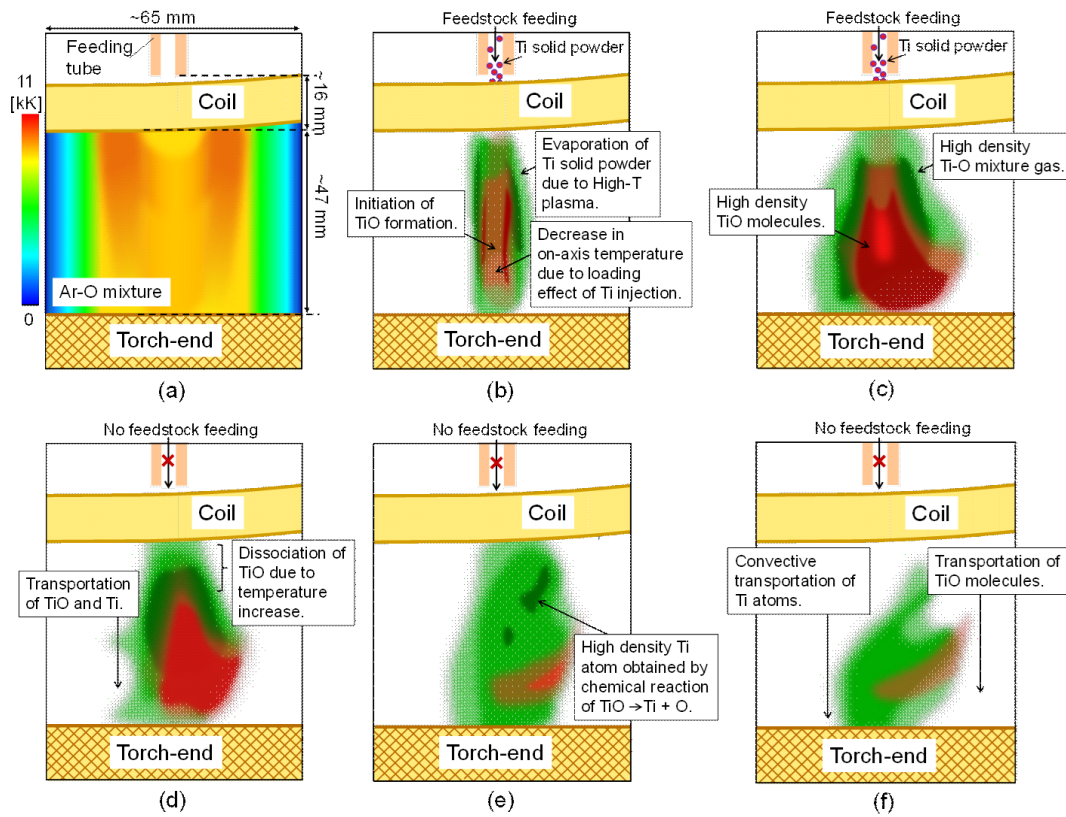


Fig. 3.12: Temporal and spatial variation of Ti atomic density and TiO molecular density in the ICTP torch estimated from two-dimensional spectroscopic observation result for 27%DF_{valve}. (a) Before feedstock injection into the ICTP torch ($t=0$ ms), (b) Ti feedstock feeding, Ti evaporation and TiO formation ($t \sim 7$ ms), (c) Formation of high-density Ti-O mixture and TiO molecules ($t \sim 14$ ms), (d) TiO transport and TiO dissociation attributable to the increased temperature by stopping of feedstock feeding ($t \sim 18$ ms), (e) Formation of high-density Ti atoms attributable to dissociation reaction of $\text{TiO} \rightarrow \text{Ti} + \text{O}$ ($t \sim 20$ ms), and (f) Convective transport of Ti atoms ($t \sim 22$ ms).

References

- [1] Malato S, Blanco J, Alarcon D C, Maldonado M I, Fernandez-Ibanez P and Gernjak W 2007 Photocatalytic decontamination and disinfection of water with solar collectors. *Catalysis Today* **122** pp.137–49
- [2] Li J, Zhao X, Wei H, Gu Z Z, and Lu Z 2008 Macroporous ordered titanium dioxide (TiO₂) inverse opal as a new label-free immunosensor. *Analytica Chimica Acta* **625** pp.63–9
- [3] Gratzel M 2001 Photoelectrochemical cells. *Nature* **414** pp.338–44
- [4] Biju K P and Jain M K 2008 Effect of crystallization on humidity sensing properties of sol-gel derived nanocrystalline TiO₂ thin films. *Thin Solid Films* **516** pp.2175–80
- [5] Park J H, Park O O, and Kim S 2006 Photoelectrochemical water splitting at titanium dioxide nanotubes coated with tungsten trioxide. *Appl. Phys. Lett.* **89** 163106
- [6] Tsai Y C, Hsi C H, Bai H, Fan S K and Sun D H 2012 Single-step synthesis of Al-doped TiO₂ nanoparticles using non-transferred thermal plasma torch. *Jpn. J. Appl. Phys.* **51** 01AL01
- [7] Shon K H, Cho L D, Na H S, Kim B J, Park J H and Kim H J 2009 Development of a novel method to prepared Fe- and Al-doped TiO₂ from wastewater. *J. Ind. Eng. Chem.* **15** pp.476–82
- [8] Barolo G, Livraghi S, Chiesa M, Cristina M, Paganini C and Giamello E 2012 Mechanism of the photoactivity under visible light of N-doped titanium dioxide. charge carriers migration in irradiated N-TiO₂ investigated by electron paramagnetic resonance. *J. Phys. Chem. C* **116** pp.20887–94

-
- [9] Lee K N, Kim Y, Lee C W and Jai-Sung Lee J S 2011 Simultaneous amination of TiO₂ nanoparticles in the gas phase synthesis for bio-medical applications *Mater. Sci. Eng.* **18** 082021
- [10] Mio M, Kogoma M, Fukui H, and Takeda A 2010 Control of inflammation using adsorption of inflammatory by nano-particles *Chem. Eng.* **55** pp.603-8 (in Japanese)
- [11] Zabet K A and Dhirani A -A 2008 Charge Transport in Nanoparticle Assemblies. *Chem. Rev.* **108** pp.4072–124
- [12] Shigeta M and Murphy A B 2011 Thermal plasmas for nanofabrication. *J. Phys. D: Appl. Phys.* **44** 174025
- [13] Girshick S L, Chiu C P, Muno R, Wu C Y, Yang L, Singh S K, and McMurry P H 1993 Thermal plasma synthesis of ultrafine iron particles. *J. Aerosol Sci.* **24** pp.367–82
- [14] Shigeta M, Watanabe T, and Nishiyama H 2004 Numerical investigation for nanoparticle synthesis in an RF inductively coupled plasma. *Thin Solid Films* **457** pp.192–200
- [15] Oh S M and Ishigaki T 2004 Preparation of pure rutile and anatase TiO₂ nanopowders using RF thermal plasma. *Thin Solid Films* **457** pp.186–91
- [16] Lee J E, Oh S M, and Park D W 2004 Synthesis of nano-sized Al doped TiO₂ powders using thermal plasma. *Thin Solid Films* **457** pp.230–4
- [17] Ishigaki T, Oh S M, Li J G, and Park D W 2005 Controlling the synthesis of TaC nanopowders by injecting liquid precursor into RF induction plasma. *Sci. & Technol. Advanced Mater.* **6** pp.111–8
- [18] Tong L and Reddy R G 2006 Thermal plasma synthesis of SiC nano-powders/nano-fibers. *Materials Research Bulletin* **41** pp.2303–10
- [19] Ishigaki T and Li J G 2007 Synthesis of functional nanocrystallites through reactive thermal plasma processing. *Sci. & Technol. Advanced Mater.* **8** pp.617–23

-
- [20] Li J G, Ikeda M, Ye R, Moriyoshi Y, and Ishigaki T 2007 Control of particle size and phase formation of TiO₂ nanoparticles synthesized in RF induction plasma. *J. Phys. D: Appl. Phys.* **40** pp.2348–53
- [21] Tanaka Y, Nagumo T, Sakai H, Uesugi Y, and Nakamura K 2010 Nanoparticle synthesis using high-powered pulse-modulated induction thermal plasma. *J. Phys. D: Appl. Phys.* **43** 265201
- [22] Tanaka Y, Sakai H, Tsuke T, Uesugi Y, Sakai Y, and Nakamura K 2011 Influence of coil current modulation on TiO₂ nanoparticle synthesis using pulse-modulated induction thermal plasmas. *Thin Solid Films* **519** pp.7100–05
- [23] Tanaka Y, Tsuke T, Guo W, Uesugi Y, Ishijima T, Watanabe S, and Nakamura K 2012 A large amount synthesis of nanopowder using modulated induction thermal plasmas synchronized with intermittent feeding of raw materials. *J. Phys. D: Conf. Ser.* **406** 012001
- [24] Tanaka Y, Sakai H, Tsuke T, Guo W, Uesugi Y, Sakai Y and Nakamura K 2011 Nanoparticle synthesis using high-power modulated induction thermal plasmas with intermittent synchronized feeding of raw materials. *Proc. 20th Int. Symp. Plasma Chem. ISPC-20*, 346, Philadelphia, USA
- [25] Tanaka Y and Sakuta T 2003 Temperature control of Ar induction thermal plasma with diatomic molecular gases by pulse-amplitude modulation of coil current. *Plasma Sources Sci. & Technol.* **12** pp.69–77
- [26] Tanaka Y, Uesugi Y, and Sakuta T 2007 Controlling the number of excited atoms flowing into the reaction chamber using pulse-modulated induction thermal plasmas at atmospheric pressure. *Plasma Sources Sci. & Technol.* **16** pp.281–9
- [27] Tanaka Y, Guo W, Kodama N, Uesugi Y, Ishijima T, Watanabe S and Nakamura K 2013 A novel approach for large amount synthesis of TiO₂ nanopowder using modulated induction thermal plasmas with time-controlled feeding of feedstock. *Proc. 21st Int. Symp. Plasma Chem. ISPC-21*, 52, Cairns, Australia

-
- [28] Kodama N, Kita K, Tanaka Y, Uesugi Y, Ishijima T, Watanabe S, and Nakamura K 2014 A method for large-scale synthesis of Al-doped TiO₂ nanopowder using pulse-modulated induction thermal plasmas with time-controlled feedstock feeding. *J. Phys. D: Appl. Phys.* **47** 195304
- [29] Kodama N, Kita K, Tanaka Y, Uesugi Y, Ishijima T, Watanabe S, and Nakamura K 2014 Two-dimensional spectroscopic observation of a pulse-modulated induction thermal plasma torch for nanopowder synthesis. *J. Phys.: Conf. Ser.* **550** 012026
- [30] Chase M W 1998 *NIST-JANAF thermochemical tables fourth Ed.* J. Phys. Chem. Ref. Data
- [31] Boulos M I, Fauchais P, and Pfender E 1994 *Thermal plasmas: fundamentals and applications volume 1.* New York: Plenum Press
- [32] Chapman S and Cowling T 1952 *The mathematical theory of non-uniform gases.* New York: Cambridge University Press
- [33] Abrahamson A A 1969 Born-Mayer-Type interatomic potential for neutral ground-state atoms with $Z = 2$ to 105. *Phys. Rev.* **178** pp.76-9
- [34] Monchick L 1959 Collision integrals for the exponential repulsive potential. *Phys. Fluids* **2** pp.695-700
- [35] Samsonov G V 1982 *The oxide handbook 2nd ed.,* IFI/Plenum, New York
- [36] CrystalMaker support page, <http://crystalmaker.com/support/tutorials/crystalmaker/atomic-radii/>
- [37] Hirschfelder J O, Curtiss C F, and Bird R B 1968 *Molecular theory of gases and liquids.* Wiley and Sons
- [38] Rapp D, and Francis W E 1962 Charge exchange between gaseous ions and atoms. *J. Chem. Phys.* **37** pp.2631-45
- [39] Yos J M 1967 *Transport properties of nitrogen, hydrogen, oxygen and air to 30000 K.* Research and advanced development division AVCO corporation, Massachusetts, Amendments to AVCO RAD-TM-63-7

-
- [40] Patankar S V 1980 *Numerical heat transfer and fluid flow*. New York: Hemisphere
- [41] The Japan Institute of Metals 2007, *Metals data book fourth ed.* Maruzen

Chapter 4

Influence of coil-current modulation on Ti feedstock evaporation and formation of TiO precursor molecule

4.1 Introduction

Nanoparticles/nanopowder are expected as promising next generation material used in various applications such as in electronics, energy and environmental fields. Titanium dioxide (TiO_2) nanopowder is receiving attention as photocatalyst material, photonic crystals, photovoltaic cells, and gas sensors [1]– [4]. However, TiO_2 works as photocatalyst only under ultraviolet light because of its wide energy band gap. Attention has also been paid to TiO_2 nanopowder with metallic-ion doping as photocatalyst material. This is because the impurity energy levels in the band gap improve their visible light absorption efficiency [5]. Another application of metallic-ion doped TiO_2 is in the biomedical field [8]. It has been recently reported that Al^{3+} -doped TiO_2 nanopowder has a inflammatory protein adsorption ability [7]. For biomedical applications, no contamination in TiO_2 or metallic-ion doped TiO_2 nanopowder is greatly desired. However, effective mass production methods have not yet been developed for such TiO_2 and metallic-ion doped TiO_2 nanopowder without contamination.

Various kinds of nanopowder synthesis methods have been developed so far. Among them, the inductively-coupled thermal plasma (ICTP) method offers great advantages [2]. For example, it can provide nanopowder with short processing time, and with simple one-step and continuous process. It can offer nanopowder in non-equilibrium or metastable

phase. The most important feature of the ICTP method is that it can essentially synthesize nanopowder without contamination due to the absence of electrodes. Many researchers have studied various kinds of nanopowder synthesis method using a steady-type of ICTP. However, nanopowder synthesis methods using steady-type ICTPs still have some issues such as the difficulty in controlling the synthesized particles size, and in the scale-up of the process for higher production rate [3]– [17].

In the chapter 2, large-scale nanopowder synthesis method was investigated by using the pulse-modulated induction thermal plasma (PMITP) with time-controlled feedstock feeding (TCFF), i. e. PMITP+TCFF method. The PMITP was developed to be controlled the time evolution of the temperature and reactive species fields in thermal plasmas using the coil current modulation. In addition to this, a method was also developed for feeding of feedstock powder. In this method, feedstock powder is intermittently and synchronously supplied with the coil current modulation of the PMITP. In our previous work, the PMITP+TCFF method was applied to synthesize pure TiO_2 and Al^{3+} -doped TiO_2 nanopowder with large-scale production. Results indicated that this method using a 20 kW PMITP offered a high production rate of 500 g h^{-1} for pure TiO_2 nanopowder with a mean particle diameter around 43 nm, and 400 g h^{-1} for Al^{3+} -doped TiO_2 nanopowder with a mean particle diameter around 67 nm [21, 26].

For a detailed understanding of this PMITP+TCFF method, it is important to study the evaporation process of the supplied feedstock powder and precursor production in gas phase for precise control of TiO_2 nanoparticle synthesis. Thus in the Chap. 3, fundamental information of Ti feedstock evaporation and precursor TiO formation processes were obtained from two-dimensional optical emission spectroscopy (2D OES) during TiO_2 nanopowder synthesis using ICTP with single-shot feedstock injection.

This chapter describes the 2D OES results during TiO_2 nanopowder synthesis using PMITP+TCFF method to discuss effect of coil-current modulation and intermittent feedstock feeding on feedstock Ti evaporation and precursor TiO formation in the ICTP/PMITP torch. For this purpose, Ti feedstock was continuously or intermittently injected into the conventional (i.e. non-modulated) ICTP torch or PMITP torch. The spatiotemporal variation for radiation intensities from some atomic spectral lines and molecular emission bands were measured during the coil current modulation and the intermittent feedstock pow-

der injection. Finally, the evaporation of the feedstock powder and precursor formation processes are discussed from the obtained results.

4.2 PMITP+TCFF approach for large-scale nanopowder synthesis

The PMITP was developed to control the temperature and reactive species in the thermal plasma jet. The PMITP is sustained by the coil current modulated in a rectangular waveform. The PMITP has four control parameters: on-time, off-time, HCL and LCL. The ‘on-time’ is the duration of the higher current level (HCL) phase where a higher input power is supplied to the PMITP. In this ‘on-time’ temperatures in the plasma torch are higher. The ‘off-time’ represents the duration of the lower current level (LCL) phase where the input power to the PMITP is lower. During this phase, the plasma jet temperature is lower. In addition to these four parameters, we also defined a shimmer current level (SCL) and duty factor (DF). The SCL is the ratio of LCL to HCL, and the DF is the ratio of ‘on-time’ to a modulation cycle (‘on-time’+ ‘off-time’). The condition of 100%SCL or 100%DF corresponds to the non-modulation condition.

Figure 4.1 illustrates the comparison between two methods for nanopowder synthesis: One is the conventional method in which a steady type of ICTP (non-modulated ICTP) is used with continuous feedstock feeding, and the other is the PMITP+TCFF method. In the PMITP+TCFF method, a solenoid valve with a response time of 2 ms is installed on the feedstock feeding tube between the powder feeder and the PMITP torch. By switching the solenoid valve on and off, the feedstock is fed intermittently into the plasma torch intermittently and synchronously with the coil-current modulation. The feedstock is supplied into the plasma torch only during the high-temperature period. This intermittently and synchronously feedstock feeding can be executed by controlling the delay time t_d for opening the valve in reference to the pulse modulation signal of the PMITP coil-current. In the actual experiment, the feedstock reaches the PMITP torch in a finite time of t_{adt} . The t_{adt} was measured in our previous work as about 6-8 ms. Therefore, the actual delay time to the coil-current modulation signal is $(t_d + t_{adt}) \simeq (t_d + 7)$ ms.

The injected feedstock is rapidly and completely evaporated during the high-temperature

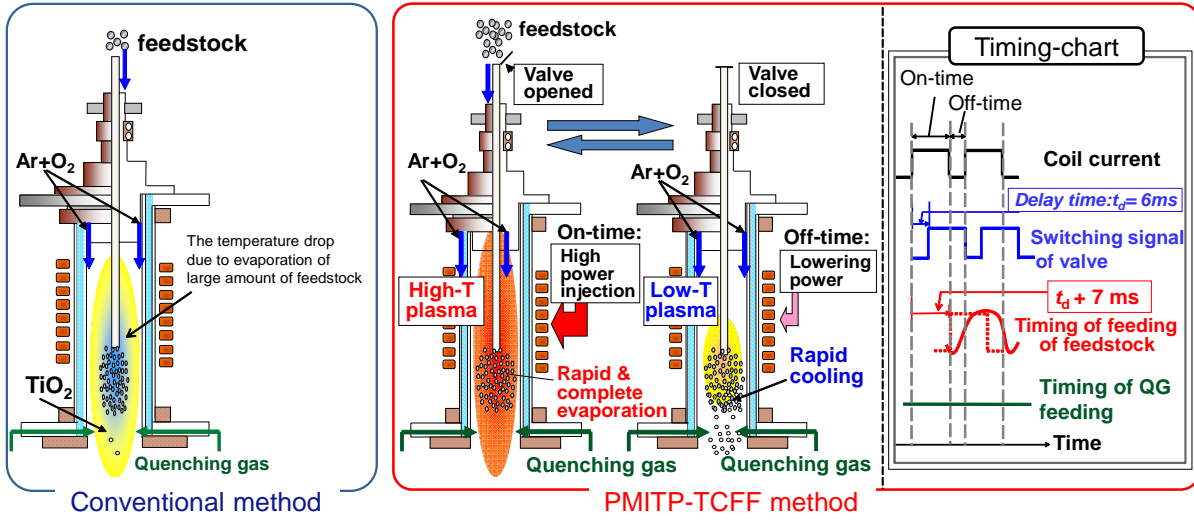


Fig. 4.1: Method for large-scale nanopowder synthesis using induction thermal plasma. Left-hand side: conventional non-modulated ICTP with continuous feedstock feeding; Right-hand side: PMITP with intermittent feedstock feeding.

phase of the PMITP. The feedstock feeding is stopped by closing the solenoid valve during successive off-time. In the off-time, the evaporated feedstock material is rapidly and efficiently cooled down because the thermal plasma temperature decreases by the decreased input power to the PMITP. The evaporated Ti atom is mixed with Ar and O atoms from the thermal plasmas. The rapid cooling of the above atomic mixture promotes the nucleation of nanoparticles under the saturated vapor conditions. The nucleated nanoparticles are transported downstream of the PMITP while particle growth take place. The quenching gas (QG) injection downstream of the torch nozzle further cools the evaporated material to promote the nucleation of nanoparticles, thus restraining the particle growth. In this way, the PMITP+TCFF method enables the synthesis of nanopowder with a high production rate.

4.3 Experimentals

4.3.1 Experimental conditions

The evaporation behavior of the powder injected in the PMITP+TCFF plasma torch is investigated. For comparison, we also measured the behavior for conventional non-modulated ICTP with continuous powder feeding, and for the PMITP with continuous powder feeding. Table 2.1 summarizes the experimental conditions. The plasma torch used is the same we used in our previous work [21, 26]. The total sheath gas flow rate was fixed at 100 l min^{-1} . The O_2/Ar gas admixture ratio was set at 10mol% in the sheath gas. The pressure in the chamber was regulated at 300 torr (=40 kPa). The quenching gas (QG) was not supplied in this work. The time-averaged input power was fixed at 20 kW. It is noted that instantaneous input power was changed periodically with time according to the coil current modulation. The modulation cycle was fixed at 15 ms. The DF of the modulated coil current was fixed at 80%. The SCL was set to two conditions: 100% (non-modulation condition) and 80%. The feedstock was Ti powder with a mean diameter of $27 \mu\text{m}$ (TILOP-45; Osaka Titanium Technologies Co.Ltd). The feedstock was fed into the thermal plasma using a rotary powder feeder with Ar carrier gas flow. The Ar carrier gas flow rate was fixed at 4 l min^{-1} . In the present experiments, the feeding rate of the feedstock was regulated at $4\text{-}7 \text{ g min}^{-1}$. This feed rate is much lower than what is typically used for synthesis of large amounts of nanopowder [21, 26]. This small feed rate was adopted to carefully investigate the evaporation process. We set two feedstock feeding methods: the conventional continuous feeding and the intermittent feeding methods. The intermittent feedstock feeding was synchronized with the coil current modulation with a delay time t_d of 6 ms. The open and close time of the valve for the intermittent feedstock feeding were 12 ms and 3 ms, respectively. The powder was actually fed from the tip of the water-cooled feeding tube directly to the thermal plasma region. The tip of the water-cooled feeding tube was located between just above the coil end on the axis of the torch to allow spectroscopic observation.

Table 4.1: Experimental conditions.

Time-averaged input power	20 kW
Fundamental frequency of the coil current	450 kHz
Pressure	300 Torr (~ 40 kPa)
Sheath gas composition	Ar: 90 L min^{-1} , O ₂ : 10 L min^{-1}
Modulation	Pulse-modulation or w/o
Modulation cycle	15 ms
Shimmer current level(SCL)	100% (Non-modulation) or 80%
Duty factor (DF)	80% (On-time:Off-time=12 ms:3 ms)
Quenching gas	Non-injection
Feedstock feeding	Continuous or Intermittent
Valve-open/close cycle	15 ms
Delay time for valve signal	6 ms
DF _{valve}	80%DF _{valve} (12 ms open/3 ms close)
Powder feed rate g_{pow}	4-7 g min ⁻¹
Feedstock	100wt%Ti powder $\bar{d} = 27 \mu\text{m}$, $d < 45 \mu\text{m}$

4.3.2 2D OES conditions

The 2D OES measurement was carried out using a two-dimensional imaging spectrometry system shown in Fig. 4.2.

Two-dimensional optical emission spectroscopy system (Anfi Inc., AN-IMC-DD) contains an objective lens (Nikon, AF Zoom-Nikkor 80-200 mm f/2.8D ED), a two-dimensional imaging spectrophotometer (Princeton Inst., Acton Spectra Pro 2300i), and a high speed video camera (NAC Imaging Tech., GX-8). The observation conditions are listed in table 4.2. The observation area was set to a $78 \times 58 \text{ mm}^2$ region below the coil end as shown in Fig. 4.2. It is noted that the feedstock powder is supplied just above the coil end from the water-cooled feeding tube. The 1200 grooves/mm of diffraction grating was used for the spectrophotometer. In this case, the wavelength resolution of the spectrometer was 0.4

Table 4.2: The 2D OES measurement conditions.

Observation area	$78 \times 58 \text{ mm}^2$ region below the coil end
Diffraction grating	1200 grooves/mm
Wavelength resolution	0.4 nm
Spectral lines observed	Ar I (811.53 nm), O I (777.54 nm), Ti I (453.32 nm) and TiO (615.91 nm)
Frame rate for high speed video camera	3000 fps

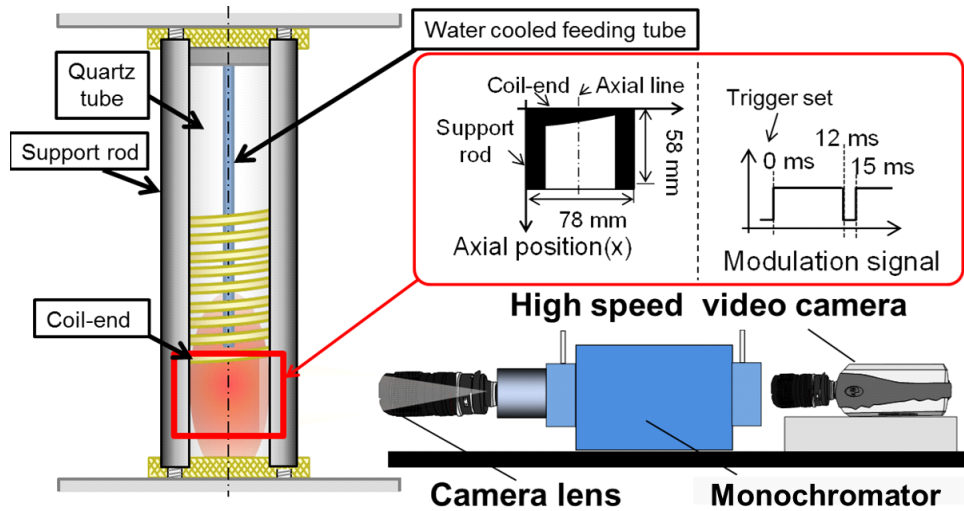


Fig. 4.2: The 2D OES system and observation area for an induction thermal plasma torch.

nm. This system can resolve time varying two-dimensional images at a selected wavelength using a high speed video camera. The atomic spectral lines of Ar I at a wavelength of 811.53 nm, O I at 777.54 nm were observed in the thermal plasma itself, and an atomic line of Ti I at 453.32 nm from the evaporated material. We also measured the molecular emission of TiO around 615.91 nm, which specie is formed by the chemical reaction of $\text{Ti} + \text{O}$. The frame rate of the high speed camera was set at 3000 fps.

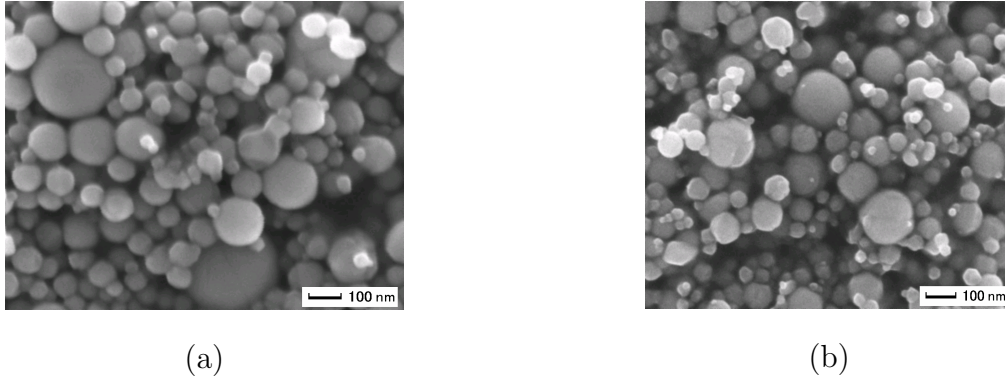


Fig. 4.3: FE-SEM images of nanoparticles synthesized (a) by non-modulated ICTP, and (b) by PMITP with intermittent feedstock feeding (80%SCL) [15].

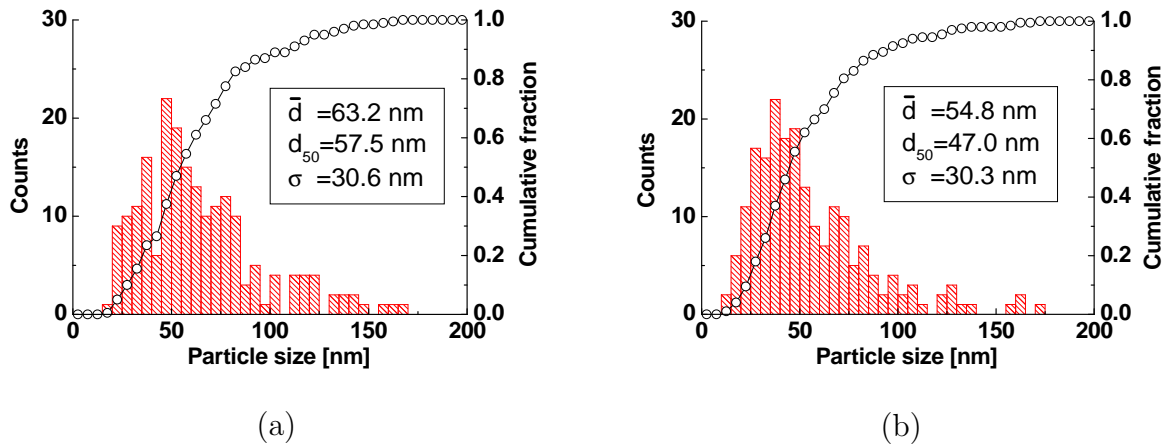


Fig. 4.4: Particle size distribution of nanoparticles synthesized (a) by non-modulated ICTP and (b) by PMITP with intermittent feedstock feeding (80%SCL) [15].

4.4 Results and discussions

4.4.1 Synthesized nanoparticles

Figure 4.3 shows FE-SEM images of nanoparticles synthesized (a) by non-modulated ICTP (100%SCL) with continuous feedstock feeding, and (b) by PMITP (80%SCL) with intermittent feedstock feeding. As seen in Fig. 4.3, in both cases (a) and (b), many nanoparticles with diameters less than 100 nm were produced. The adopted feedstock feed rates being much lower typical value used in synthesis of large-scale of nanoparticles [21,26], the feedstock was completely evaporated.

From randomly selected 200 particles in each of these FE-SEM images, the particle size distribution of synthesized particles were evaluated for different conditions. Figure 4.4 depicts the particle size distribution of nanoparticles synthesized (a) by non-modulated ICTP

with continuous feedstock feeding, and (b) by PMITP with intermittent feedstock feeding (80%SCL). The mean particle diameter, and the standard deviation are also represented in figure 4.4. Nanoparticles with mean particle diameters around 55-65 nm were synthesized by the both methods even without quenching gas injection. In the next section, we focus an attention on the influence of the coil-current modulation and intermittent feedstock feeding on the feedstock evaporation process as well as the vapor cooling process.

4.4.2 Two-dimensional distribution of radiation intensities

Figures 4.5– 4.7 show temporal variations of the two-dimensional distribution of radiation intensities for (a) Ar I and (b) O I lines from the thermal plasma itself, that of (c) Ti I line from the evaporated material, and those of (d) TiO from by-product of Ti and O. In these figures, the timing t was also denoted at the bottom-left of each image. The coil current amplitude rises up at $t= 0$ ms, and falls down at $t= 12$ ms. In case of the non-modulated ICTP with continuous feedstock feeding, the Ar I and O I radiation intensities were almost unchanged with time as shown in Figs. 4.5 (a) and (b). The Ar I and O I radiation intensities were almost uniform in the radial direction just below the coil end. However, the Ar I and O I radiation intensities decreased sharply downstream around the bottom of these figures, clearly indicating that the plasma tail of the ICTP is rapidly quenched. On the other hand, Ti atoms emit strongly around the axis, and especially in off-axis region below the coil end, as depicted in Fig. 4.5 (c). This implies that the injected Ti powder was evaporated by the thermal plasma to produce a high-density of Ti atoms, which were transported downstream. The Ti radiation intensity observed on the axis is lower than that in the fringe. This may be because the induction heating is present in the fringe, and the Ar carrier gas cools down the temperature on the axis. Figure 4.5 (d) presents the TiO spectral intensity distribution. The TiO is one important precursor for TiO₂ nanoparticle formation. The radiation intensity of TiO was detected locally on the axis. This means that TiO was formed in gas phase around the axis, and it transferred downstream by the Ar carrier gas flow.

Results for the PMITP with continuous feedstock feeding are presented in Fig. 4.6. The Ar I and O I lines had strong radiation intensities detectable from $t=3$ –12 ms during the on-time, whereas these intensities became weaker in the off-time as shown in Figs. 4.6

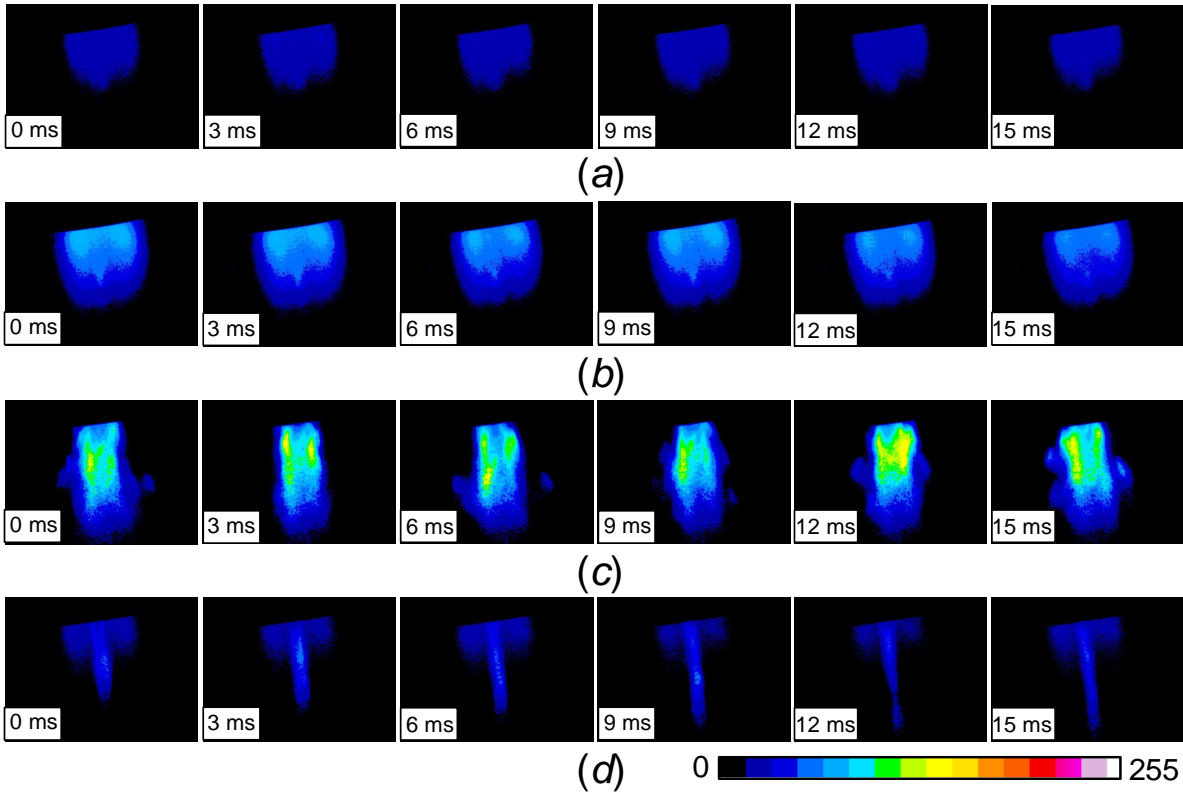


Fig. 4.5: Two-dimensional distribution of radiation intensities for the non-modulated ICTP (100%SCL) with continuous feedstock feeding. (a) Ar I: 811.53 nm, (b) O I: 777.54 nm, (c) Ti I: 453.32 nm, and (d) TiO: 615.91 nm.

(a) and (b). These results indicate that high and low temperature fields in the PMITP torch were repeatedly created with the coil-current modulation. Panel (c) indicates that Ti I radiation intensity from evaporated material was also varied with the coil-current modulation. The TiO radiation intensity were also detected on the axis with a peculiar time variation according to the coil-current modulation.

The most important result is presented in Fig. 4.7 for the PMITP with intermittent feedstock feeding. In this case, Ar I and O I radiation intensities similarly changed with the coil-current modulation. However, a large difference appears in Ti and TiO radiation intensities from those observed with continuous feedstock feeding. The radiation intensity of Ti I in intermittent feedstock feeding became much stronger than with continuous feedstock feeding. This is attributed to the fact that intermittent feedstock feeding has a higher

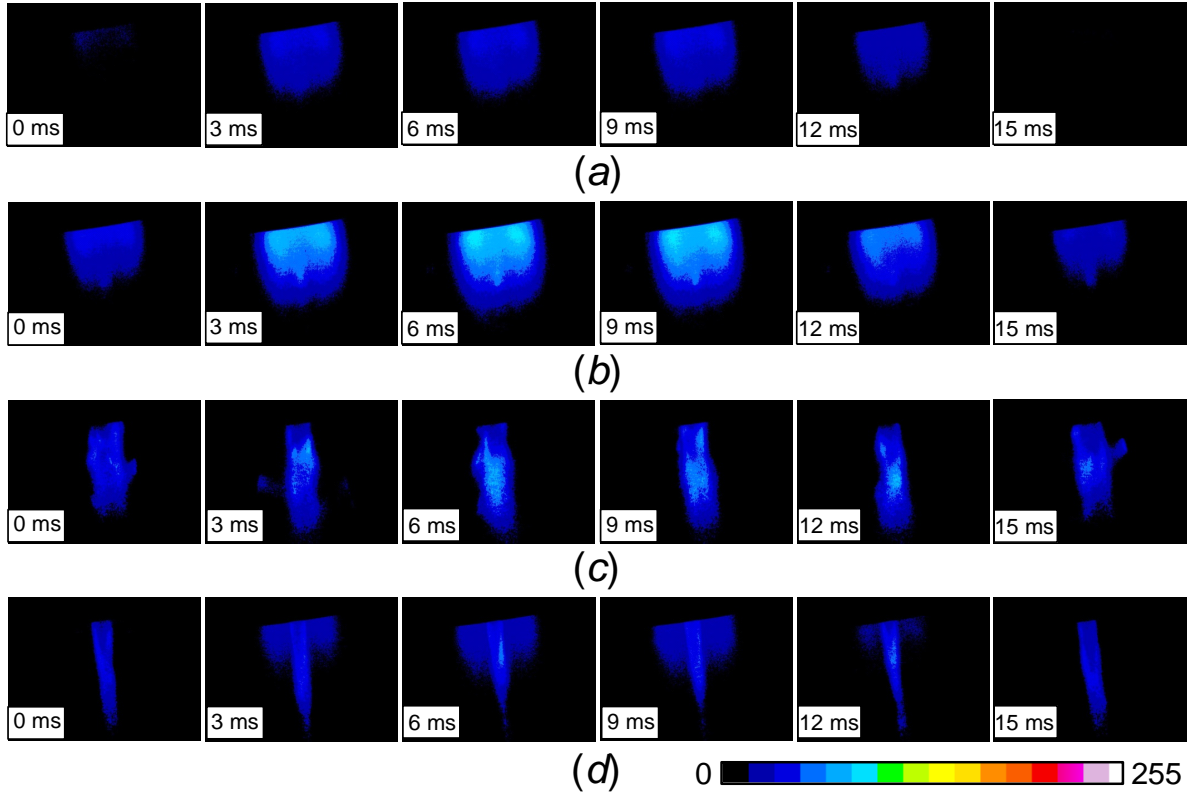


Fig. 4.6: Two-dimensional distribution of radiation intensities from the PMITP for 80%SCL with continuous feedstock feeding. (a) Ar I: 811.53 nm, (b) O I: 777.54 nm, (c) Ti I: 453.32 nm, and (d) TiO: 615.91 nm.

instantaneous feeding rate during the on-time, and that the fed feedstock is efficiently evaporated by during the PMITP on-time. The Ti I radiation intensity depends on both Ti excitation temperature and Ti atomic density determined by evaporation amount of Ti feedstock. The result of the high Ti I intensity in panel (c) indicates that high-density Ti is present almost without a temperature drop even from feedstock loading because of high input-power to the PMITP during the on-time. In addition, the TiO intensity was strong just under the coil end. This result suggests that larger amounts of TiO was formed under the coil end region in this condition, and that it was transported downstream of the PMITP torch.

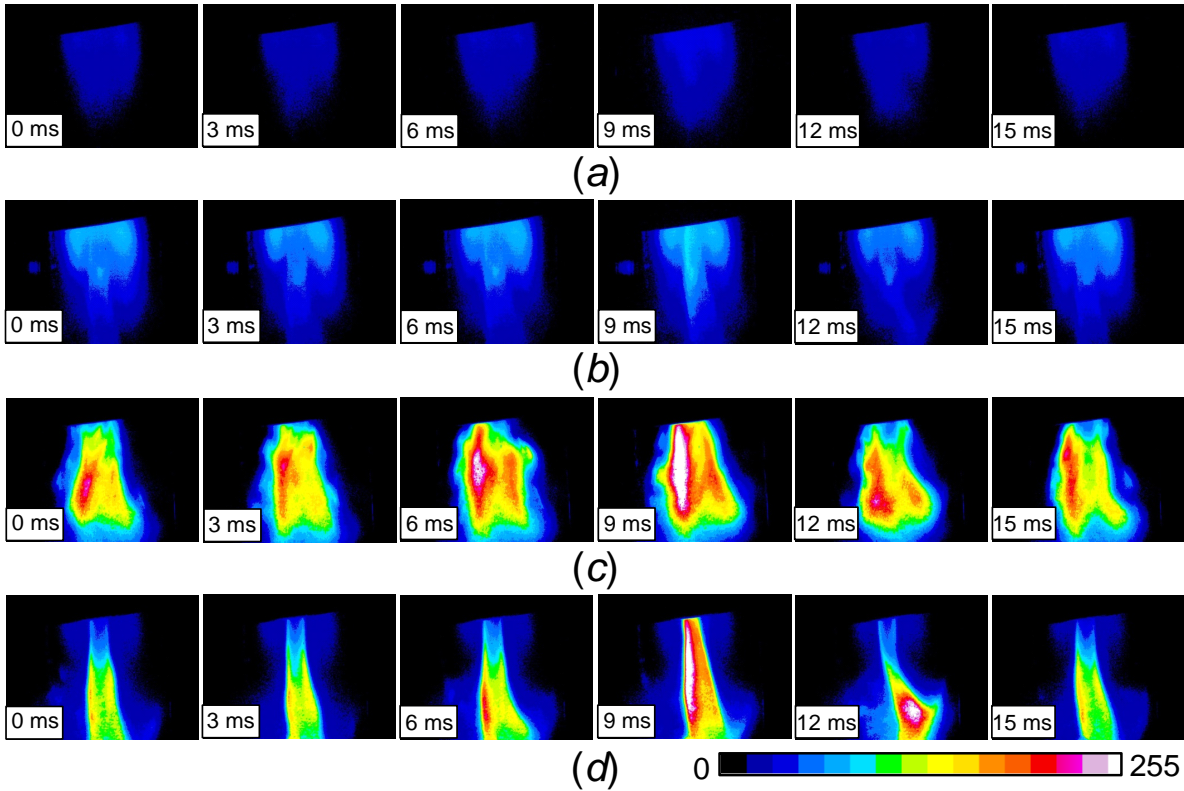


Fig. 4.7: Two-dimensional distribution of radiation intensities from the PMITP for 80%SCL with intermittent feedstock feeding. (a) Ar I: 811.53 nm, (b) O I: 777.54 nm, (c) Ti I: 453.32 nm, and (d) TiO: 615.91 nm.

4.4.3 Temporal variation in radiation intensities for different spectral lines

Figure 4.8 illustrates the temporal variations in the radiation intensities of Ar I, O I, Ti I and TiO observed 10 mm, 20 mm and 30 mm below the coil end on the axis of the plasma torch. Panel (a) is the result for non-modulated coil current condition with continuous feedstock feeding; panel (b) is that for modulated coil current condition with continuous feedstock feeding, and panel (c) corresponds to the result for modulated coil current with intermittent feedstock feeding.

In case of non-modulation with continuous feedstock feeding, the Ar I and O I have almost unchanged radiation intensities, indicating stable sustainability of the thermal plasma

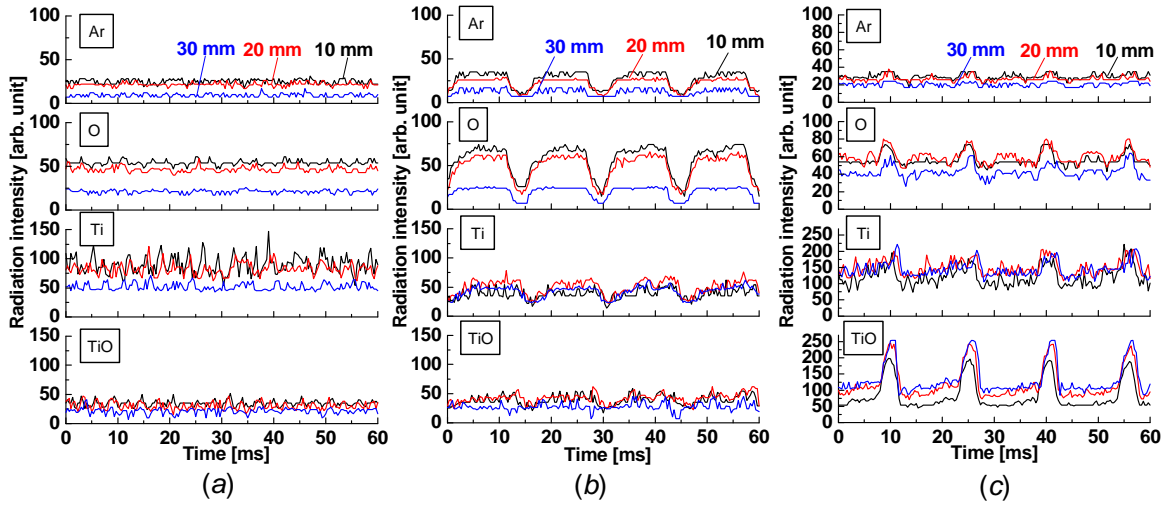


Fig. 4.8: Temporal variation of radiation intensities of different spectral lines observed below the coil end. (a) Non-modulated coil current with continuous feedstock feeding, (b) modulated coil current of 80%SCL with continuous feedstock feeding, (c) modulated coil current of 80%SCL with intermittent feedstock feeding.

torch. The radiation intensity of Ti I fluctuate due to the fluctuations in feedstock powder feeding and its evaporation. The TiO intensity is also hardly changed with time.

For modulated coil current with continuous feedstock feeding, the Ar I and O I radiation intensities periodically varied following the coil-current modulation. This result clearly shows that high-temperature and low-temperature fields in the PMITP torch were generated repeatedly. The radiation intensities from Ti I and TiO also change with time similarly.

A significantly different behavior of the time-varying radiation intensities for modulated coil current with intermittent feedstock feeding is observed. First, Ar I in the panel (c) has almost unchanged radiation intensity although the coil current was modulated. The O emission line intensity at 777.54 nm is almost constant similar to Ar I intensity except just before transition to the off-time. The radiation intensity of Ti I changes according to the pulse modulation but in almost triangular waveform. On the other hand, the TiO spectral intensity changes with time in periodical waveform, having a drastic increase just before transition to the off-time. We infer from those observations that the Ar I has almost unchanged intensity, which shows the unchanged plasma temperature in spite of the pulse

modulation. This is inferred due to the energy balance between the increased input power by the coil current modulation and the increased loss power for evaporation of large amounts of feedstock during the on-time. The O emission line intensity increase just before transition to the off-time may be caused only by overlapping intensities from TiO band spectra around this wavelength because TiO band spectra has a wide wavelength region and high intensity in this case. The drastic increase in TiO emission intensity may arise from a remarkable increase in TiO number density just before transition to the off-time. The remarkable increase in the TiO number density originates from promotion of formation reaction $\text{Ti} + \text{O} \rightarrow \text{TiO}$ because of Ti density increase from feedstock evaporation.

4.4.4 Discussion on Ti evaporation and TiO formation in PMITP+TCFF method

The observations presented in the preceding sections lead to the following understanding of the evaporation process of Ti feedstock, formation of TiO, and the transport of TiO(precursor of TiO_2 nanoparticles). Figure 4.9 illustrates the schematic interpretation for phenomena happening in the plasma torch. The steps described as follows, where t is the time in Fig. 4.7:

- (a) The Ti feedstock is supplied into the high-temperature thermal plasma just before the ‘on-time’ through the feeding tube. High Ar and O atomic density regions are present in off-axis region.
- (b) At $t= 0$ ms, the coil current amplitude is increased to establish the high temperature thermal plasma. The Ti feedstock starts being evaporated to generate a high atomic density Ti region. Ti atoms in gas phase then diffuse in all directions.
- (c) From $t= 3$ ms, a region containing Ti and O atoms is formed between the center-axis and the high-temperature region, and then TiO formation is initiated there.
- (d) Around $t= 6$ ms, TiO density increases with time around the center axis.
- (e) Around $t= 9$ ms, further higher TiO density region is formed around the center axis.
- (f) At $t= 15$ ms, TiO is transported downstream of the PMITP torch between off-time.

4.5 Summary

The two-dimensional distributions of spectral radiation intensities from pulse modulated induction thermal plasmas (PMITP) were investigated with continuous/intermittent feedstock feeding for TiO₂ nanopowder synthesis. For this measurement, the 2D OES system, consisted of an imaging spectrometer and a high speed video camera, was adopted. The spatiotemporal distribution of radiation intensities for Ar I, O I, Ti I and TiO spectra were observed selectively by the 2D OES measurement. The observations provided spatial information on the evaporation of the Ti feedstock, mixing of Ti and O atoms, formation of TiO and the transport of TiO, i.e. the precursor of TiO₂ nanoparticles. This study clearly highlights the advantage of using the pulse modulation of the RF power and synchronous injection of feedstock over the conventional continuous process.

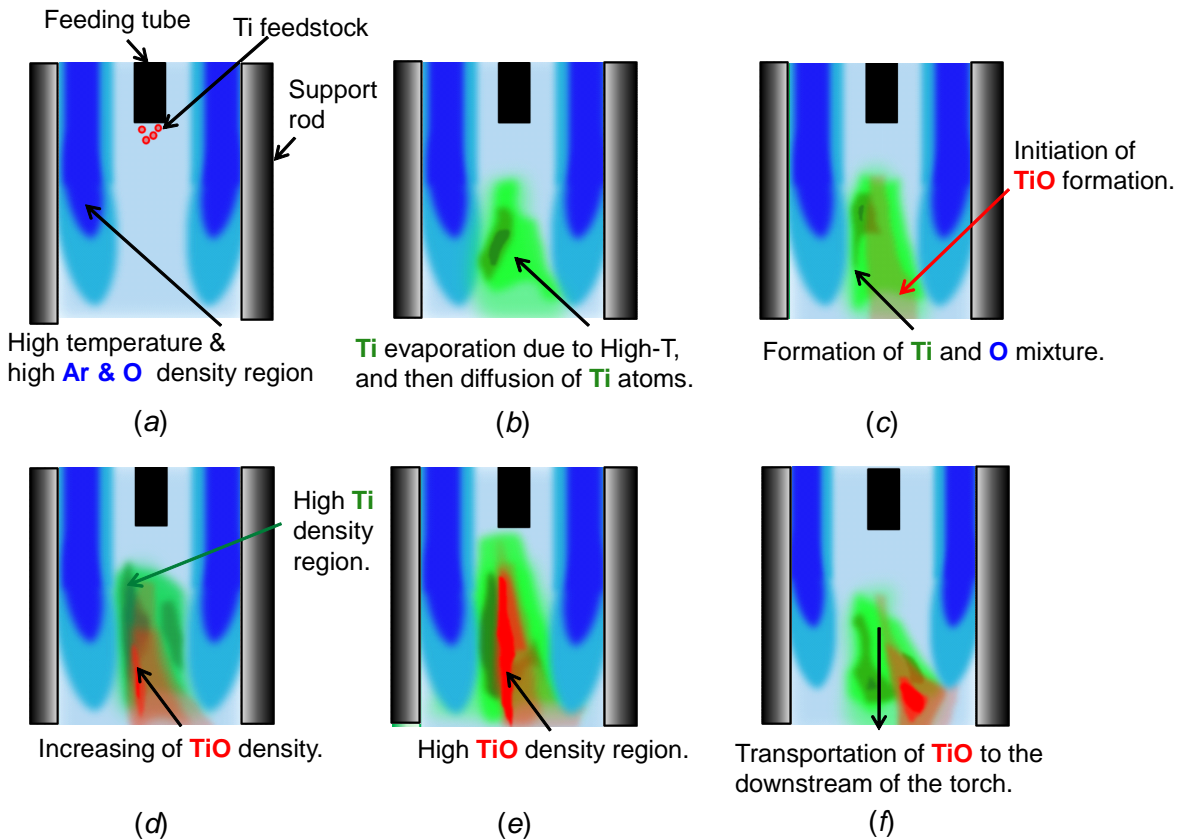


Fig. 4.9: An interpretation on the evaporation process of Ti feedstock and the formation of TiO for pulse-modulation with intermittent feedstock feeding. (a) Input powder increase and initiation of feedstock feeding in on-time; (b) The evaporation of Ti feedstock, and then diffusion of Ti atoms in on-time ($t=0$ ms); (c) Mixing of Ti and O atoms, and initiation of TiO formation around the axis ($t=3$ ms); (d) Increasing of TiO density ($t=6$ ms); (e) Formation of high TiO density region ($t=9$ ms); (f) Transportation of TiO to the downstream of the PMITP torch ($t=12$ ms).

References

- [1] Malato S, Blanco J, Alarcon D C, Maldonado M I, Fernandez-Ibanez P, and Gernjak W 2007 Photocatalytic decontamination and disinfection of water with solar collectors *Catalysis Today* **122** pp. 137–49
- [2] Li J, Zhao X, Wei H, Gu Z Z, and Lu Z 2008 Macroporous ordered titanium dioxide (TiO₂) inverse opal as a new label-free immunosensor. *Analytica Chimica Acta* **625** pp. 63–9
- [3] Gratzel M 2001 Photoelectrochemical cells. *Nature* **414** pp. 338–44
- [4] Biju K P and Jain M K 2008 Effect of crystallization on humidity sensing properties of sol-gel derived nanocrystalline TiO₂ thin films. *Thin Solid Films* **516** pp. 2175–80
- [5] Tsai Y C, Hsi C H, Bai H, Fan S K and Sun D H 2012 Single-step synthesis of Al-doped TiO₂ nanoparticles using non-transferred thermal plasma torch. *Jpn. J. Appl. Phys.* **51** 01AL01
- [6] Lee K N, Kim Y, Lee C W and Jai-Sung Lee J S 2011 Simultaneous amination of TiO₂ nanoparticles in the gas phase synthesis for bio-medical applications *Mater. Sci. Eng.* **18** 082021
- [7] Mio M, Kogoma M, Fukui H, and Takeda A 2010 Control of inflammation using adsorption of inflammatory by nano-particles *Chem. Eng.* **55** pp. 603-8 (in Japanese)
- [8] Girshick S L, Chiu C P, Munro R, Wu C Y, Yang L, Singh S K, and McMurry P H 1993 Thermal plasma synthesis of ultrafine iron particles. *J. Aerosol Sci.* **24** pp. 367–82
- [9] Oh S M and Ishigaki T 2004 Preparation of pure rutile and anatase TiO₂ nanopowders using RF thermal plasma. *Thin Solid Films* **457** pp. 186–91

-
- [10] Tong L and Reddy R G 2006 Thermal plasma synthesis of SiC nano-powders/nano-fibers. *Materials Research Bulletin* **41** pp. 2303–10
- [11] Li J G, Ikeda M, Ye R, Moriyoshi Y, and Ishigaki T 2007 Control of particle size and phase formation of TiO₂ nanoparticles synthesized in RF induction plasma. *J. Phys. D: Appl. Phys.* **40** pp. 2348–53
- [12] Ishigaki T and Li J G 2007 Synthesis of functional nanocrystallites through reactive thermal plasma processing. *Sci. and Technol. Advanced Mater.* **8** pp. 617–23
- [13] Tanaka Y, Tsuke T, Guo W, Uesugi Y, Ishijima T, Watanabe S, and Nakamura K 2012 A large amount synthesis of nanopowder using modulated induction thermal plasmas synchronized with intermittent feeding of raw materials. *J. Phys. D: Conf. Ser.* **406** 012001
- [14] Kodama N, Kita K, Tanaka Y, Uesugi Y, Ishijima T, Watanabe S, and Nakamura K 2014 A method for large-scale synthesis of Al-doped TiO₂ nanopowder using pulse-modulated induction thermal plasmas with time-controlled feedstock feeding. *J. Phys. D: Appl. Phys.* **47** 195304
- [15] Tsuke T, Guo W, Tanaka Y, Uesugi Y, Ishijima T, Sakai Y, and Nakamura K 2012 The paper of Technical Meeting on Plasma Sci. & Technolo. IEE of Japan, PST-10-122

Chapter 5

Spatial estimation of Ti excitation temperature in the ICTP torch during TiO₂ nanopowder synthesis

5.1 Introduction

Nanopowders and nanoparticles (NPs) are receiving great attention as next-generation materials because of their unique physical, chemical, and optical properties compared to their bulk properties. Therefore, NPs are used in diverse fields: electronics, medicine, energy, and the environment. For example, titanium dioxide nanoparticles (TiO₂ NPs) is used as a photocatalyst [1], and in photonic crystals [2], photovoltaic cells [3], and gas sensors [4]. In addition, metallic-ion doped TiO₂ NPs are anticipated for use as visible light-active photocatalysts [5]– [7], and as biomedical materials for inflammatory protein adsorption [8,9]. Especially for biomedical applications, prevention of contamination in NPs is extremely important because even slight impurities of countable atoms or molecules can alter the NP properties and damage human skin. Therefore, a high-purity synthesis process of NPs with high production efficiency is eagerly sought for progress of nano-technologies.

Various NP synthesis methods have been developed to date. Different thermal plasma torches have been applied in these methods to fabricate nanomaterials including NPs [1]. Among these NP synthesis methods using thermal plasmas, inductively coupled thermal plasma (ICTP) presents some great benefits for NP fabrication [2]– [18]. One salient benefit of ICTP methods is that ICTP can produce a high-temperature and high-chemical activity field with no impurity from electrodes. In actuality, it requires no electrodes to sustain

thermal plasmas. A second important benefit is that the ICTP method can use not only liquid and gas materials but also solid materials as a feedstock material. This feature extends its applicable range for NPs of various types. Another feature is that it can offer one-step, direct processing with much shorter processing time for NP synthesis. The ICTP method can evaporate the feedstock fed to produce atoms in the high-temperature ICTP. Then the evaporated material is cooled to produce NPs. This method can also produce not only pure-metallic NPs but also oxide or nitride NPs by adopting specified reactive gases for processing. Nevertheless, the conventional ICTP method also presents some shortcomings, including poor size control and low production efficiency. Therefore, the alleviation of these shortcomings suggests challenging work for the goal of wider use of ICTP methods in future applications.

The authors have developed a unique and original method of large-scale NP synthesis using pulse-modulated induction thermal plasma (PMITP) with time-controlled feeding of a feedstock (TCFF) [19]–[22]. We designate this method as ‘PMITP+TCFF method’. The PMITP was developed in our group to control the high-temperature and chemical activity fields in thermal plasmas in the time domain using amplitude modulation of the coil-current [23, 24]. In addition, we contrived the TCFF method for more effective NP fabrication. The TCFF method was applied to control timing of the feedstock injection into the ICTP torch. In the PMITP+TCFF method, feedstock powder is intermittently injected synchronously with coil-current modulation of PMITP [21, 22]. This PMITP+TCFF method provides effective evaporation of feedstock. Then effective cooling of the evaporated materials is done for efficient nucleation of NPs. In the chapter 2, the 20 kW PMITP+TCFF method was adopted for pure-TiO₂ NPs and Al³⁺-doped TiO₂ NP syntheses. In this work, pure-TiO₂ NPs with mean particle diameter of approximately 43 nm and Al³⁺-doped TiO₂ NPs with mean particle diameter of approximately 67 nm were synthesized with a high production rate of more than approximately 400–500 g h⁻¹ [7, 26]. These production rates at input power of 20 kW were several tens of times higher than those of conventional methods using thermal plasmas.

One key point for enhancement of production efficiency is to elucidate NP formation mechanisms including feedstock evaporation processes and precursor molecule formation processes. For this purpose, many numerical simulations have been conducted for various

kinds of NP synthesis using an ICTP torch to clarify NP formation processes including feedstock evaporation, precursor formation, nucleation and NP growth processes [17]– [20]. However, few reports have described investigation of NP synthesis processes based on spatial and temporal measurements for the ICTP torch during NP synthesis.

We have been investigating these processes during pure-TiO₂ NP synthesis using the ICTP mainly with a two-dimensional optical emission spectroscopic (2D OES) system. In the chapter 3 and chapter 4, the 2D OES measurement was carried out to fundamentally investigate Ti feedstock evaporation and precursor TiO formation processes in ICTP and PMITP torch and to discuss effect of PMITP+TCFF method on feedstock evaporation and precursor formation [30,31]. However, the temperature distribution in the ICTP torch has not yet been investigated. The temperature is a crucial parameter for determining NP nucleation processes.

This chapter presents estimation results on 2D temperature distribution in the plasma torch during TiO₂ nanopowder synthesis. Almost single-shot feedstock powder injection was applied to the non-modulated ICTP torch in this experiment. For this estimation, the Ti excitation temperature $T_{\text{ex}}^{\text{Ti}}$ distribution was estimated using the two-line method for two Ti I atomic spectral lines. The spatial and temporal change in the $T_{\text{ex}}^{\text{Ti}}$ was evaluated in the plasma torch during TiO₂ NP synthesis. Evaluated $T_{\text{ex}}^{\text{Ti}}$ was compared with spatiotemporal distribution of TiO radiation intensities obtained from our earlier work [31]. Result showed that the Ti excitation temperature is higher at off-axis region in the ICTP torch, while it is lower at central axis region with strong TiO radiation intensity. These results suggest that TiO molecules are formed only at lower temperature region around central axis region in the ICTP torch.

5.2 Experimentals

5.2.1 Experimental setup

The experimental setup was the same as that reported in our earlier work [26]. Figure 5.1 shows the non-modulated ICTP torch for TiO₂ nanopowder synthesis. This cylindrical-type of ICTP torch has two co-axial quartz tubes. The water flows between quartz tubes to cool the inner quartz tube wall. The inner quartz has 70 mm inner diameter and 370 mm length;

the outer quartz tube has 85 mm outer diameter. The eight-turn induction coil is located around the outer quartz tube. The coil is connected to a matching circuit and inverter power supply to generate an electromagnetic field. Consequently an RF thermal plasma is produced inside the inner quartz tube of the plasma torch. A water-cooled stainless steel feeding tube is inserted from the top of the torch head, located on the central axis of the torch. The outer diameter and inner diameter of the feeding tube are, respectively, 10 mm and 4 mm. The feedstock can be injected directly into the thermal plasma through the feeding tube from a powder feeder. Between the feeding tube and the powder feeder, a high-speed solenoid valve is installed to control feedstock injection into the thermal plasmas. This solenoid valve can be controlled using a transistor–transistor logic (TTL) signal. Figure 5.2 depicts an overall view of the experimental system for nanoparticles synthesis, including the ICTP torch, reaction chambers, a collection filter, and a vacuum pump. The reaction chambers and the collection filter are installed downstream of the ICTP torch to collect the synthesized nanopowder. All reaction chamber walls are cooled by water. Details of these experimental apparatuses are available in the literature [26].

5.2.2 Experimental conditions

Table 6.1 presents the experimental conditions of pure-TiO₂ nanopowder synthesis described in the present work. In this experiment, the Ti feedstock was intermittently injected into the non-modulated PMITP torch (i.e. conventional ICTP torch) to investigate the spatiotemporal behaviours of Ti feedstock vapour and precursor TiO vapour, and also the temperature and nucleation inside the ICTP torch. The time-averaged input power from the inverter power supply was fixed at 20 kW. The fundamental frequency of the coil-current was about 304 kHz. A mixture gas of Ar and O₂ was used as a sheath gas. The total gas flow rate of the sheath gas was fixed at 100 L min⁻¹. The gas composition was set to 90 mol%Ar and 10 mol%O₂. In this experiment, to retain simplicity of the investigation, quenching gas was not supplied to the reaction chamber. The pressure was fixed at 300 Torr (approx. 40 kPa) for the inside of torch and reaction chamber. Pure-Ti micro-powder (TILOP-45; Osaka Titanium Technologies Co. Ltd.) was used as the feedstock powder. The mean diameter and the maximum diameter of this feedstock were about 27 μm and 45 μm, respectively. The Ti feedstock was intermittently supplied into the ICTP torch with

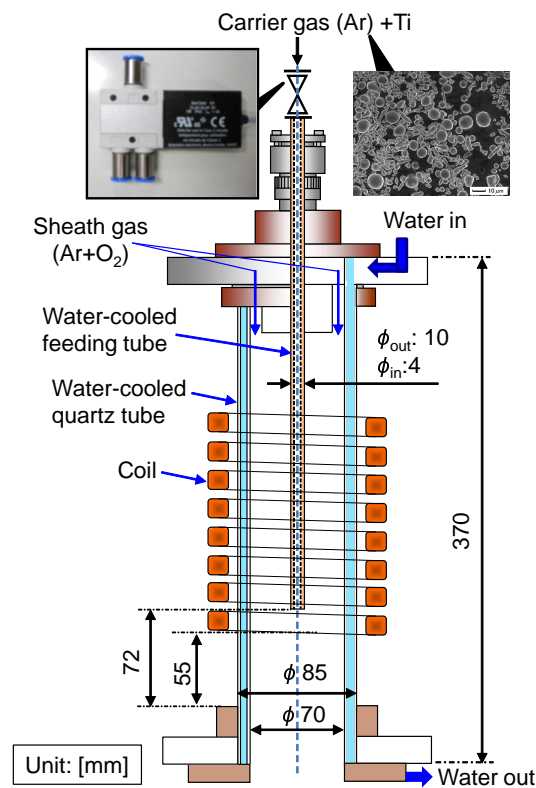


Fig. 5.1: Experimental apparatus using an ICTP torch and solenoid valve.

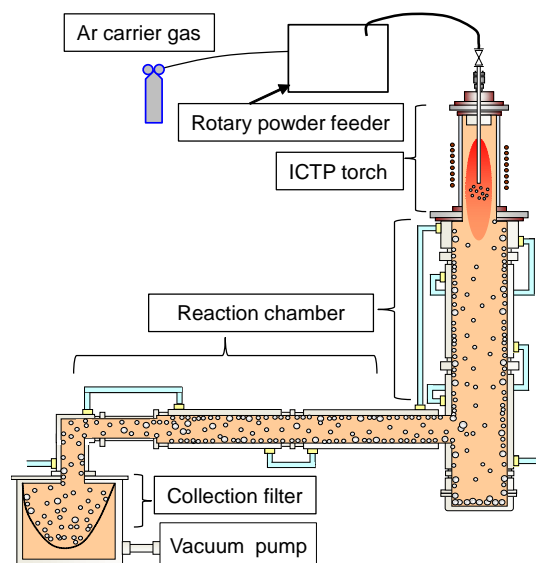


Fig. 5.2: Overall view of the experimental apparatus used for nanopowder fabrication.

Table 5.1: Experimental conditions.

Time-averaged input power	20 kW
Fundamental frequency of the coil current	304 kHz
Modulation	Non-modulation
Pressure	300 Torr (~ 40 kPa)
Gas composition	Ar: 90 L min ⁻¹ , O ₂ : 10 L min ⁻¹
Carrier gas flow rate	Ar: 4 L min ⁻¹
Quenching gas	Non-injection
Valve open–close cycle	30 ms
Valve open–close time	8/22 ms (27%DF _{valve})
Powder feed rate g_{pow}	4–7 g min ⁻¹
Feedstock	100 wt%Ti powder $\bar{d} = 27 \mu\text{m}$, $d < 45 \mu\text{m}$

Ar carrier gas through the solenoid valve and feeding tube. The gas flow rate of Ar carrier gas was fixed at 4 L min⁻¹. The feedstock injection was controlled by a high-speed solenoid valve connecting the feeding tube with the rotary powder feeder, as shown in Figure 5.2. The solenoid valve response time was about 2 ms. The feedstock feeding rate was adjusted to about 4–7 g min⁻¹. This feeding rate is lower than those used for large-scale nanopowder synthesis reported in our earlier work [26], but it is higher or comparable to that of the conventional ICTP method. This feeding rate condition was selected to investigate fundamental behaviour of the feedstock vapour, precursor TiO vapour, the temperature distribution and nucleation. The feeding cycle time ($t_{\text{valve}}^{\text{cyc}}$) was set to 30 ms, which is much longer than that used in our earlier work [26]. The open (t_{open})/close time (t_{close}) of the solenoid valve was adjusted to 8/22 ms (27%DF_{valve}). The DF_{valve}, which was used as a control parameter of the solenoid valve, is defined as $t_{\text{open}}/t_{\text{valve}}^{\text{cyc}}$. In the condition of 27%DF_{valve}, the open time was sufficiently shorter than the close time. Therefore the condition of 27%DF_{valve} is regarded as almost a single-shot feedstock feeding. This single-shot feeding was adopted to avoid interaction between feedstock feeding during intermittent feedstock injection [31].

Table 5.2: Two-dimensional spectroscopic observation conditions.

Observation area	$47 \times 46 \text{ mm}^2$ region below the coil end
Diffraction grating	1200 grooves/mm
Wavelength resolution	0.4 nm
Spectral lines observed	Ti I (453.32 nm) and Ti I (521.04 nm)
Frame rate for high speed video camera	3000 fps

5.2.3 Optical emission spectroscopy conditions

The 2D OES measurements were conducted using a 2D OES system (AN-IMC-DD; Anfi Inc.) as presented in figure 5.3 with a 2D OES region. This 2D OES system consists of an objective lens (AF Zoom-Nikkor 80-200 mm f/2.8D ED; Nikon Corp.), an imaging spectrometer (Acton Spectra Pro 2300i; Princeton Instruments, Inc.), and a high-speed video camera (GX-8; NAC Image Technology Inc.). The observation conditions are presented in table 6.2. The 2D OES region was set to approximately a $47 \times 46 \text{ mm}^2$ region below the coil-end, as shown in figure 5.3. The imaging spectrometer has a diffraction grating of 1200 grooves mm^{-1} . The wavelength resolution of this system was 0.4 nm. The salient feature of this system is that it can measure the radiation intensity of spectral lines with higher wavelength resolution of 0.4 nm than those other imaging OES systems using optical interference bandpass filters. In this work, two Ti I spectral lines were observed at 453.32 nm and 521.04 nm wavelengths to estimate Ti excitation temperature distribution using two-line method. A high-speed video camera was used to capture 2D image at the specified wavelength. The frame rate of the high-speed video camera was set to 3000 frames per second (fps). We confirmed that the measured high-speed video images had good reproducibility at each timing in the present experimental condition. Consequently, the accumulation and averaging were done four times for four cycles ($=4t_{\text{valve}}^{\text{cyc}}$) to reduce the contribution from a noise signal.

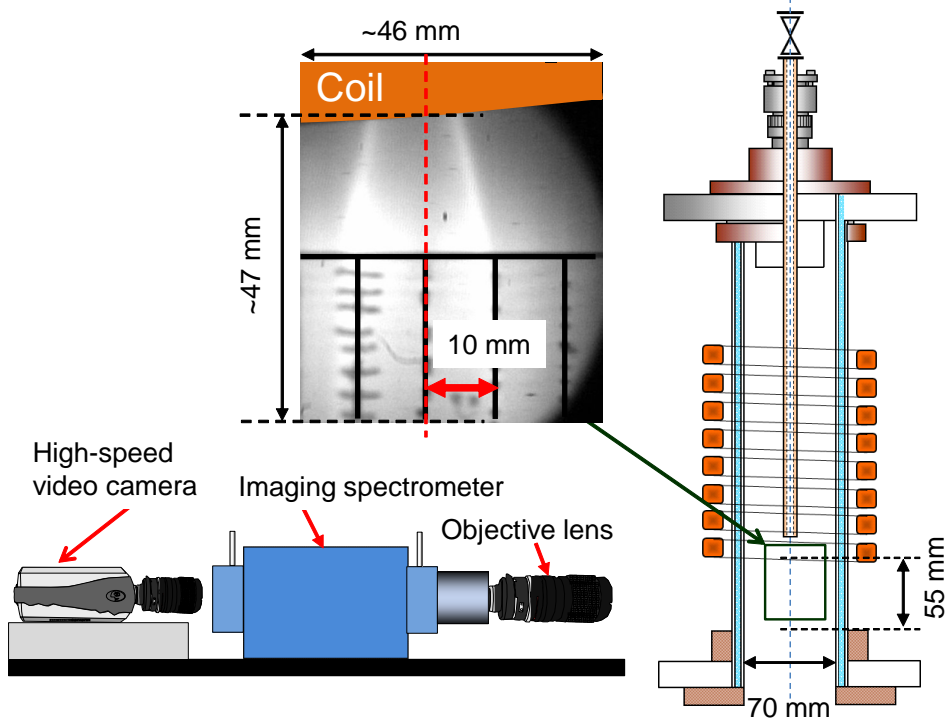


Fig. 5.3: Two-dimensional spectroscopic observation region and observation system using an imaging spectrometer and high-speed video camera.

5.3 Determination method of Ti excitation temperature

The Ti excitation temperature ($T_{\text{ex}}^{\text{Ti}}$) was ascertained from 2D radiation intensity of Ti I at 453.32 nm and that of Ti I at 521.04 nm. Here, the radiation intensity I_{453} of Ti I spectral line at 453.32 nm is superimposed from the contribution of two Ti I spectral lines at 453.3240 nm and at 453.4776 nm, whereas the radiation intensity I_{521} is obtained from a Ti I spectral line at 521.04 nm. Consequently, the intensity ratio I_{453}/I_{521} can be calculated as a function of $T_{\text{ex}}^{\text{Ti}}$ when the population of the excited states follows the Boltzmann distribution at the excitation temperature $T_{\text{ex}}^{\text{Ti}}$:

$$\frac{I_{453}}{I_{521}} = \frac{\frac{g_p A_{pq}}{\lambda_{pq}} \exp\left(-\frac{E_p}{kT_{\text{ex}}^{\text{Ti}}}\right) + \frac{g_k A_{kl}}{\lambda_{kl}} \exp\left(-\frac{E_k}{kT_{\text{ex}}^{\text{Ti}}}\right)}{\frac{g_m A_{mn}}{\lambda_{mn}} \exp\left(-\frac{E_m}{kT_{\text{ex}}^{\text{Ti}}}\right)} \quad (5.1)$$

where k is Boltzmann's constant, λ_{pq} , λ_{kl} and λ_{mn} are wavelengths for Ti I at 453.3240 nm, at 453.4776 nm and at 521.0384 nm, g_p , g_k and g_m are the degeneracy values of the

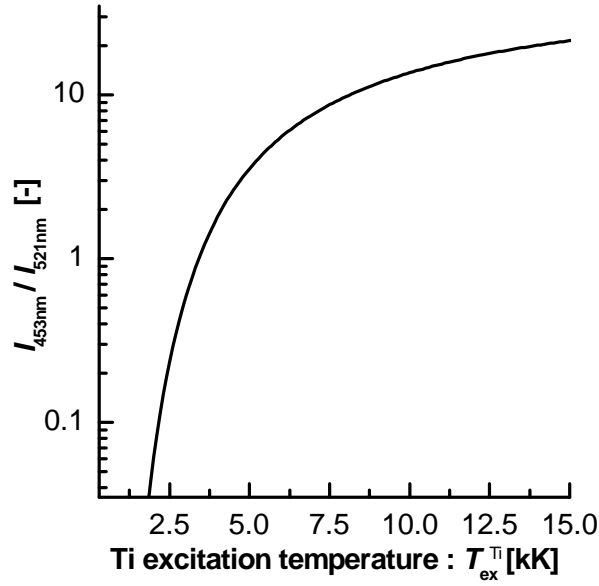
upper level for respective spectral lines, A_{pq} , A_{kl} and A_{mn} are the transition probabilities for respective spectral lines, E_p , E_k and E_m is the upper state energy levels for respective spectral lines. These atomic constants, which were referred from the NIST database [27], are presented in table 5.3.

As well known, the collision frequencies between the electron and heavy particles and between heavy particles are extremely high (e.g. $\sim 10^{16} \text{ s}^{-1}$ at 300 torr) in thermal plasmas because the electron and gas temperatures are high as several thousands kelvin and the pressure is high as 300 torr. These high collision frequencies lead the plasma to near thermodynamic equilibrium condition. Thus, the population of the excited states follows the Boltzmann distribution in many case for thermal plasmas [13]. From this reason, it was assumed at present that the population of the excited states follows the Boltzmann distribution.

Figure 5.4 shows a curve of I_{453}/I_{521} as a function of $T_{\text{ex}}^{\text{Ti}}$. Using this curve of $I_{453}/I_{521} - T_{\text{ex}}^{\text{Ti}}$, one can estimate $T_{\text{ex}}^{\text{Ti}}$ from measurements of I_{453}/I_{521} for intensity ratio of the Ti I spectral lines. For this temperature estimation, the influence of continuum spectra was found to be negligible because the radiation intensity of continuum spectra around 521.04 nm and 453.32 nm wavelengths were very weak compared with those of these Ti I spectra lines. This neglect of the continuum was confirmed from another spectroscopic observation using a spectroscopic observation. In determination of the excitation temperature, for simplicity, Abel inversion was not performed. Strictly speaking, Abel inversion for the measured radiation intensities should be done to obtain the net radiation intensity distributions if the axis-symmetric structure can hold in the radiation intensity. However, the complete axis-symmetric structure cannot be obtained in the measured radiation intensity, and the incomplete axis-symmetric structure would involve an error in the estimation of temperature. On the other hand, the apparent radiation intensities integrated along the line of sight were used here to determine the excitation temperature with an error tolerance. The excitation temperature determined here is thus not completely local one but an indicator of the excitation temperature. Nevertheless, the excitation temperature determined here is roughly close to the real excitation temperature, and useful to estimate relative distribution of the excitation temperature. Consequently, the excitation temperature ascertained in this study would be overestimated or underestimated with error of $\pm 1000 \text{ K}$ from our

Table 5.3: Physical quantities for respective Ti I spectra.

λ [nm]	Config.	E [eV]	A [$\times 10^6$ s $^{-1}$]	g
453.3204	3d ³ 4s-3d ³ 4p	3.5827	88.3	11
453.4776	3d ³ 4s-3d ³ 4p	3.5693	68.7	9
521.0384	3d ² 4s ² -3d ² 4s4p	2.4269	3.89	9

Fig. 5.4: Relation between I_{453}/I_{521} and the Ti excitation temperature.

detailed temperature evaluation considering the radial temperature distribution. The error in temperature determination between with and without Abel inversion will be discussed in section 5.5.2.

5.4 Two-dimensional spectroscopic observation results

5.4.1 Spatial distribution of Ti I radiation intensities

Figure 5.5 portrays 2D OES results for two Ti atomic lines. Panel (a) shows the solenoid valve open–close signal, panel (b) depicts a schematic of the estimated timing of feedstock injection into the ICTP torch, and panel (c) is the 2D distribution of Ti I radiation intensity at 453.32 nm wavelength, and panel (d) portrays the 2D distribution of Ti I radiation

intensity at 521.04 nm wavelength. Panel (a) presents that the solenoid valve receives the open signal (high-level signal) at $t=0$ ms, and the close signal (low-level signal) at $t=8$ ms, where t is the time. As portrayed in panel (b), we have already confirmed in another experiment that it takes approximately 6–8 ms for the solenoid valve to open and for Ti feedstock to travel from the inlet of the solenoid valve to the ICTP torch. After the feedstock reaches the torch at around $t=8$ –9 ms, and the feeding rate becomes the value in the steady state at $t=9$ –16 ms. After steady state feeding, the feeding rate decreases and stops at around $t=15$ –17 ms. In panels (c) and (d), the coil end position is presented with axial coordinate z and radial coordinate r . The radial position $r=0$ mm in panels (c) and (d) almost corresponds to the central axis of the ICTP torch.

In panel (c), the radiation intensity of Ti I at 453.32 nm was extremely low at $t=0$ –6 ms because the Ti feedstock did not yet reach into the ICTP torch. At $t=6$ –8 ms, the Ti I radiation intensity increased sharply. This sharp increase in the radiation intensity indicates that Ti feedstock reaches the torch. It began to be evaporated rapidly at around $t=6$ ms. It is noteworthy that, around $t=6$ ms, the Ti I radiation intensity was detected only around the on-axis region ($r=0$ mm), although it was then expanded from the on-axis region to the off-axis region at $t=8$ ms. This expansion suggests that the feedstock evaporation initially occurs around on-axis region. Then the evaporated Ti atoms might be diffused in the radial direction because of the high radial gradient of Ti density. At $t=8$ –20 ms, the Ti I radiation intensity is kept high and static at the axial position of $z=15$ –40 mm and radial position of $|r| < 10$ mm below the coil-end region in the ICTP torch. This high and static radiation intensity distribution implies that the feedstock injection and its evaporation are almost in a steady state in the ICTP torch. After $t=20$ –22 ms, the Ti I radiation intensity decreased with time. Then it became too low to be detected. This result reflects that feedstock feeding is well controlled to be stopped by the solenoid valve. Similar spatiotemporal behaviour of Ti I radiation intensity was found for the spectral line at 521.04 nm wavelength, as shown in panel (d). Consequently, spatiotemporal distributions of the radiation intensities from two Ti atomic lines were observed using the 2D OES system.

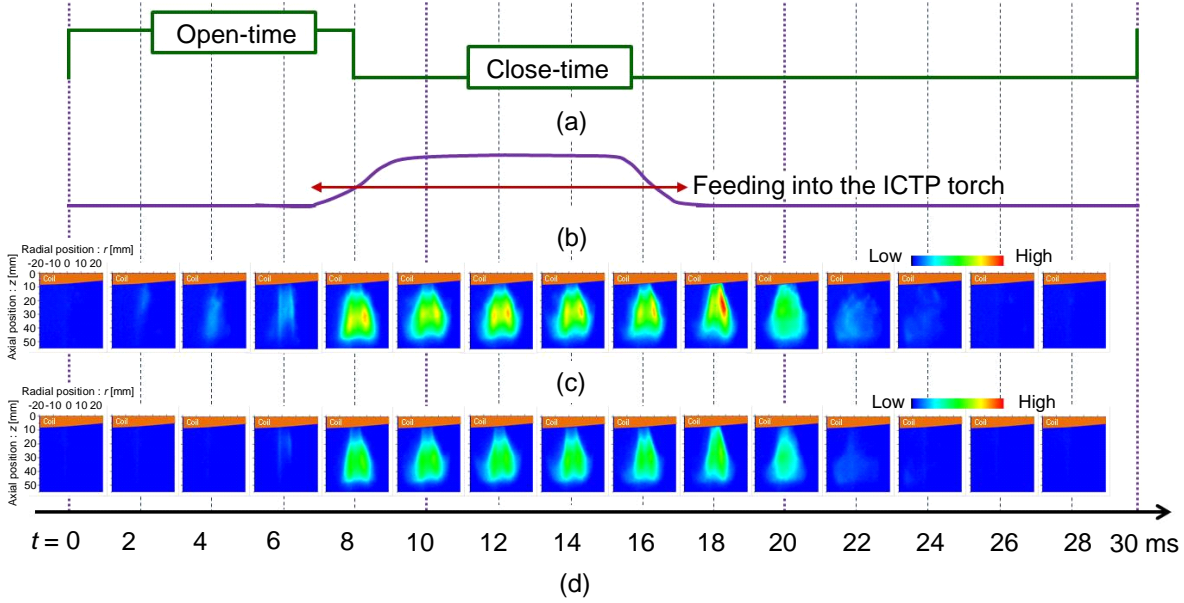


Fig. 5.5: 2D OES results for two Ti atomic lines. (a) High-speed solenoid valve open–close signal. (b) Estimated actual feedstock injection timing into the ICTP torch. (c) Ti I radiation intensity at 453.32 nm wavelength. (d) Ti I radiation intensity at 521.04 nm wavelength.

5.4.2 Spatiotemporal distribution of the Ti excitation temperature

5.4.2.1 Estimation of 2D Ti excitation temperature

The excitation temperature $T_{\text{ex}}^{\text{Ti}}$ was estimated from the radiation intensities of the two Ti I lines. Figure 5.6 depicts (a) the radiation intensity distribution of Ti I at $\lambda=453.32$ nm, (b) that at $\lambda=521.04$ nm, and (c) $T_{\text{ex}}^{\text{Ti}}$ estimated from the above two intensity distributions at $t=16$ ms. In panel (c), the region painted in black corresponds to the region in which $T_{\text{ex}}^{\text{Ti}}$ was unable to be estimated because of its low radiation intensity. In addition, the region in which $T_{\text{ex}}^{\text{Ti}}$ was estimated as below 2500 K is also painted in black because of a lack of accuracy in determination of $T_{\text{ex}}^{\text{Ti}}$.

In this figure, $T_{\text{ex}}^{\text{Ti}}$ on the axis around $|r| < 10$ mm was estimated as about 2500–4000 K, which is lower than the off-axis temperature. This low temperature might arise from a quenching effect of low-temperature Ar carrier gas (approx. 300 K) injected together

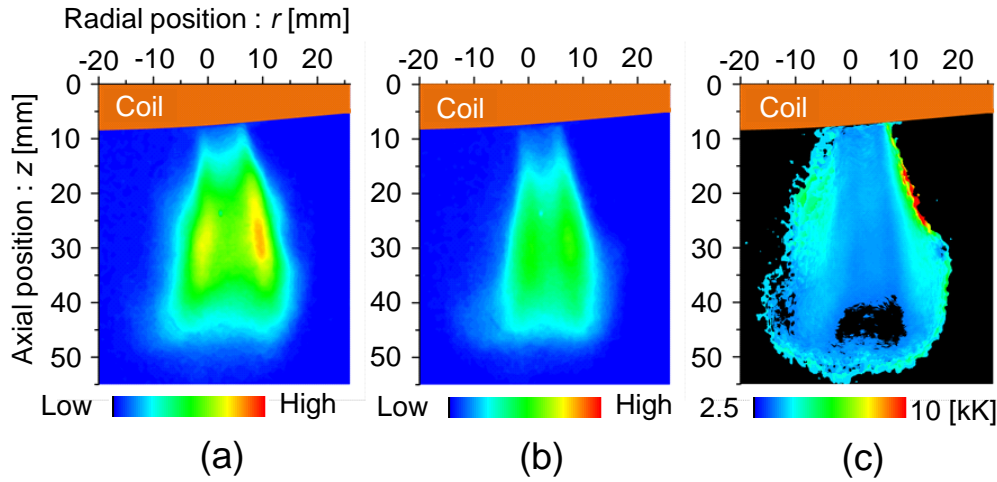


Fig. 5.6: Comparison between Ti I radiation intensities and estimated Ti excitation temperature distribution at $t=16$ ms. (a) Ti I radiation intensity at 453.32 nm wavelength. (b) Ti I radiation intensity at 521.04 nm wavelength. (c) 2D distribution of Ti excitation temperature.

with Ti feedstock into the ICTP torch [31]. Furthermore, evaporation of the Ti feedstock consumes energy around the on-axis, which can decrease the temperature. On the other hand, $T_{\text{ex}}^{\text{Ti}}$ around $|r|=10\text{--}15$ mm, which is the off-axis temperature, was estimated as higher than 4500 K. This high temperature at the off-axis might be attributable to induction heating by the eddy current in the ICTP. The injected Ti feedstock is evaporated, resulting in high-density Ti atoms. Mixing of Ti atoms to Ar-O₂ plasma increases the electrical conductivity markedly around 4500–6000 K [31] because of lower ionization potential of Ti than Ar or O atoms. Consequently, at the off-axis region, the current density from inductive coupling can be elevated by increased electrical conductivity, involving an increase in the on-axis temperature. Such 2D temperature estimation can be done using 2D OES measurements.

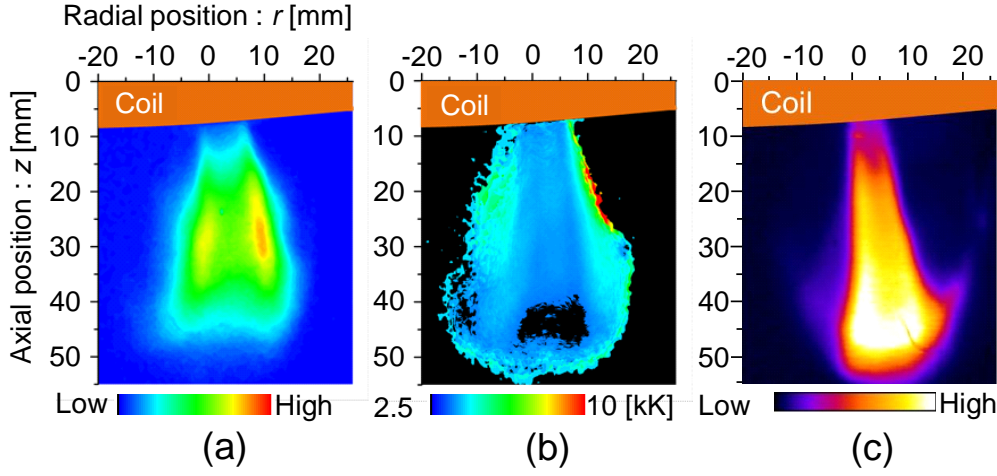


Fig. 5.7: Comparison between Ti I and TiO radiation intensities and estimated Ti excitation temperature distribution at $t=16$ ms. (a) Ti I radiation intensity at 453.32 nm wavelength. (b) 2D distribution of Ti excitation temperature. (c) TiO radiation intensity obtained from our earlier work [31].

5.4.2.2 Relation between estimated $T_{\text{ex}}^{\text{Ti}}$ and the radiation intensities of Ti and TiO

It is useful to investigate the relation between the estimated $T_{\text{ex}}^{\text{Ti}}$ and the radiation intensities of Ti and TiO. Figure 5.7 presents a comparison of spatial distributions among (a) the radiation intensity of Ti atomic line at 453.32 nm, (b) estimated $T_{\text{ex}}^{\text{Ti}}$, and (c) the radiation intensity of TiO. These are obtained at $t=16$ ms after initiation of the open signal for the solenoid valve, as described in the previous section. The TiO molecular radiation intensity distribution was referred from our earlier work [31]. From the radiation intensity distributions of Ti and TiO shown in panels (a) and (c), we were able to infer the density distribution of Ti and TiO, while also considering the temperature in panel (b).

As shown in panel (a), the Ti atoms have high density around the axis just below the coil end, where $T_{\text{ex}}^{\text{Ti}}$ was estimated as 2500–4000 K around the axis in panel (b), as described in the previous section. Panel (c) depicts that the TiO radiation intensity is high only around on-axis region. This strong TiO radiation intensity distribution on the axis closely corresponds to low- $T_{\text{ex}}^{\text{Ti}}$ region around on-axis shown in panel (b). In addition, the

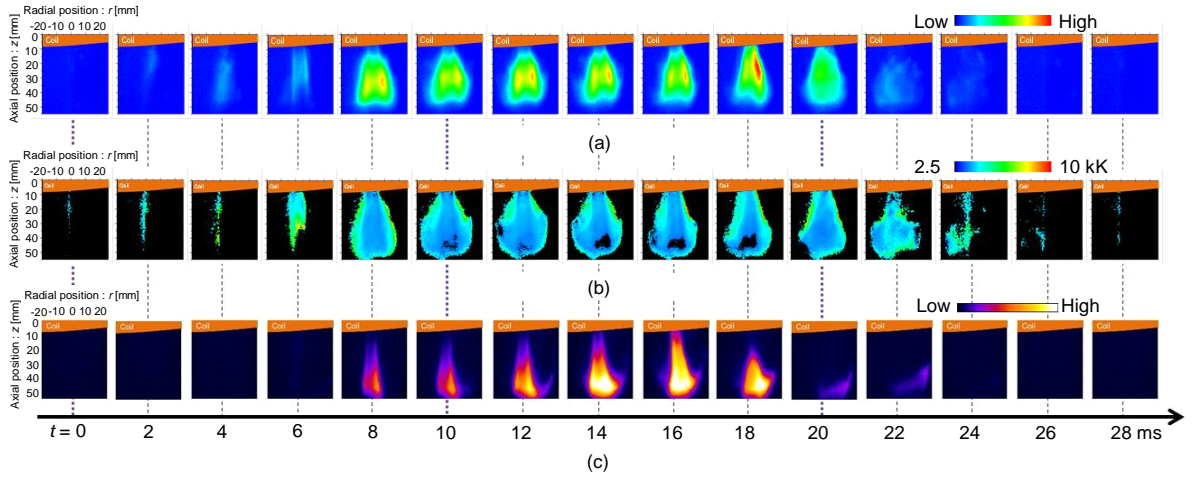


Fig. 5.8: Comparison between 2D OES results and estimated Ti excitation temperature distribution. (a) Ti I radiation intensity at 453.32 nm wavelength. (b) 2D distribution of Ti excitation temperature. (c) TiO radiation intensity obtained from our earlier work [31].

TiO radiation intensity became highest downstream of the torch. This downstream region approximates the region in which $T_{\text{ex}}^{\text{Ti}}$ was estimated below 2500 K. This agreement suggests that TiO molecules are formed this downstream region because of association reactions $\text{Ti} + \text{O} + \text{M} \rightarrow \text{TiO} + \text{M}$ at low temperature, where M is the third particle.

5.4.2.3 Spatiotemporal distribution of Ti excitation temperature

For one cycle of the valve open to close, the $T_{\text{ex}}^{\text{Ti}}$ was estimated. Its spatiotemporal distribution was compared with the radiation intensity distribution of Ti and TiO. Figure 5.8 shows the spatiotemporal distributions of (a) the Ti I radiation intensity, (b) the estimated $T_{\text{ex}}^{\text{Ti}}$, and (c) the TiO radiation intensity in one cycle of the solenoid valve for intermittent feeding.

As panel (b) shows, $T_{\text{ex}}^{\text{Ti}}$ was not estimated between $t=0-4$ ms because the Ti radiation intensity was extremely low in the ICTP torch. At $t=6-8$ ms, $T_{\text{ex}}^{\text{Ti}}$ was estimated as 2500–4000 K around on the axis, as 4500–8000 K in off-axis region in the ICTP torch. At $t=8-18$ ms, $T_{\text{ex}}^{\text{Ti}}$ distribution is almost static, except at a downstream portion. That downstream portion has a decreased temperature region around $z=40-50$ mm and $|r|=10$ mm. The radiation intensity of TiO becomes strong, as shown in panel (c) especially at $t=14-16$

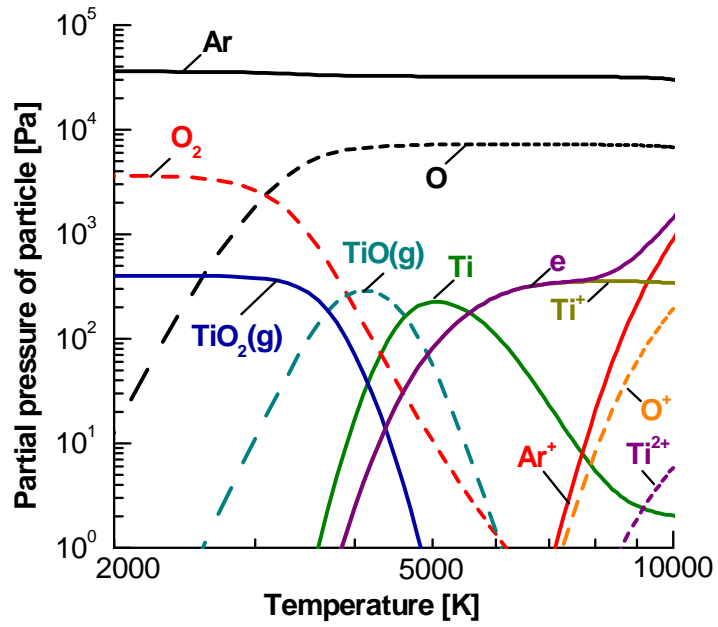
ms. This fact suggests that TiO molecules are formed at this downstream region through an association reaction by decreased temperature. From $t=16$ ms, injection amount of feedstock was gradually reduced by closing the valve, as described previously. This suppression of feedstock injection might engender recovery in the temperature, especially from upstream of the ICTP torch. Consequently, $T_{\text{ex}}^{\text{Ti}}$ was found to be recovered gradually after $t=16$ ms, as shown in panel (b). In panel (c), the TiO radiation intensity was detected strongly at $t=8-18$ ms. This intensity was detected as high only around the on-axis region during $t=8-18$ ms. After $t=18$ ms, the TiO radiation intensity decreased rapidly because TiO molecules might mainly be transported by axial convection and because TiO can be dissociated to produce $\text{Ti} + \text{O}$ by recovering temperature.

5.5 Discussion

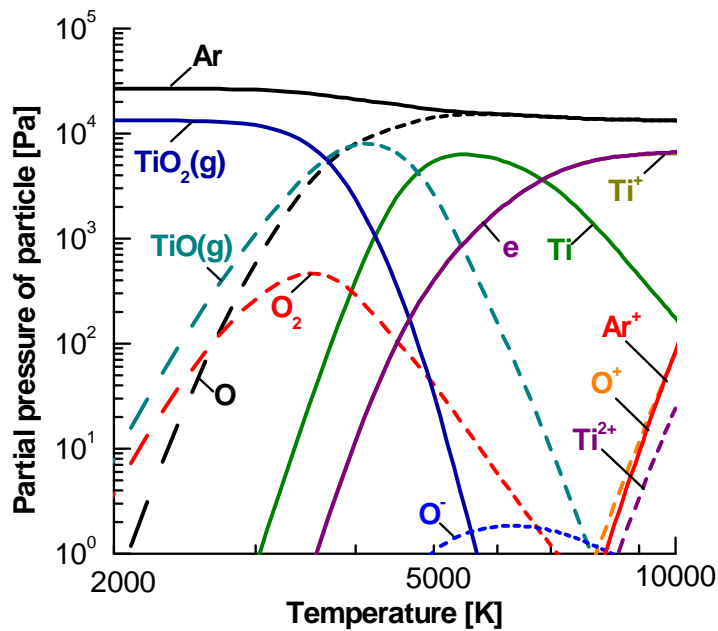
5.5.1 Equilibrium particle composition for the Ar-O-Ti system

The equilibrium particle composition for the Ar-O-Ti system was calculated to investigate behaviour of Ti atoms, and TiO and TiO_2 molecules as a function of temperature. The minimization of Gibbs's free energy of a system of Ar-O-Ti was performed to calculate the equilibrium particle compositions. These calculations were conducted under constant pressure of 300 Torr (approx. 40 kPa). In this calculation, species only in the gas phase were considered. intentionally because we consider precursor molecule formation at first. The calculation procedure is the same as that used in our earlier work [31]. The equilibrium particle compositions were calculated for two gas mixture conditions: 89 mol%Ar - 10 mol% O_2 - 1 mol%Ti and 50 mol%Ar - 25 mol% O_2 - 25 mol%Ti. Both these conditions have more than 2.0 in molar ratio of oxygen atom to titanium atom, and thus all Ti atoms can react with oxygen atoms to produce TiO_2 molecules through reactions of $\text{Ti}(\text{g}) + \text{O}_2 \rightarrow \text{TiO}_2(\text{g})$. The second condition of 50%Ar-25% O_2 -25%Ti mixture has a much higher Ti inclusion ratio. Therefore, high density TiO and TiO_2 vapour can be formed compared to the first condition of 89%Ar-10% O_2 -1%Ti mixture.

Figures 5.9 (a) and (b) present the calculated equilibrium compositions of 89%Ar-10% O_2 -1%Ti and 50%Ar-25% O_2 -25%Ti mixtures at a pressure of 300 torr (~ 40 kPa). In panel (a) for 89%Ar-10% O_2 -1%Ti mixture, particles of all kinds are ionized at temperatures higher



(a)



(b)

Fig. 5.9: Equilibrium particle compositions for the Ar-O₂-Ti system: (a) 89%Ar-10%O₂-1%Ti, and (b) 50%Ar-25%O₂-25%Ti.

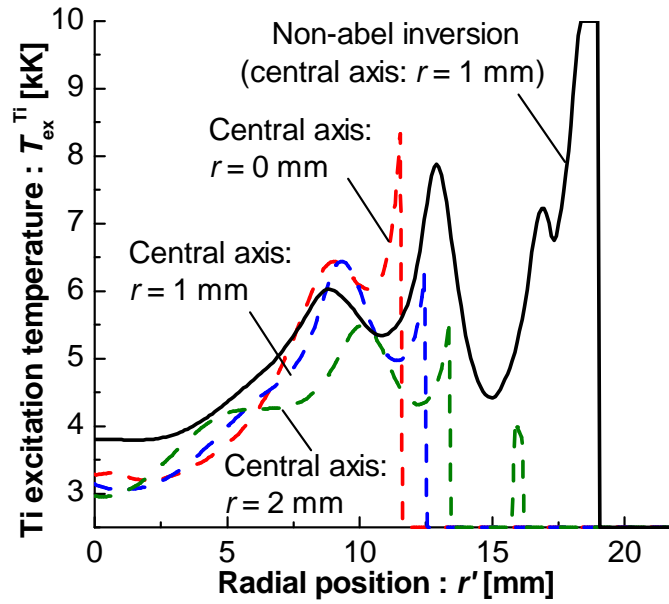


Fig. 5.10: Estimation result of Ti excitation temperature with Abel inversion at $z=20$ mm.

than 10 000 K. At temperatures of 10 000 – 5000 K, Ar and O atoms are the predominant species. At 5000–3000 K, TiO(g) is formed by the association reaction of $\text{Ti(g)} + \text{O} \rightarrow \text{TiO(g)}$. Then TiO(g) becomes a dominant species. At temperatures below 3000 K, $\text{TiO}_2(\text{g})$ in gas phase is also formed markedly by the association reaction of $\text{TiO(g)} + \text{O} \rightarrow \text{TiO}_2(\text{g})$. In addition, the TiO_2 molecule becomes the dominant species among Ti species at temperatures lower than 3500 K. Panel (b) for 50%Ar-25% O_2 -25%Ti mixture shows a similar composition variation as a function of temperature to the 89%Ar-10% O_2 -1%Ti mixture. However, the partial pressure of $\text{TiO}_2(\text{g})$ monomer becomes much higher for the 50%Ar-25% O_2 -25%Ti mixture than for 89%Ar-10% O_2 -1%Ti at temperatures below 4000 K. If such a high partial pressure of $\text{TiO}_2(\text{g})$ can be realized, then it may lead to $\text{TiO}_2(\text{s},\ell)$ nucleation possible in the ICTP torch. On the other hand, O_2 partial pressure becomes lower because O atoms are consumed through formation of $\text{TiO}_2(\text{g})$ and TiO(g) .

In our previous section, we discussed the relationship between the Ti excitation temperature, Ti and TiO radiation intensities. Results from figures 5.7 and 5.8 indicated that TiO(g) was effectively formed in a region at temperatures below 5000 K. These results fairly agree with the density increase of TiO(g) with decreasing temperature from 5000 K in the equilibrium compositions.

5.5.2 Temperature difference between with and without Abel inversion

Abel inversion technique for obtained radiation intensities was partially used to check a influence in temperature determination between with and without Abel inversion. The Abel inversion was made for the two Ti radiation intensities measured at an axial position of $z=20$ mm in figures 5.6(a) and 5.6(b). Generally, the Abel inversion technique assumes an axis-symmetric structure for the radiation intensity and requires to assign the center axis. However, the radiation intensity distribution from the plasma is not completely axis-symmetric structure. The assignment of the center axis position is therefore one parameter to produce an error in temperature determination.

Figure 5.10 shows the estimation results on the radial distribution of $T_{\text{ex}}^{\text{Ti}}$ with Abel inversion and without Abel inversion. This figure includes three results on $T_{\text{ex}}^{\text{Ti}}$ for three different central axis positions with Abel inversion: $r=0, 1,$ and 2 mm in figures 5.6(a) and 5.6(b). In figure 5.10, the solid black curve shows the estimation result on $T_{\text{ex}}^{\text{Ti}}$ without Abel inversion for the specified center axis position of $r = 1$ mm. The dashed curves indicate the estimation results on $T_{\text{ex}}^{\text{Ti}}$ with Abel inversion for the three different center axis positions $r = 0, 1, 2$ mm. The horizontal axis in this figure corresponds to the radial position r' from the specified center axis. As seen in figure 5.10, $T_{\text{ex}}^{\text{Ti}}$ around the central axis $r' < 3$ mm were estimated to be about 3000–3500 K with Abel inversion for different center axis positions, whilst $T_{\text{ex}}^{\text{Ti}}$ was evaluated as about 3700 K without Abel inversion. At $0\text{mm} < r' < 7\text{mm}$, the temperature differences among these four curves are thus less than 1000 K. On the other hand, at radial positions $r' > 7\text{mm}$, there are large temperature differences among three dashed curves. As seen, Abel inversion with uncertain central axis position produces a serious error >2000 K in temperature determination. From the above error estimation, it was found that the temperature error without Abel inversion around the center axis is less than 1000 K. In addition, even with Abel inversion, uncertain center axis position for incomplete axis-symmetric structure provides an error in temperature determination about 2000 K at $r' > 7$ mm in figures 5.6(c) and 5.7(b). Thus, Abel inversion was not carried out for two-dimensional temperature determination in the present paper. Further accurate 2D temperature determination needs a computer tomographic technique with different observation directions in future work. Nevertheless, the 2D temperature estimation result

presented here offers important information on distribution and its time variation during nanoparticle synthesis.

5.5.3 Possibility in nucleation occurrence in the torch

In this section, just a possibility in nucleation occurrence in the torch is discussed on the basis of saturation vapor pressure and then supersaturation condition. This discussion does not explain complete routes to TiO_2 NP formation, but only a nucleation possibility in the torch. As shown in figure 5.9, there are three Ti-containing species, i.e. Ti atom, $\text{TiO}(\text{g})$ and $\text{TiO}_2(\text{g})$ molecules, in Ar- O_2 -Ti system at temperatures below 3000 K. Molecules $\text{TiO}_2(\text{g})$ plays an important role directly for TiO_2 nucleation. In addition, $\text{TiO}(\text{g})$ molecule may also have an important role for TiO nucleation (e.g., $\alpha\text{-TiO}(\text{s})$, $\beta\text{-TiO}(\text{s})$) and then it oxides to produce $\text{TiO}_x(\text{s})$ ($1 < x < 2$) clusters. However, there are lacks of sufficient physical data about $\text{TiO}(\text{s})$ because it is unstable compared to $\text{TiO}_2(\text{s})$. Thus, we here focused only on a possibility in nucleation occurrence for $\text{TiO}_2(\text{s})$ from $\text{TiO}_2(\text{g})$ in the torch. If we consider other routes to $\text{TiO}_2(\text{s})$ nucleation, the nucleation occurrence possibility in the torch would be further higher.

From the temperature distribution determined in the ICTP torch, we can estimate the 2D distribution of saturation vapor pressure of $\text{TiO}_2(\text{g})$. The saturation vapour pressure distribution in the torch is an important parameter to guess nucleation occurrence in the ICTP torch during TiO_2 nanopowder synthesis. The saturation vapour pressure was calculated from Clausius–Clapeyron equation (P_{sat}):

$$P_{\text{sat}}^{\text{TiO}_2} = P_0 \exp \left\{ \frac{(\Delta H)_{\text{vap}}}{R} \left(\frac{1}{T_0} - \frac{1}{T} \right) \right\} \quad (5.2)$$

where $P_{\text{sat}}^{\text{TiO}_2}$ is the saturation vapour pressure of TiO_2 , P_0 is the reference pressure (atmospheric pressure), $(\Delta H)_{\text{vap}}$ stands for the latent heat for vaporization of TiO_2 , R is the gas constant, T_0 signifies the vaporization temperature of TiO_2 at atmospheric pressure, and T is the gas temperature. In this estimation of the saturation vapor pressure distribution, $T_{\text{ex}}^{\text{Ti}}$ was used as gas temperature T on the assumption of LTE condition. The physical constants and quantities of monomer were collected from databooks [36, 37].

Figure 5.11 shows the estimated saturation vapour pressure distribution of TiO_2 in the ICTP torch. Panel(a) shows the configuration of the ICTP torch and the estimation region,

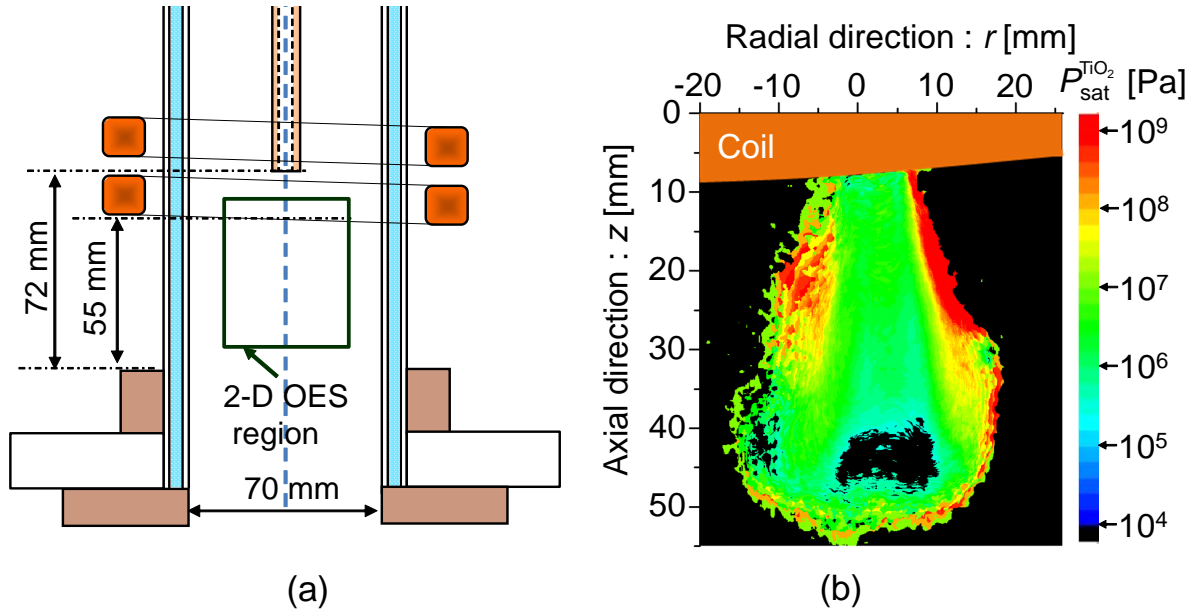


Fig. 5.11: Estimation result of $\text{TiO}_2(\text{g})$ saturation vapour pressure in the ICTP torch.

while panel (b) is the estimated saturation vapour pressure of TiO_2 gas ($P_{\text{sat}}^{\text{TiO}_2}$). As seen in panel(b), $P_{\text{sat}}^{\text{TiO}_2}$ is calculated to be 10^7 – 10^8 Pa at off-axis region, whereas it is less than 10^5 Pa at on-axis region. According to homogeneous nucleation theory, nucleation can occur when the saturation ratio S is greater than unity (supersaturation) at least. The saturation ratio S is expressed as following equation:

$$S = \frac{P_{\text{TiO}_2}}{P_{\text{sat}}^{\text{TiO}_2}} \quad (5.3)$$

where P_{TiO_2} is the partial pressure of $\text{TiO}_2(\text{g})$. As shown in panel(b), the saturation vapour pressure is greater than the ambient pressure ($300 \text{ torr} \sim 4 \times 10^4 \text{ Pa}$) in most of vapour region. This means that nucleation cannot occur there. However, at downstream of on-axis region in the ICTP torch, the saturation vapour pressure $P_{\text{sat}}^{\text{TiO}_2}$ becomes lower than ambient pressure. This implies that TiO_2 vapour can be in supersaturation state if Ti feedstock is efficiently evaporated and then fully mixed with oxygen as shown in figure 5.9(b). This result infers that TiO_2 nuclei could be generated in this downstream region in the ICTP torch. However, it should be noted that nucleation occurrence could be estimated if the partial pressure of $\text{TiO}_2(\text{g})$ would be measured in the ICTP torch. The evaluation of the partial pressure of $\text{TiO}_2(\text{g})$ and then nucleation occurrence are underway in our group.

5.6 Summary

Two-dimensional optical emission spectroscopic (2D OES) observations were conducted to investigate the spatiotemporal distribution of radiation intensities from Ti atomic lines and TiO molecular spectra during TiO₂ nanopowder synthesis using an ICTP torch. Furthermore, the 2D distribution of Ti excitation temperature was estimated from the 2D OES results in the ICTP torch. The 2D OES radiation intensities of Ti and TiO, and the 2D Ti excitation temperature elucidated a fundamental relation between the Ti and TiO vapour and the temperature distribution. These results will be useful to discuss the nucleation occurrence of nanoparticles in the plasma torch.

References

- [1] Malato S, Blanco J, Alarcon D C, Maldonado M I, Fernandez-Ibanez P and Gernjak W 2007 Photocatalytic decontamination and disinfection of water with solar collectors. *Catalysis Today* **122** pp.137–49
- [2] Li J, Zhao X, Wei H, Gu Z Z, and Lu Z 2008 Macroporous ordered titanium dioxide (TiO₂) inverse opal as a new label-free immunosensor. *Analytica Chimica Acta* **625** pp.63–9
- [3] Gratzel M 2001 Photoelectrochemical cells. *Nature* **414** pp.338–44
- [4] Biju K P and Jain M K 2008 Effect of crystallization on humidity sensing properties of sol-gel derived nanocrystalline TiO₂ thin films. *Thin Solid Films* **516** pp.2175–80
- [5] Tsai Y C, Hsi C H, Bai H, Fan S K and Sun D H 2012 Single-step synthesis of Al-doped TiO₂ nanoparticles using non-transferred thermal plasma torch. *Jpn. J. Appl. Phys.* **51** 01AL01
- [6] Shon K H, Cho L D, Na H S, Kim B J, Park J H and Kim H J 2009 Development of a novel method to prepare Fe- and Al-doped TiO₂ from wastewater. *J. Ind. Eng. Chem.* **15** pp.476–82
- [7] Barolo G, Livraghi S, Chiesa M, Cristina M, Paganini C and Giamello E 2012 Mechanism of the photoactivity under visible light of N-doped titanium dioxide. charge carriers migration in irradiated N-TiO₂ investigated by electron paramagnetic resonance. *J. Phys. Chem. C* **116** pp.20887–94
- [8] Lee K N, Kim Y, Lee C W and Jai-Sung Lee J S 2011 Simultaneous amination of TiO₂ nanoparticles in the gas phase synthesis for bio-medical applications *Mater. Sci. Eng.* **18** 082021

-
- [9] Mio M, Kogoma M, Fukui H, and Takeda A 2010 Control of inflammation using adsorption of inflammatory by nano-particles *Chem. Eng.* **55** pp.603-8 (in Japanese)
- [10] Shigeta M and Murphy A B 2011 Thermal plasmas for nanofabrication. *J. Phys. D: Appl. Phys.* **44** 174025
- [11] Girshick S L, Chiu C P, Muno R, Wu C Y, Yang L, Singh S K, and McMurry P H 1993 Thermal plasma synthesis of ultrafine iron particles. *J. Aerosol Sci.* **24** pp.367-82
- [12] Shigeta M, Watanabe T, and Nishiyama H 2004 Numerical investigation for nano-particle synthesis in an RF inductively coupled plasma. *Thin Solid Films* **457** pp.192-200
- [13] Oh S M and Ishigaki T 2004 Preparation of pure rutile and anatase TiO₂ nanopowders using RF thermal plasma. *Thin Solid Films* **457** pp.186-91
- [14] Lee J E, Oh S M, and Park D W 2004 Synthesis of nano-sized Al doped TiO₂ powders using thermal plasma. *Thin Solid Films* **457** pp.230-4
- [15] Ishigaki T, Oh S M, Li J G, and Park D W 2005 Controlling the synthesis of TaC nanopowders by injecting liquid precursor into RF induction plasma. *Sci. & Technol. Advanced Mater.* **6** pp.111-8
- [16] Tong L and Reddy R G 2006 Thermal plasma synthesis of SiC nano-powders/nano-fibers. *Materials Research Bulletin* **41** pp.2303-10
- [17] Ishigaki T and Li J G 2007 Synthesis of functional nanocrystallites through reactive thermal plasma processing. *Sci. & Technol. Advanced Mater.* **8** pp.617-23
- [18] Li J G, Ikeda M, Ye R, Moriyoshi Y, and Ishigaki T 2007 Control of particle size and phase formation of TiO₂ nanoparticles synthesized in RF induction plasma. *J. Phys. D: Appl. Phys.* **40** pp.2348-53
- [19] Tanaka Y, Nagumo T, Sakai H, Uesugi Y, and Nakamura K 2010 Nanoparticle synthesis using high-powered pulse-modulated induction thermal plasma. *J. Phys. D: Appl. Phys.* **43** 265201

-
- [20] Tanaka Y, Sakai H, Tsuke T, Uesugi Y, Sakai Y, and Nakamura K 2011 Influence of coil current modulation on TiO₂ nanoparticle synthesis using pulse-modulated induction thermal plasmas. *Thin Solid Films* **519** pp.7100–05
- [21] Tanaka Y, Tsuke T, Guo W, Uesugi Y, Ishijima T, Watanabe S, and Nakamura K 2012 A large amount synthesis of nanopowder using modulated induction thermal plasmas synchronized with intermittent feeding of raw materials. *J. Phys. D: Conf. Ser.* **406** 012001
- [22] Tanaka Y, Sakai H, Tsuke T, Guo W, Uesugi Y, Sakai Y and Nakamura K 2011 Nanoparticle synthesis using high-power modulated induction thermal plasmas with intermittent synchronized feeding of raw materials. *Proc. 20th Int. Symp. Plasma Chem. ISPC-20*, 346, Philadelphia, USA
- [23] Tanaka Y and Sakuta T 2003 Temperature control of Ar induction thermal plasma with diatomic molecular gases by pulse-amplitude modulation of coil current. *Plasma Sources Sci. & Technol.* **12** pp.69–77
- [24] Tanaka Y, Uesugi Y, and Sakuta T 2007 Controlling the number of excited atoms flowing into the reaction chamber using pulse-modulated induction thermal plasmas at atmospheric pressure. *Plasma Sources Sci. & Technol.* **16** pp.281–9
- [25] Tanaka Y, Guo W, Kodama N, Uesugi Y, Ishijima T, Watanabe S and Nakamura K 2013 A novel approach for large amount synthesis of TiO₂ nanopowder using modulated induction thermal plasmas with time-controlled feeding of feedstock. *Proc. 21st Int. Symp. Plasma Chem. ISPC-21*, 52, Cairns, Australia
- [26] Kodama N, Kita K, Tanaka Y, Uesugi Y, Ishijima T, Watanabe S, and Nakamura K 2014 A method for large-scale synthesis of Al-doped TiO₂ nanopowder using pulse-modulated induction thermal plasmas with time-controlled feedstock feeding. *J. Phys. D: Appl. Phys.* **47** 195304
- [27] Colombo V, Ghedini E, Gherardi M, and Sanibondi P 2013 Evaluation of precursor evaporation in Si nanoparticle synthesis by inductively coupled thermal plasmas. *Plasma Sources Sci. Technol.* **22** 035010

-
- [28] Watanabe T, and Fujiwara K 2004 Nucleation and growth of oxide nanoparticles prepared by induction thermal plasmas *Chem. Eng. Comm.* **191** pp.1343–61
- [29] Shigeta M, and Watanabe T 2010 Growth model of binary alloy nanopowders for thermal plasma synthesis *J. Appl. Phys.* **108** 043306
- [30] Kodama N, Kita K, Tanaka Y, Uesugi Y, Ishijima T, Watanabe S, and Nakamura K 2014 Two-dimensional spectroscopic observation of a pulse-modulated induction thermal plasma torch for nanopowder synthesis. *J. Phys.: Conf. Ser.* **550** 012026
- [31] Kodama N, Kita K, Ishisaka Y, Tanaka Y, Uesugi Y, Ishijima T, Sueyasu S, and Nakamura K 2016 Fundamental study of Ti feedstock evaporation and precursor formation process in inductively coupled thermal plasmas during TiO₂ nanopowder synthesis. *J. Phys. D: Appl. Phys.* **49** 305501
- [32] Olesik J W and Hieftje G M 1985 Optical imaging spectrometers *Anal. Chem.* **57** pp.2049-55
- [33] Webb M R and Hieftje G M Hieftje 2006 Improved monochromatic imaging spectrometer *Appl. Spectro.* **60** pp.57-60
- [34] Boulos M I, Fauchais P and Pfender E 1997 *Thermal plasmas fundamentals and applications vol I* (New York: Plenum)
- [35] NIST atomic spectra database, <http://www.nist.gov/pml/data/asd.cfm>
- [36] Samsonov G V 1982 *The oxide handbook second ed.* (New York: IFI/Plenum)
- [37] The Japan Institute of Metals 2007 *Metals data book fourth ed.* (Tokyo: Maruzen)

Chapter 6

Determination of Ti vapor admixture ratio in the Ar ICTP torch during Ti feedstock injection

6.1 Introduction

Thermal plasmas are widely applied to various material processes such as nanopowder synthesis, surface modification, and thin film deposition [1]- [12]. Inductively coupled thermal plasma (ICTP) is a thermal plasma that is used frequently for nanopowder synthesis because of its high temperature and high chemical activity field and non-contaminating process: it uses electrodeless discharge [13]. For nanopowder synthesis using ICTPs, a solid, liquid, or gas phase feedstock is often injected into a thermal plasma to evaporate and decompose the feedstock to form precursor atomic or molecular particles. The feedstock vapor and precursor vapor are mixed with the thermal plasma gas. Metal feedstock are often used to synthesize metallic nanopowders, metallic oxides, and nitride nanopowders. Especially for metal feedstock evaporation in the ICTP, even only a slight admixture of metal vapor can change the thermal plasma properties markedly, especially elevating electrical conductivity [14, 15]. In the case of ICTP, changing the magnitude of the electrical conductivity affects the plasma temperature distribution and the plasma stability considerably because the ICTP is sustained with induction heating at an electrically conductive channel in the plasma [13]. It is therefore necessary to investigate the spatial distribution of feedstock vapor admixture ratio in an actual ICTP torch. The feedstock admixture ratio distribution might influence plasma properties and plasma stability to a marked degree.

Numerical studies have investigated feedstock evaporation and feedstock vapor distribution in thermal plasmas [16, 17]. Nevertheless, few reports have described experimental investigations of feedstock evaporation or spatial measurement of feedstock vapor during material processing using thermal plasmas. Consequently, some convenient and effective method is desired to measure the feedstock vapor admixture ratio for comparison and for support of numerical calculation results. After feedstock evaporation and precursor formation, nanoparticles are nucleated by homogeneous nucleation and then by heterogeneous nucleation [18]- [20]. In both cases, nanoparticle nucleation depends strongly on the number density and partial pressure of the neutral precursor particle. Some ions can also contribute to nucleation by ion-induced nucleation [21, 22]. Accordingly, the spatial distribution of number densities for various species is also crucially important to augment the understanding of nucleation phenomena.

In the chapters. 3–5, two-dimensional optical emission spectroscopy measurements (2D OES) was carried out to investigate feedstock evaporation experimentally and to investigate precursor formation processes during TiO₂ nanopowder synthesis in the inductively coupled thermal plasma (ICTP) torch. In that work, spatiotemporal distributions of Ti I and TiO spectral radiation intensities were detected by 2D OES method [15, 23]. Furthermore, the spatiotemporal distribution of Ti excitation temperature was inferred from the 2D OES results for Ti I spectral lines [24]. Based on those results, fundamental information of feedstock evaporation and precursor formation and these transportation processes were investigated with the possibility of nucleation during TiO₂ nanopowder synthesis.

This chapter describes the spatial estimation results of Ti excitation temperature $T_{\text{ex}}^{\text{Ti}}$ and the Ti vapor admixture ratio X_{Ti} during Ti feedstock injection into the ICTP torch. Both $T_{\text{ex}}^{\text{Ti}}$ and X_{Ti} , estimated simultaneously, are fundamentally important to study the properties of the thermal plasma with Ti feedstock. First, for this estimation, 2D OES was conducted for Ti I and Ar I atomic spectral lines. Secondly, the emission coefficients of Ti I and Ar I atomic lines were calculated theoretically as a function of temperature and X_{Ti} . Thirdly, the spatial distributions of $T_{\text{ex}}^{\text{Ti}}$ and X_{Ti} were evaluated from 2D OES results and from the theoretically calculated emission coefficients. Finally, the spatial distributions of particle number densities were also estimated for Ar atom, Ti atom, and electrons. Results show that the Ti excitation temperature is lower at the on-axis region in the ICTP torch

t

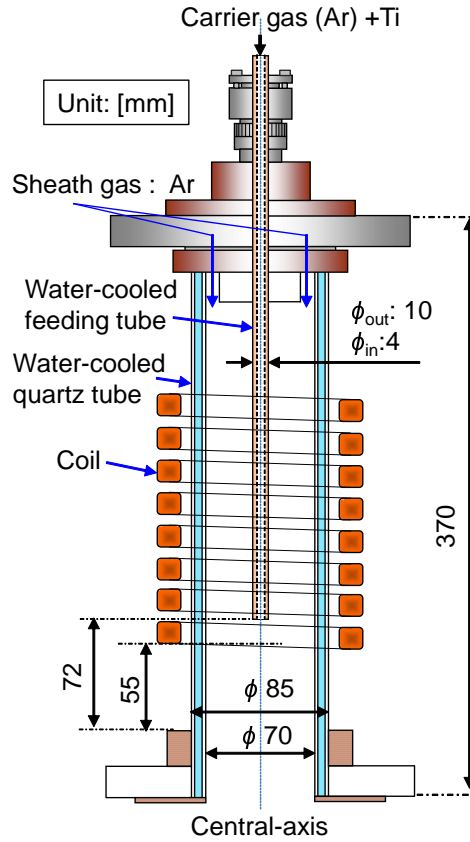


Fig. 6.1: Experimental apparatus using an ICP torch.

with a low Ti vapor admixture ratio, whereas $T_{\text{ex}}^{\text{Ti}}$ is higher in the off-axis region with a high Ti vapor admixture ratio. In addition, the electron density is also estimated as higher in the off-axis region in the ICP torch.

6.2 Experimentals

6.2.1 Experimental configuration

The experimental configuration was almost identical to that reported in our previous work [24]. Figure 6.1 depicts the ICP torch used in this work. The eight-turn of induction coil is installed around a cylindrical quartz tube. The coil is connected to an inverter power supply via a matching circuit. The rf current from the power supply produces an electromagnetic field. This electromagnetic field generates the rf thermal plasma inside the quartz tube of the ICP torch. The feedstock is injected directly into the thermal plasma

through a water-cooled feeding tube inserted from the top of the torch head to the thermal plasma. The reaction chambers and the collection filter are installed downstream of the ICTP torch. Details of these experimental configurations are available in earlier reports of the literature [8, 24].

6.2.2 Experimentals conditions

Table 6.1 shows the experimental conditions of Ti feedstock injection into the Ar ICTP torch. The time-averaged input power from the inverter power supply was fixed at 20 kW. The fundamental frequency of the coil-current was 304 kHz. Pure Ar gas was injected into the torch as a sheath gas. The Ar sheath gas flow rate was fixed at 90 L·min⁻¹. Molecular gas was not added for the fundamental investigation of Ti feedstock evaporation and distribution of the feedstock vapor in the ICTP torch. For this experiment, the Ti feedstock was injected continuously into the Ar ICTP torch. Pure micro-size Ti powder (TILOP-45; Osaka Titanium Technologies Co. Ltd.) was used as the feedstock. Feedstock was injected continuously into the ICTP torch with Ar carrier gas. The Ar carrier gas flow rate was set to 4 L·min⁻¹. The feedstock feeding rate was adjusted about 1.0 g·min⁻¹. This feedstock feeding rate is lower than that used in our earlier work investigating large-scale nanopowder synthesis [8]. The low feeding rate conditions were selected to investigate the fundamental behavior of feedstock evaporation and feedstock vapor in the ICTP torch.

6.2.3 Optical emission spectroscopy setup

First, a wavelength-resolved OES was conducted for the below coil-end region to confirm the atomic spectral lines and the contribution of the continuum spectra. Figure 6.2 depicts OES results at 20 mm below the coil-end for wavelengths between (a) 430–830 nm and (b) 430–530 nm. Figure 6.2 shows that many atomic spectral lines for Ar I and Ti I were detected at the region below coil-end. In addition, the radiation intensity of the continuum spectra was much lower than that of Ar I and Ti I spectral lines. Consequently, the influence of continuum spectra can be negligible for the determination of temperature and Ti vapor admixture ratio. Two-dimensional OES was conducted for the region, including this OES region.

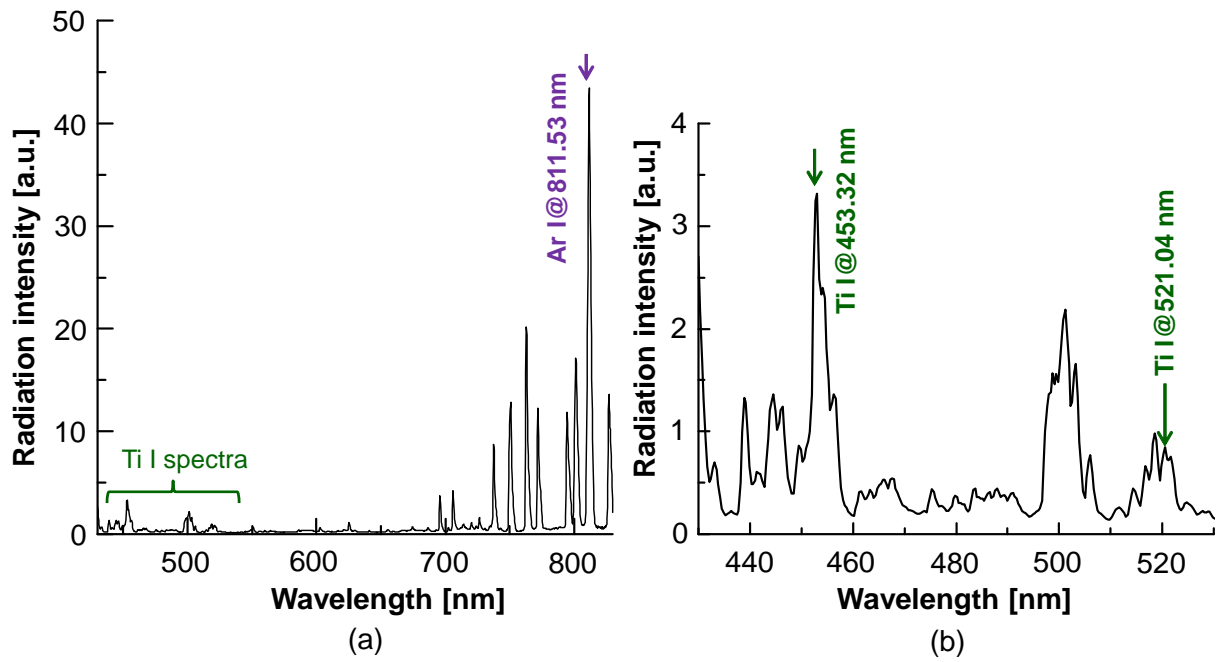


Fig. 6.2: OES spectra for the region below the coil-end (a) $\lambda=430$ nm to 830 nm, and (b) Ti I spectra ($\lambda=430$ nm to 530 nm).

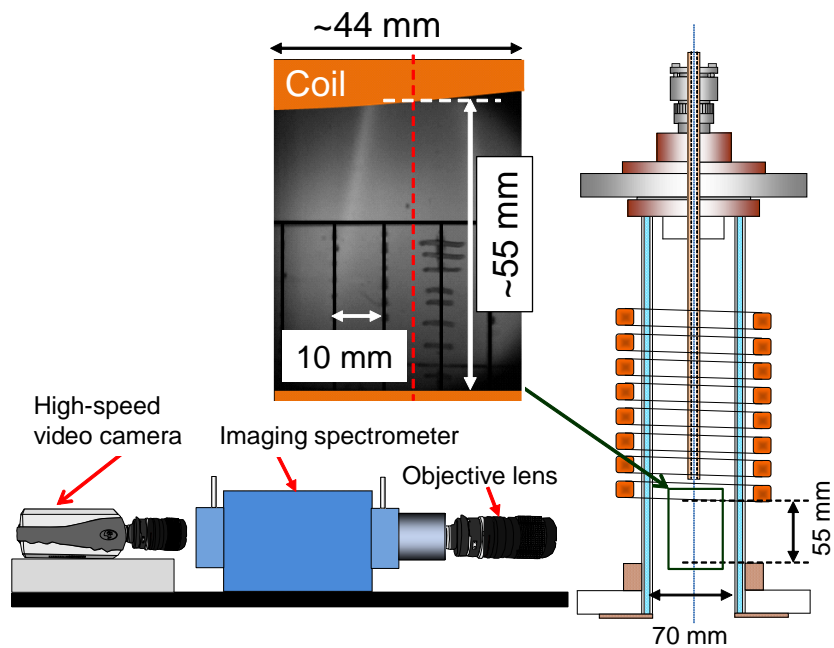


Fig. 6.3: 2D OES region in this work.

Table 6.1: Experimental conditions.

Time-averaged input power	20 kW
Fundamental frequency of the coil current	304 kHz
Modulation	Non-modulation
Pressure	300 Torr (~ 40 kPa)
Gas composition	Ar: $90 \text{ L}\cdot\text{min}^{-1}$
Carrier gas flow rate	Ar: $4 \text{ L}\cdot\text{min}^{-1}$
Quenching gas	Non-injection
Powder feed rate g_{pow}	$1.0 \text{ g}\cdot\text{min}^{-1}$
Feedstock	100 wt%Ti powder $\bar{d} = 27 \mu\text{m}, d < 45 \mu\text{m}$

The 2D OES measurements were conducted using a 2D OES system (AN-IMC-DD; Anfi Inc.). Details and principles of 2D OES measurement system are available in the literature and in our earlier work [24–26]. This 2D OES system consists of an objective lens (AF Zoom-Nikkor 80-200 mm f/2.8D ED; Nikon Corp.), an imaging spectrometer (Acton Spectra Pro 2300i; Princeton Instruments, Inc.), and a high-speed video camera (GX-8; NAC Image Technology Inc.), as portrayed in Fig. 6.3. The observation region was set to approximately $44 \times 55 \text{ mm}^2$ region below the coil-end, as shown in Fig. 6.3. The diffraction grating of the imaging spectrometer was $1200 \text{ grooves}\cdot\text{mm}^{-1}$ with a blaze wavelength of 750 nm. The wavelength resolution of 2D OES system was 0.8 nm, which is quite higher than that for a conventional 2D OES system consisting of optical interference bandpass filters. In this work, two Ti I spectral lines were observed at wavelengths (λ)=453.32 nm and λ =521.04 nm to estimate Ti excitation temperature distribution in the ICTP torch. In addition, an Ar I line was observed at λ =811.53 nm to use for determination of the Ti vapor admixture ratio distribution. Figure 6.2 shows that these atomic lines were selected based on the OES result. A high-speed video camera was used to capture optical 2D images of the specified spectra. The frame rate of the high-speed video camera was set to 1000 frames per second. Accumulation and averaging were conducted four times to reduce the contribution from a noise signal. These 2D OES conditions are summarized in Tab. 6.2.

Table 6.2: Two-dimensional spectroscopic observation conditions.

Observation area	44 × 55 mm ² region below the coil end
Diffraction grating	1200 grooves·mm ⁻¹
Wavelength resolution	0.8 nm
Spectral lines observed	Ti I (453.32 nm) and Ti I (521.04 nm) Ar I (811.53 nm)
Frame rate for high speed video camera	1000 fps

The Ti excitation temperature was estimated using a two-line method for two Ti I atomic spectra [24]. The Ti vapor admixture ratio was ascertained from the radiation intensity ratio between Ti I line at $\lambda=521.04$ nm and Ar I line at $\lambda=811.53$ nm $I_{\text{Ti@521}}/I_{\text{Ar@811}}$. Details of the determination procedure are described in the following sections.

6.3 Determination procedure

6.3.1 Determination of Ti excitation temperature

The Ti excitation temperature was estimated using our two-line method from the two observed Ti I atomic lines at $\lambda=453.32$ nm and $\lambda=521.04$ nm. The local thermodynamic equilibrium (LTE) was assumed to estimate Ti excitation temperature. The radiation intensity of Ti I spectral line at $\lambda=453.32$ nm ($I_{\text{Ti@453}}$) is superimposed from the contributions of two Ti I spectral lines at $\lambda=453.3240$ nm and $\lambda=453.4776$ nm, whereas the radiation intensity $I_{\text{Ti@521}}$ is obtained from a Ti I spectral line at $\lambda=521.04$ nm. Consequently, the intensity ratio $I_{\text{Ti@453}}/I_{\text{Ti@521}}$ can be expressed as a function of $T_{\text{ex}}^{\text{Ti}}$ as

$$\frac{I_{\text{Ti@453}}}{I_{\text{Ti@521}}} = \frac{\frac{g_p A_{pq}}{\lambda_{pq}} \exp\left(-\frac{E_p}{kT_{\text{ex}}^{\text{Ti}}}\right) + \frac{g_k A_{kl}}{\lambda_{kl}} \exp\left(-\frac{E_k}{kT_{\text{ex}}^{\text{Ti}}}\right)}{\frac{g_m A_{mn}}{\lambda_{mn}} \exp\left(-\frac{E_m}{kT_{\text{ex}}^{\text{Ti}}}\right)} \quad (6.1)$$

where k is the Boltzmann constant, λ_{pq} , λ_{kl} and λ_{mn} respectively represent the wavelength for Ti I atomic spectra at 453.3240 nm, at 453.4776 nm and at 521.0384 nm, g_p , g_k and g_m respectively denote the degeneracies of the upper energy level for the Ti I spectral

lines, A_{pq} , A_{kl} , A_{mn} respectively signify the transition probabilities for Ti I spectral lines, and E_p , E_k and E_m denote the upper energy levels for the respective Ti I spectral lines. These physical data were collected from an NIST database [27]. The estimated $T_{\text{ex}}^{\text{Ti}}$ was treated as an almost identical value to that of the heavy particle temperature assuming an LTE condition. For the thermal plasma, the collision frequencies for electron – heavy particles and heavy particles – heavy particles are much higher than those for non-thermal plasmas because of the higher electron and heavy particle temperatures and the higher gas pressure. Because of these high collision frequencies, the thermal plasma produces a nearly LTE condition. Consequently, the population at excited states follows the Boltzmann distribution in many cases of thermal plasma [13, 24]

Regarding the estimation of $T_{\text{ex}}^{\text{Ti}}$, the contribution from continuum spectra was neglected because of its lower radiation intensity, as shown in Fig. 6.2.

6.3.2 Definition of the Ti vapor admixture ratio

The Ti vapor admixture ratio X_{Ti} was ascertained from 2D OES results for Ti I atomic lines and an Ar I line. The quantity X_{Ti} is defined as the total molar ratio of titanium-containing species, as presented in the following expression:

$$X_{\text{Ti}} = M_{\text{Ti}} + M_{\text{Ti}^+} + M_{\text{Ti}^{2+}} \quad (6.2)$$

where M_{Ti} , M_{Ti^+} , and $M_{\text{Ti}^{2+}}$ respectively denote the molar fraction of Ti atom, Ti^+ and Ti^{2+} ions, respectively. Here, Ti^{3+} ion was neglected because of its high ionization potential [27]. The following assumptions were adopted to ascertain X_{Ti} : (a) LTE, (b) constant pressure, and (c) optically thin. The Ti vapor admixture ratio was determined according to the flowchart portrayed in Fig. 6.4. The quantity X_{Ti} was determined by the comparison between experimentally obtained radiation intensity ratio and theoretically calculated emission coefficient ratio between Ti I and Ar I. Emission coefficients were calculated from computed equilibrium particle composition for the Ar-Ti system as described in the following section.

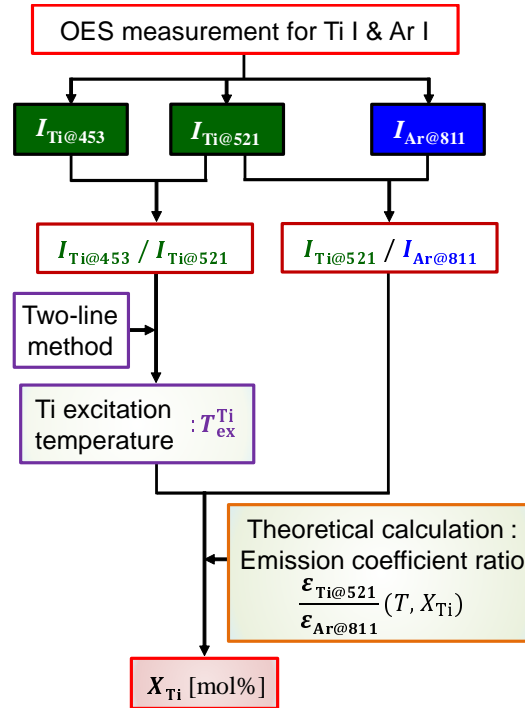


Fig. 6.4: Flowchart to determine Ti excitation temperature and Ti vapor admixture ratio.

6.3.3 Equilibrium particle compositions

The equilibrium particle compositions for Ar–Ti system were calculated as a function of temperature and X_{Ti} . Minimization of the Gibbs's free energy of a system was performed to calculate the equilibrium particle composition [15]. For calculations, X_{Ti} was changed from 10^{-9}mol\%Ti to 99mol\%Ti . These calculations were conducted under constant pressure at 300 Torr (~ 40 kPa). Figure 6.5 presents the calculated equilibrium particle compositions for the Ar-Ti system in the respective conditions of (a) 1 mol%Ti and (b) 10^{-5}mol\%Ti . The condition of 1 mol%Ti corresponds to non-dilute Ti vapor admixture condition, whereas the condition of 10^{-5}mol\%Ti corresponds to the dilute Ti vapor admixture condition.

In panel(a) for the 1 mol%Ti admixture condition, particles of all kinds are ionized at temperatures higher than 10000 K. At temperatures below 5000 K, the number density of Ti^+ ion is high, although the number density of Ar^+ ion is low. This difference occurs because of the lower ionization potential of Ti atom (~ 6.83 eV) compared with that of Ar atom (~ 15.76 eV). In addition, the density of Ti^+ density is almost equal to the electron number density. Consequently, most of the electrons are supplied because of ionization of Ti

atoms at temperatures below 5000 K. Panel (b) presents calculation results for the dilute Ti vapor admixing condition. In this case, the number density of electrons is almost identical, with Ar^+ density at temperatures over about 4500 K, although it is almost identical with Ti^+ density at temperatures below about 4500 K. Consequently, electrons are supplied because of Ar atom ionization at temperatures higher than approximately 4500 K and Ti atom ionization at temperatures below about 4500 K. However, the electron density is lower than that for 1 mol%Ti condition because of the low Ti vapor admixture ratio and high ionization potential of Ar atom.

6.3.4 Procedure for determination of the Ti vapor admixture ratio and particle number densities

The Ti vapor admixture ratio was determined by the comparison between experimentally obtained radiation intensity ratio and theoretically calculated emission coefficient ratio between Ti I and Ar I. In the determination of X_{Ti} , the equilibrium particle composition of Ar-Ti system was first calculated as a function of temperature and X_{Ti} , as shown in Fig. 6.5. From the calculated particle compositions, the emission coefficient ratio of Ti I line at $\lambda = 521.04$ nm and Ar I line at $\lambda = 811.53$ nm, i.e. $\varepsilon_{\text{Ti@521}}/\varepsilon_{\text{Ar@811}}$ was calculated as a function of temperature T and X_{Ti} . The emission coefficient ratio $\varepsilon_{\text{Ti@521}}/\varepsilon_{\text{Ar@811}}$ was calculated using the following expression:

$$\frac{\varepsilon_{\text{Ti@521}}}{\varepsilon_{\text{Ar@811}}} = \frac{\frac{n_{\text{Ti}}}{4\pi Z_{\text{Ti}}(T)} \frac{hc}{\lambda_{\text{Ti@521}}} g_p^{\text{Ti@521}} A_{pq}^{\text{Ti@521}} \exp\left(-\frac{E_p^{\text{Ti@521}}}{kT}\right)}{\frac{n_{\text{Ar}}}{4\pi Z_{\text{Ar}}(T)} \frac{hc}{\lambda_{\text{Ar@811}}} g_p^{\text{Ar@811}} A_{pq}^{\text{Ar@811}} \exp\left(-\frac{E_p^{\text{Ar@811}}}{kT}\right)} \quad (6.3)$$

where h is the Planck constant, c is the speed of light, n_{Ti} and n_{Ar} respectively denote the number densities of Ti and Ar atoms, Z_{Ti} and Z_{Ar} respectively represent the partition functions of Ti and Ar atoms, $\lambda_{\text{Ti@521}}$ and $\lambda_{\text{Ar@811}}$ respectively signify the spectral wavelengths of Ti I at 521.0384 nm and Ar I at 811.53 nm, $g_p^{\text{Ti@521}}$ and $g_p^{\text{Ar@811}}$ respectively represent the degeneracies of the upper energy levels for Ti I and Ar I spectra, $A_{pq}^{\text{Ti@521}}$ and $A_{pq}^{\text{Ar@811}}$ respectively signify the transition probabilities for Ti I and Ar I spectra, and $E_p^{\text{Ti@521}}$ and $E_p^{\text{Ar@811}}$ respectively represent the upper energy levels for Ti I and Ar I spectra. The number densities of Ti and Ar atoms were collected from calculation results of equilibrium particle compositions for Ar-Ti system.

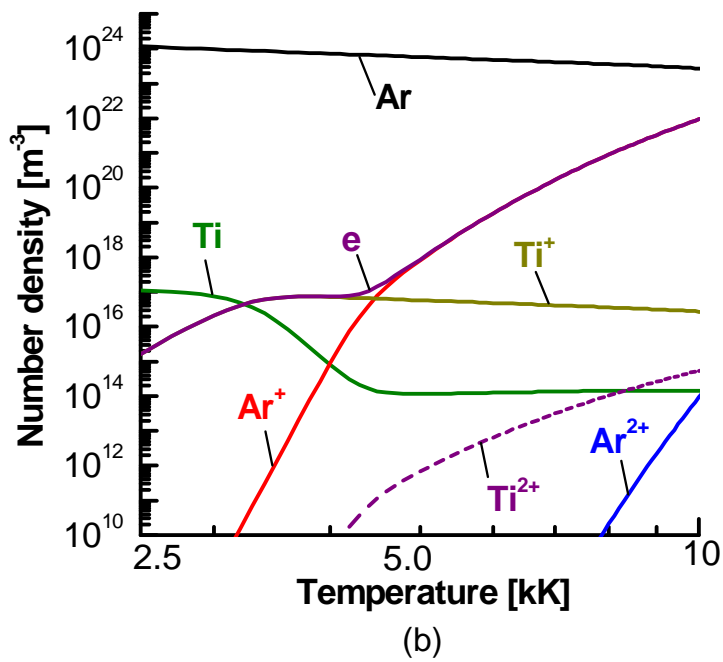
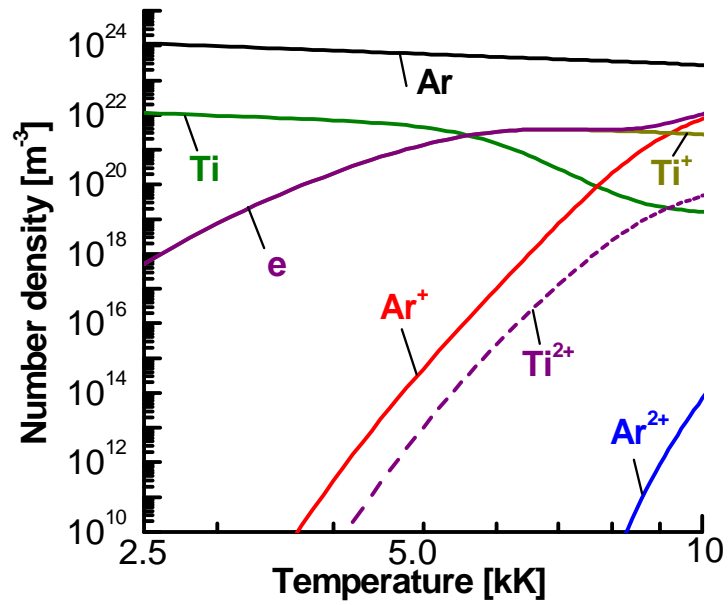


Fig. 6.5: Equilibrium particle compositions for Ar-Ti system at pressure of 300 Torr: (a) 1 mol%Ti and (b) 10^{-5} mol%Ti.

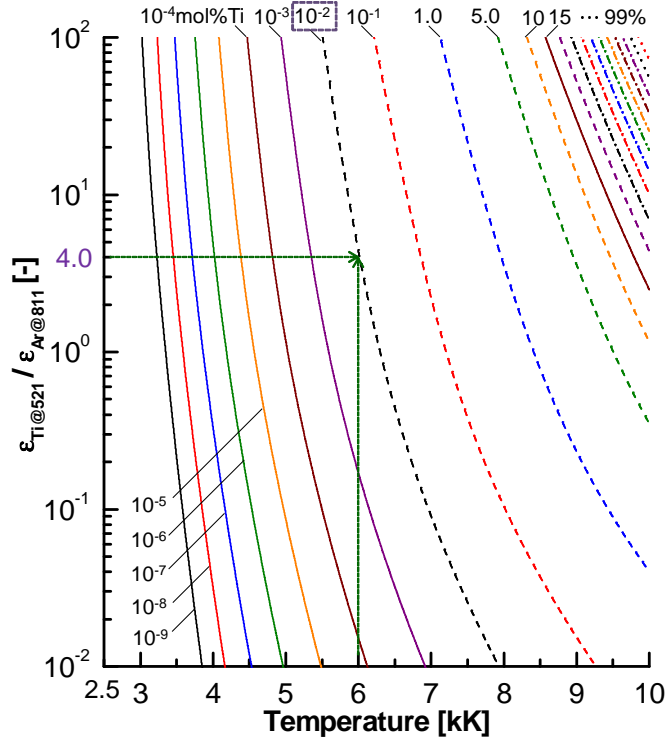


Fig. 6.6: Emission coefficient ratio between Ti I@521.04 nm and Ar I@811.53 nm as a function of temperature and Ti vapor admixture ratio.

Figure 6.6 shows the emission coefficient ratio calculated as a function of temperature T and X_{Ti} . The calculated $\varepsilon_{\text{Ti@521}}/\varepsilon_{\text{Ar@811}}$ was treated as the same value of $I_{\text{Ti@521}}/I_{\text{Ar@811}}$ on the assumption of optically thin character. From the OES results, $T_{\text{ex}}^{\text{Ti}}$ was estimated using two-line method for Ti I radiation intensities, as described in section 6.3.1. The radiation intensity ratio $I_{\text{Ti@521}}/I_{\text{Ar@811}}$ was determined. The value X_{Ti} was estimated from Fig. 6.6 with $T_{\text{ex}}^{\text{Ti}}$ and $I_{\text{Ti@521}}/I_{\text{Ar@811}}$. If the temperature and $I_{\text{Ti@521}}/I_{\text{Ar@811}}$ are, respectively, 6.0 kK and 4.0, then X_{Ti} is estimated as about $10^{-2}\text{mol}\%\text{Ti}$ according to Fig. 6.6.

The number densities of Ar atom n_{Ar} , Ti atom n_{Ti} and electron n_e were also determined using estimation results of $T_{\text{ex}}^{\text{Ti}}$ and X_{Ti} . Figure 6.7 depicts (a) the Ar atomic number density, (b) the Ti atomic number density, and (c) the electron density calculated as a functions of temperature T and X_{Ti} . These relations were obtained from calculation results of equilibrium particle composition for the Ar-Ti system. The particle number densities were determined from Fig. 6.7. If the temperature and X_{Ti} are determined respectively as 6.0 kK and $10^{-2}\text{mol}\%\text{Ti}$, then n_{Ti} is estimated as about $4 \times 10^{17} \text{ m}^{-3}$ from Fig. 6.7. This

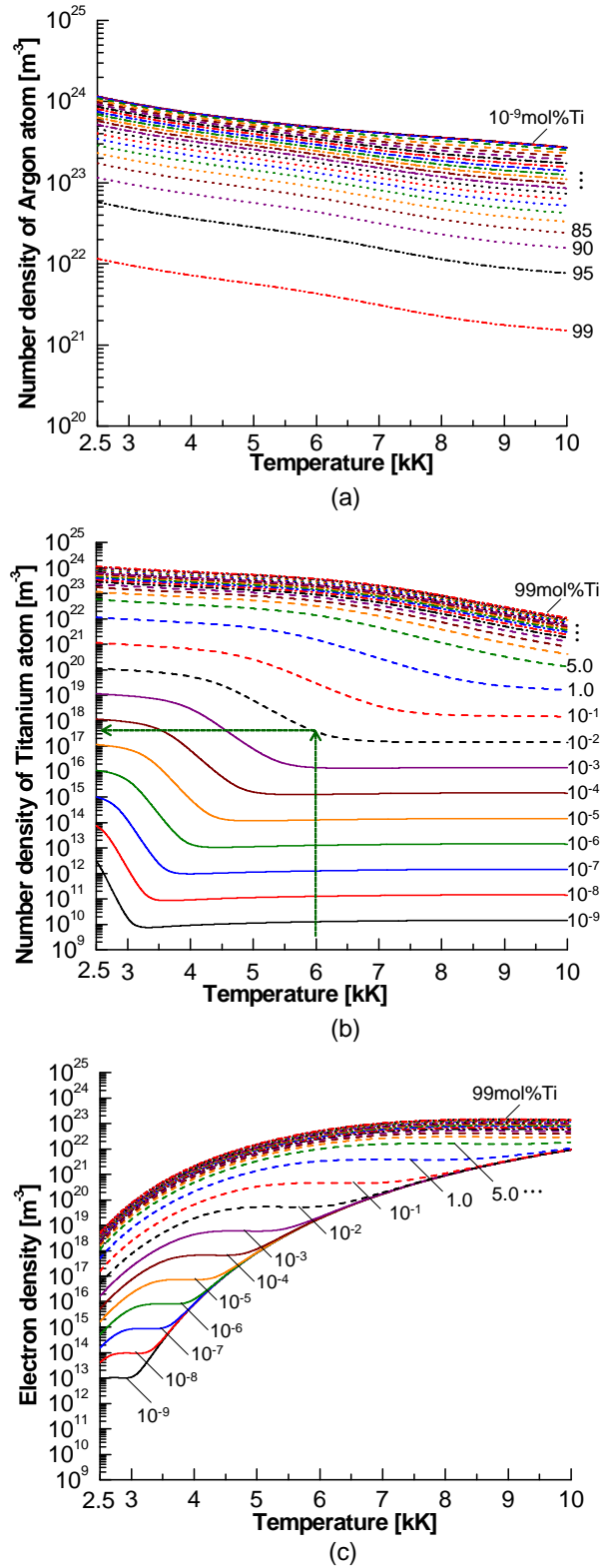


Fig. 6.7: Particle number densities as a function of the temperature and Ti vapor admixture ratio: (a) number density of Ar atom, (b) number density of Ti atom, and (c) electron density.

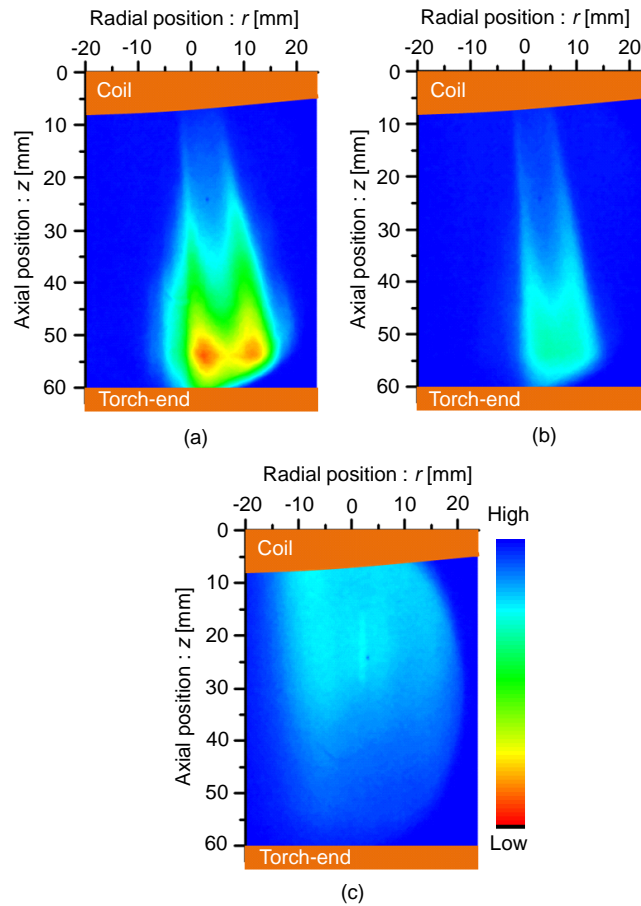


Fig. 6.8: 2D OES results for Ti I and Ar I atomic spectra: (a) Ti I ($\lambda=453.32$ nm), (b) Ti I ($\lambda=521.04$ nm), and (c) Ar I ($\lambda=811.53$ nm).

estimated number density including density of Ti atoms in the ground state and all the excited states. The Ar atomic number density and electron density are ascertained using the same procedure.

In this experiment, the Ar carrier gas was injected with Ti feedstock into the central axis region in the ICTP torch. Consequently, the Ar atomic number density certainly increases at the central axis region in the ICTP torch. From the reason represented above, the validity of this estimation method was discussed from the estimation results of the Ar atomic number density distribution.

6.4 Results and discussion

6.4.1 Spatial distribution of Ti I and Ar I radiation intensities

Figure 6.8 portrays the 2D OES results obtained for two Ti atomic lines and one Ar atomic line. Panels (a) and (b) respectively present the spatial distribution of Ti I radiation intensities at wavelengths of 453.32 nm and 521.04 nm. Panel (c) depicts spatial distribution of Ar I radiation intensity at the wavelength of 811.53 nm. In panels (a)–(c), the coil-end and torch-end positions are illustrated with axial coordinate z and radial coordinate r . The radial position $r = 0$ mm roughly corresponds to the central axis of the ICTP torch.

As shown in panel (a), radiation intensity of Ti I at 453.32 nm was detected in the region of about $|r| < 15$ mm. The radiation intensity of Ti I was increased at the downstream region of ICTP torch. This Ti I radiation intensity suggests that Ti atomic vapor existed in the region of about $|r| < 15$ mm. A similar spatial distribution of radiation intensity was obtained for Ti I at 521.04 nm as shown in panel (b). However, details of the radiation intensity distribution differed because the excited state of these spectra differ. In this experiment, Ar gas was injected into the ICTP torch as sheath gas. Consequently, Ar I radiation intensity was detected at the whole region in the ICTP torch in contrast to the radiation intensity of Ti I spectral lines, as shown in panel (c). The Ti excitation temperature was estimated from 2D OES result for Ti I atomic lines. However, Abel inversion was not adopted to estimate $T_{\text{ex}}^{\text{Ti}}$ because of the non-complete axis-symmetric structure of Ti I radiation intensities. Abel inversion for non-complete axis-symmetric structure produces a large error of over 2000 K [24]. In contrary, the temperature error without Abel inversion is less than 1000 K, especially for central axis region [24].

6.4.2 Spatial distribution of Ti excitation temperature

The Ti excitation temperature $T_{\text{ex}}^{\text{Ti}}$ was estimated using the two-line method for two Ti I radiation intensity distributions.

Figure 6.9 portrays (a) spatial distribution of Ti I at 453.32 nm and (b) $T_{\text{ex}}^{\text{Ti}}$ in the ICTP torch. In panel (b), the black region corresponds to the region in which $T_{\text{ex}}^{\text{Ti}}$ was unable to be estimated because of its extremely low Ti I radiation intensity. In addition, the region

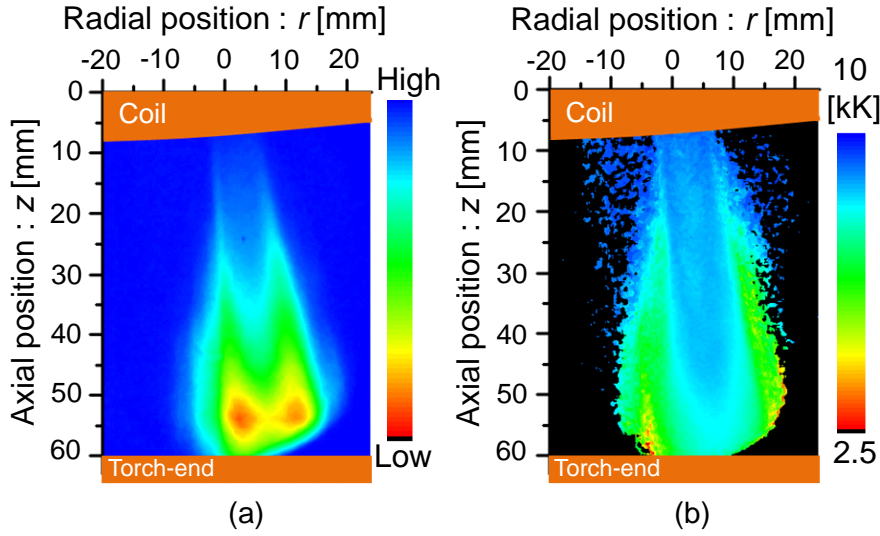


Fig. 6.9: Determination result for spatial distribution of Ti excitation temperature: (a) Ti I ($\lambda=453.32$ nm) and (b) Ti excitation temperature $T_{\text{ex}}^{\text{Ti}}$.

in which $T_{\text{ex}}^{\text{Ti}}$ was estimated as below 2500 K is shown in black because of a lack of accuracy in the determination of temperature.

In Fig. 6.9 (b), $T_{\text{ex}}^{\text{Ti}}$ around on-axis ($r \sim 0$ mm) was estimated as about 2500–4000 K, which is lower than $T_{\text{ex}}^{\text{Ti}}$ estimated at off-axis region ($|r| \sim 5$ –10 mm). For this experiment, the Ti feedstock powder was injected into the on-axis region with low-temperature Ar carrier gas ($T \sim 300$ K). Furthermore, the injected Ti feedstock was evaporated in the on-axis region. Then, evaporation of the Ti feedstock consumes energy at the on-axis region. Consequently, on-axis temperature can be quenched because of Ar carrier gas injection and decreased by feedstock evaporation. The similar temperature drop caused by feedstock loading is reported from the numerical simulation of copper feedstock evaporation in Ar ICTP torch [16]. However, the $T_{\text{ex}}^{\text{Ti}}$ estimated at the off-axis region was higher than 4500 K, which is higher than the on-axis temperature. The reason for the higher temperature in off-axis region is the contribution of induction heating by eddy current in the ICTP torch. The contribution of induction heating is discussed in section 6.4.4.

6.4.3 Estimation result of Ti vapor admixture ratio

The Ti vapor admixture ratio was estimated from the estimation result of $T_{\text{ex}}^{\text{Ti}}$ and radiation intensity ratio between Ti I at 521.04 nm and Ar I at 811.53 nm. Figure 6.10 portrays

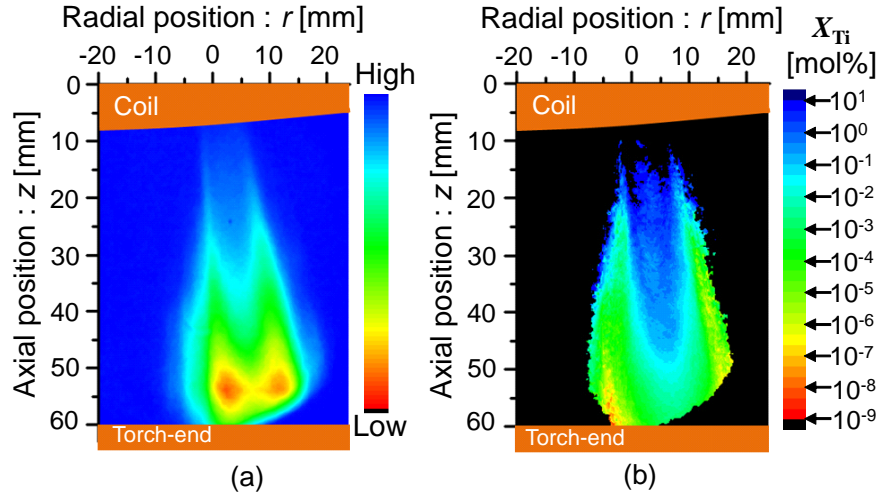


Fig. 6.10: Estimation result for spatial distribution of Ti vapor admixture ratio: (a) Ti I ($\lambda=453.32$ nm) and (b) Ti vapor admixture ratio X_{Ti} .

a spatial distribution of the Ti vapor admixture ratio in the ICTP torch. The Ti vapor admixture ratio was estimated as 10^{-9}mol\%Ti – 99mol\%Ti . The Ti vapor admixture ratio less than 10^{-9}mol\%Ti is shown as black.

The Ti vapor admixture ratio was estimated as $X_{\text{Ti}} \leq 10^{-8}\text{mol\%Ti}$ at the upstream region of the on-axis ($z \sim 10$ – 20 mm), which was elevated along with increasing axial position. For the downstream region at the off-axis, X_{Ti} was estimated as 10^{-6} – 10^{-3}mol\%Ti , which was much higher than X_{Ti} in the upstream region. These estimation results show clearly that most of injected Ti feedstock was gradually evaporated during its transportation toward downstream region in the ICTP torch without instantaneous evaporation. In addition, the feedstock was diffused toward the off-axis region. Then it was evaporated efficiently at the high-temperature region in the off-axis.

The admixing of high-density Ti atomic vapor changes the plasma composition and plasma properties such as electrical conductivity significantly. The influence of Ti feedstock vapor admixing on temperature was discussed in the next section based on the estimation result

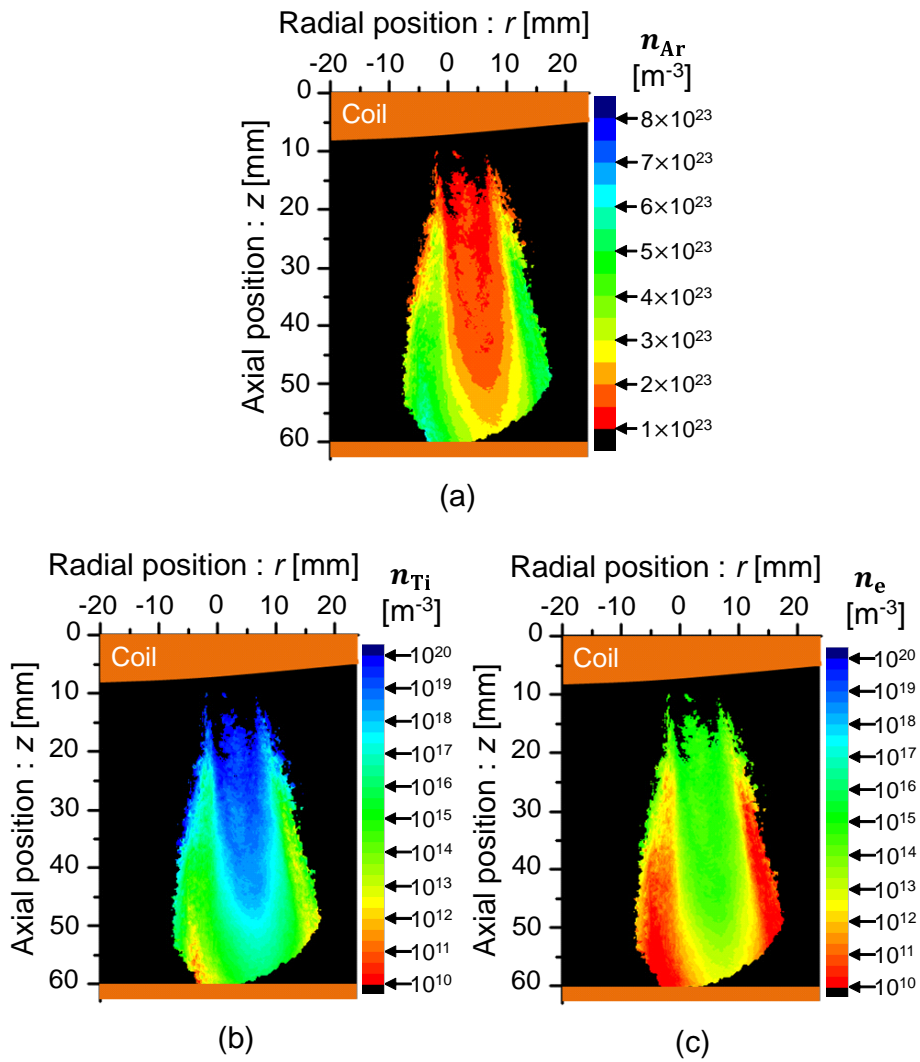


Fig. 6.11: Spatial distribution of particle number densities: (a) Ar atomic number density n_{Ar} , (b) Ti atomic number density n_{Ti} , and (c) electron density n_e .

6.4.4 Estimation result of particle number density

The particle number densities were also determined from the estimation result of $T_{\text{ex}}^{\text{Ti}}$ and X_{Ti} . Figure 6.11 presents estimation results of (a) Ar atomic number density n_{Ar} , (b) Ti atomic number density n_{Ti} and (c) electron density n_e .

From panel (a), the number density of Ar atom was estimated as higher at the on-axis region in the ICTP torch. The reason for the high Ar number density is injection of Ar carrier gas into the on-axis region. The distribution of n_{Ti} revealed a quite similar distribution of X_{Ti} shown in Fig. 6.10 (b). This similarity occurs because n_{Ti} is almost proportional to X_{Ti} , as portrayed in Fig. 6.7.

The Ti atomic number density was estimated as about 10^{10} – 10^{13} m^{-3} at the on-axis region and as about 10^{13} – 10^{15} at the off-axis region. In this experiment, Ti feedstock was injected continuously into the torch with the feeding rate of about 1.0 $\text{g}\cdot\text{min}^{-1}$ (approximately 3.5×10^{-7} mol ms^{-1}), as indicated in the experimental condition. Consequently, the number of about 10^{17} Ti atoms can be supplied into the ICTP torch every millisecond if the injected Ti feedstock is evaporated completely. However, n_{Ti} was estimated as much lower than 10^{17} in the ICTP torch. This result implied that injected Ti feedstock was not evaporated completely in the Ar ICTP torch. As shown in panel(c), n_e was estimated as approximately 10^{14} – 10^{16} m^{-3} at the on-axis region and as 10^{17} – 10^{20} m^{-3} at the off-axis region. The distribution of n_e was a quite similar distribution of X_{Ti} and n_{Ti} . In the case of the Ar–Ti system, most electrons are supplied by ionization of Ti atom because of the lower ionization potential of Ti atom (~ 6.83 eV) compared to that of Ar atom (~ 15.76 eV), as presented in Fig. 6.5. Consequently, electron density increased with increased Ti vapor admixture ratio.

According to the Chapman–Enskog method, electrical conductivity σ is proportional to n_e [28]. In addition, the current density of eddy current j is expressed as $j = \sigma E$ according to Ohm’s law, where E is the electric field. Therefore, the current density j was increased at the off-axis region, resulting in enhancement of Joule heating. However, it is noteworthy that Ti vapor admixing elevates the radiation loss simultaneously. Consequently, the temperature increase is limited by energy balance between Joule heating and radiative energy loss.

6.5 Summary

The two-dimensional optical emission spectroscopy (2D OES) was conducted during Ti feedstock injection into the Ar ICTP torch. The spatial distribution of Ti excitation temperature, Ti vapor admixture ratio, and number densities of Ar, Ti atoms, and electrons were estimated from the 2D OES results for Ti I and Ar I atomic lines. The estimation results demonstrated that high temperatures are maintained because of Joule heating at the off-axis region and that the injected Ti feedstock is efficiently evaporated in the high-temperature off-axis region.

References

- [1] Shigeta M and Murphy A B 2011 Thermal plasmas for nanofabrication. *J. Phys. D: Appl. Phys.* **44** 174025
- [2] Girshick S L, Chiu C P, Muno R, Wu C Y, Yang L, Singh S K, and McMurry P H 1993 Thermal plasma synthesis of ultrafine iron particles. *J. Aerosol Sci.* **24** pp.367–82
- [3] Oh S M and Ishigaki T 2004 Preparation of pure rutile and anatase TiO₂ nanopowders using RF thermal plasma. *Thin Solid Films* **457** pp.186–91
- [4] Ishigaki T, Oh S M, Li J G, and Park D W 2005 Controlling the synthesis of TaC nanopowders by injecting liquid precursor into RF induction plasma. *Sci. & Technol. Advanced Mater.* **6** pp.111–8
- [5] Kambara M, Kitayama A, Homma K, Hideshima T, Kaga M, Sheem K Y, Ishida S and Yoshida T 2014 Nano-composite Si particle formation by plasma spraying for negative electrode of Li ion batteries. *J. Appl. Phys.* **115** 143302
- [6] Watanabe T and Fujiwara K 2004 Nucleation and growth of oxide nanoparticles prepared by induction thermal plasmas *Chem. Eng. Comm.* **191** pp.1343–61
- [7] Tanaka Y, Guo W, Kodama N, Uesugi Y, Ishijima T, Watanabe S and Nakamura K 2013 A novel approach for large amount synthesis of TiO₂ nanopowder using modulated induction thermal plasmas with time-controlled feeding of feedstock. *Proc. 21st Int. Symp. Plasma Chem. ISPC-21*, 52, Cairns, Australia
- [8] Kodama N, Kita K, Tanaka Y, Uesugi Y, Ishijima T, Watanabe S, and Nakamura K 2014 A method for large-scale synthesis of Al-doped TiO₂ nanopowder using pulse-modulated induction thermal plasmas with time-controlled feedstock feeding. *J. Phys. D: Appl. Phys.* **47** 195304

-
- [9] Kim K S, Kingston C T, Hydna A, Jakubinek M B, Guan J, Plunkett M, and Simard B 2014 Hydrogen-catalyzed, pilot-scale production of small-diameter boron nitride nanotubes and their macroscopic assemblies. *ACS Nano* **8** pp.6211-20
- [10] Mavier F, Rat V, Bienia M, Lejeune M, and Coudert J F 2017 Suspension and precursor solution plasma spraying by means of synchronous injection in a pulsed arc plasma. *Surf. Coatings Technol.* **318** pp.18-27
- [11] Liao F, Girshick S L, Mook W M, Gerberich W W, and Zachariah M R 2005 Superhard nanocrystalline silicon carbide films. *Appl. Phys. Lett.* **86** 171913
- [12] Maruyama Y, Tanaka Y, Irie H, Tsuchiya T, and Tial M K S, Uesugi Y, Ishijima T, Yukimoto T, and Kawamura H 2017 Rapid surface oxidation of the Si substrate using longitudinally long Ar/O₂ loop type of inductively coupled thermal plasmas. *IEEE Trans. Plasma Sci.* **44** pp.3164–71
- [13] Boulos M I, Fauchais P and Pfender E 1997 *Thermal Plasmas Fundamentals and Applications vol. I* (New York: Plenum)
- [14] Mostaghimi J and Pfender E 1984 Effects of metallic vapor on the properties of an argon arc plasma. *Plasma Chem. Plasma Process.* **4** pp.129–39
- [15] Kodama N, Kita K, Ishisaka Y, Tanaka Y, Uesugi Y, Ishijima T, Sueyasu S, and Nakamura K 2016 Fundamental study of Ti feedstock evaporation and precursor formation process in inductively coupled thermal plasmas during TiO₂ nanopowder synthesis. *J. Phys. D: Appl. Phys.* **49** 305501
- [16] Proulx P, Mostaghimi J, and Boulos M I 1985 Plasma-particle interaction effects in induction plasma modelling under dense loading conditions. *Int. J. Heat Mass Transfer* **28** pp.1327–36
- [17] Colombo V, Ghedini E, Gherardi M, and Sanibondi P 2013 Evaluation of precursor evaporation in Si nanoparticle synthesis by inductively coupled thermal plasmas. *Plasma Sources Sci. Technol.* **22** 035010
- [18] Friedlander S K 2000 *Smoke, dust and haze, fundamentals of aerosol dynamics second edn.* (Oxford: Oxford University Press)

-
- [19] Seinfeld J H and Pandis S N 1998 *Atmospheric chemistry and physics, from air pollution to climate change* (New York: Wiley)
- [20] Shigeta M and Watanabe T 2010 Growth model of binary alloy nanopowders for thermal plasma synthesis *J. Appl. Phys.* **108** 043306
- [21] Girshick S L, Rao N P and Kelkar M 1996 Model for ion-induced nucleation based on properties of small ionic clusters. *J. Vac. Sci. Technol. A* **14** pp.529–34
- [22] Vishnyakov V I, Kiro S A and Ennan A A 2011 Heterogeneous ion-induced nucleation in thermal dusty plasmas. *J. Phys. D: Appl. Phys.* **44** 215201
- [23] Kodama N, Kita K, Tanaka Y, Uesugi Y, Ishijima T, Watanabe S, and Nakamura K 2014 Two-dimensional spectroscopic observation of a pulse-modulated induction thermal plasma torch for nanopowder synthesis. *J. Phys.: Conf. Ser.* **550** 012026
- [24] Kodama N, Tanaka Y, Ishisaka Y, Uesugi Y, Ishijima T, Sueyasu S, and Nakamura K 2017 Spatiotemporal distribution of thermal plasma temperature and precursor formation in a torch during TiO₂ nanopowder synthesis. *Plasma Sources Sci. Technol.* **26** 075008
- [25] Olesik J W and Hieftje G M 1985 Optical imaging spectrometers *Anal. Chem.* **57** pp.2049-55
- [26] Webb M R and Hieftje G M 2006 Improved monochromatic imaging spectrometer *Appl. Spectro.* **60** pp.57-60
- [27] NIST atomic spectra database, <http://www.nist.gov/pml/data/asd.cfm>
- [28] Chapman S and Cowling T 1952 *The mathematical theory of non-uniform gases*. (New York: Cambridge University Press)

Chapter 7

Conclusions

7.1 Introduction

In this thesis, a unique synthesis method using inductively coupled thermal plasma (ICTP) was investigated for large-scale production of Al³⁺-doped TiO₂ nanopowder. The ICTP method is useful to synthesis high purity nanopowder in very short time cycle, while this method has also disadvantages for controllability of synthesized nanoparticle and production efficiency. We developed a unique synthesis method using pulse-modulated induction thermal plasma in order to overcome these disadvantages.

In ICTP method, nanopowder is synthesized via feedstock evaporation, precursor formation, nucleation and nanoparticle growth processes. The clarification and understanding of these processes are necessary to increase nanopowder synthesis rate more. The PMITP should be controlled based on investigation results to facilitate these processes. From above reasons, nanoparticle synthesis process was visualized to discuss about nanoparticle synthesis process mainly feedstock evaporation and nucleation of nanoparticle in the ICTP torch. The two-dimensional optical emission spectroscopy (2D OES) measurement was used to investigate these topics. From 2D OES measurement results, feedstock evaporation, precursor formation, nucleation possibility. In addition, the admixing of feedstock vapor changes plasma properties and stability markedly especially in case of using metal feedstock. Therefore, spatial distribution of feedstock vapor admixture ratio was also determined.

In this chapter, the results derived in this thesis are briefly summarized as following sections.

7.2 Summary of results

7.2.1 Large-scale synthesis of Al³⁺-doped TiO₂ nanopowder

In this chapter, a unique large-scale synthesis method for Al³⁺-doped TiO₂ nanopowder was developed using pulse-modulated induction thermal plasma with time-controlled feedstock feeding method, i. e. PMITP+TCFF method. In this method, the feedstock injection was synchronized with coil-current modulation of PMITP system, that is, Al and Ti feedstock mixture was injected into the PMITP torch only during on-time of coil-current modulation. The PMITP and synchronized feedstock injection enables heavy-load feeding of feedstock powder to the thermal plasmas for complete evaporation. Synthesized nanopowder was analyzed using different methods including FE-SEM, XRD, BF-TEM with TEM/EDX mapping. XPS and spectrophotometry. Results showed that Al³⁺ element was doped in TiO₂ structure. In addition, particle diameter of synthesized nanopowder was varied depend on shimmer current level of modulated coil current. The production rate of Al³⁺-doped TiO₂ nanopowder was estimated to be about 400 g h⁻¹. This production rate is 10 to 20 times higher production rate compared with conventional non-modulated ICTP method.

7.2.2 Fundamental investigation of Ti feedstock evaporation in the ICTP torch during TiO₂ nanopowder synthesis

In this chapter, 2D OES measurements were conducted for an ICTP torch during TiO₂ nanopowder synthesis. The single powder injection was performed into the ICTP torch to fundamentally investigate the Ti feedstock evaporation process and to elucidate the formation process of precursor TiO molecule. Spatiotemporal distribution of Ti atomic line and TiO molecular spectra were simultaneously observed inside the plasma torch using developed 2D OES system. The observation results showed that the injected Ti feedstock was evaporated to form high density Ti atomic vapor in the ICTP torch. The generated Ti atomic vapor is transported and diffused by gas flow and density gradient. In addition, TiO molecular vapor was generated almost simultaneously around only on-axis region in the ICTP torch. In this experiment, low temperature Ar carrier gas was injected with Ti

feedstock into the torch. Consequently, on-axis temperature may cooled down by carrier gas injection and energy consumption due to feedstock evaporation. TiO molecules were formed inside this cooled down region.

7.2.3 Effect of coil-current modulation on feedstock evaporation and precursor TiO formation during TiO₂ nanopowder synthesis

In this chapter, effect of coil-current modulation on Ti feedstock evaporation and precursor TiO formation were fundamentally investigated from 2D OES measurement results during TiO₂ nanopowder synthesis using conventional ICTP or PMITP torch with continuous or intermittent feedstock injection. In addition, an interpretation was suggested from the 2D OES results for Ti feedstock evaporation and TiO formation in nanoparticle synthesis using a PMITP with intermittent feedstock feeding. Results showed that coil-current modulation and intermittent feedstock injection may enable efficient feedstock injection and precursor TiO formation in the PMITP torch.

7.2.4 Spatial estimation of Ti excitation temperature in the ICTP torch during TiO₂ nanopowder synthesis

In this chapter, spatiotemporal distribution of Ti excitation temperature ($T_{\text{ex}}^{\text{Ti}}$) was determined from 2D OES during TiO₂ nanopowder synthesis using conventional ICTP torch with single-feedstock injection. The temperature is one of the fundamental information to discuss feedstock evaporation and nucleation of nanoparticle. The spectroscopic observation results revealed that $T_{\text{ex}}^{\text{Ti}}$ was estimated as 2500–4000 K around the central axis of the ICTP torch, and as more than 4500 K in the off-axis region. In the on-axis region, TiO was detected with high radiation intensity in the lower temperature region. These results showed that TiO molecules are formed only in low temperature region around the central axis of the ICTP torch. In addition, TiO molecular density could be high especially in downstream region at central axis of the ICTP torch. Based on estimated temperature, nucleation possibility was also investigated from determination result of saturation vapor

pressure of TiO_2 vapor. As a result, TiO_2 nuclei can be formed inside the ICTP torch during nanopowder synthesis using ICTP with single feedstock injection.

7.2.5 Determination of Ti vapor admixture ratio in the Ar ICTP torch during Ti feedstock injection

In this chapter, the spatial distribution of the Ti vapor admixture ratio (X_{Ti}) was determined together with $T_{\text{ex}}^{\text{Ti}}$ from 2D OES during Ti feedstock injection into the Ar ICTP torch for Ti nanopowder synthesis. The X_{Ti} is one important parameter affecting ICTP properties such as its electrical conductivity. The value of X_{Ti} was estimated from the radiation intensity ratio of the Ar atomic line to the Ti atomic line, and $T_{\text{ex}}^{\text{Ti}}$ obtained from 2D OES observation. Furthermore the electron density (n_e) was also determined from the estimated results of $T_{\text{ex}}^{\text{Ti}}$ and X_{Ti} through the equilibrium composition. These 2D OES results revealed $T_{\text{ex}}^{\text{Ti}}$ as 2500–4000 K at around the central axis of the ICTP torch, although it was higher than 4000 K in the off-axis region. In the off-axis region, X_{Ti} and n_e were much higher than in the on-axis region. In addition, neutral Ti atomic density (n_{Ti}) was also determined from estimation results of $T_{\text{ex}}^{\text{Ti}}$ and X_{Ti} through the equilibrium composition. This estimated n_{Ti} is useful for quantitative discussion of Ti nucleation in the ICTP torch.

7.3 Scope of future researches

Nanomaterials receiving great attention in various fields because of their unique characteristics. In this thesis, only Al^{3+} -doped TiO_2 nanoparticle and pure- TiO_2 nanoparticle were treated and synthesized. These nanoparticle has very simple spherical structure and simple crystalline composition. Besides these simple structures, many kinds of nanomaterials have been investigated and studied for various applications. Thus, following topic should be included as future work:

(1) Synthesis of composite-nanomaterials.

Synthesis of “Composite-nanomaterial” is one of the key point to progress nanotechnology. Here “Composite” means synthesized nanomaterial consist of different two or more chemical and crystalline structure. By the compositing, it is possible to compensate for disadvan-

tages of material. For example, silicon (Si) nanoparticle is expected as next-generation anode material for high capacity lithium ion battery. Silicon nanoparticle has high discharge capacity compared with that of graphite used for the current electrode material. However, silicon has less electrical conductivity because of semiconductor. To improve this issue, for example, graphite-coated Si nanoparticle or carbon nanoparticle-supported silicon nanoparticle are investigated. These composite nanomaterial suggest high capacity with high electrical conductivity. Therefore, compositing is one of the way to use nanomaterial more efficiently.

For synthesize composite-nanomaterials, precursor formation and nucleation processes have to be controlled in detail more. To control nanopowder synthesis process, following points have to be investigated.

(2) Tomographic imaging of ICTP during nanopowder synthesis.

As shown in figure 3.5 in chapter 3, the structure of ICTP is not completely axisymmetric. Thus, as already described chapter 5, Abel inversion cannot be adopted to estimate local quantity of radiation intensity from observation result because Abel inversion for non-axisymmetric distribution may causes error. This problem decrease accuracy of measured and estimated results. Therefore, analytical methods that do not assume axisymmetric structure should be considered. In analytical method developed up to date, tomographic imaging of plasma is one of very powerful method to obtain actual (local) radiation intensity distribution. The tomographic imaging itself is a method often used for measurement of plasma. However, few researches have been reported for combination of tomographic imaging and 2D OES to obtain three-dimensional structure of specified wavelength. Thus, the combination of tomographic imaging with 2D OES have to be carried out to the ICTP or PMITP torch during nanomaterial synthesis.

(3) Discussion of thermal- and chemical- non-equilibrium during processing.

In this thesis, local thermodynamic equilibrium (LTE) involving chemical equilibrium was assumed to investigate inside the thermal plasma. The LTE assumption is frequently used for atmospheric pressure thermal plasma because high collision frequency lead plasma to equilibrium state under atmospheric pressure. However, in recent years it has been discussed that the high temperature plasma does not reach the complete-equilibrium state during material processing. From the numerical simulation, it has also been reported that

the deviation from the equilibrium state greatly affects the plasma properties, particle composition and temperature field of high temperature plasma. Therefore, it is better to perform new measurement and determination taking into account non-equilibrium of high temperature plasma.

(4) Clarification of nanoparticle growth process including agglomeration.

In this thesis, feedstock evaporation, precursor formation processes and nucleation possibility were mainly discussed during TiO₂ nanopowder synthesis. The discussion and investigation of these three processes are of course important for efficient and stable processing, but the subsequent growth and agglomeration processes have to also be understood because accurate control of particle size and prevention of agglomeration are the issues to be improved. It is need to measure particle size in the reaction field in order to investigate nanopowder growth. The laser light scattering, differential mobility analyzer, and cascade impactor are considered as powerful and effective measurement method of particle size distribution. However for each measurement method, measurable size range is restricted due to physical or technical limitation. This problem have to be noted to use these method.